Bioelectric Sensing and Navigation: Multimodal Control in Electric Fish and Endovascular Device Guidance

by

Erin Elizabeth Sutton

A dissertation submitted to The Johns Hopkins University in conformity with the requirements for the degree of Doctor of Philosophy.

Baltimore, Maryland

December, 2017

Abstract

Biological and engineered systems rely on constant input from multiple sensors. An understanding of the underlying mechanisms for sensory integration and control can inform developments in both fields.

Animal nervous systems resolve sensory conflict for the control of movement. For example, the glass knifefish, *Eigenmannia virescens*, relies on visual and electrosensory feedback as it swims to maintain position within a moving refuge. To study how signals from these two parallel sensory streams are used in refuge tracking, we constructed a novel augmented reality apparatus that enables the independent manipulation of visual and electrosensory cues to freely swimming fish. We evaluated the linearity of multisensory integration, the change to the relative perceptual weights given to vision and electrosense in relation to sensory salience, and the effect of the magnitude of sensory conflict on sensorimotor gain. First, we found that tracking behavior obeys superposition of the sensory inputs, suggesting linear sensorimotor integration. In addition, fish rely more on vision when electrosensory salience is reduced, suggesting that fish dynamically alter sensorimotor gains in a manner con-

sistent with Bayesian integration. However, the magnitude of sensory conflict did not significantly affect sensorimotor gain. These studies lay the theoretical and experimental groundwork for future work investigating multisensory control of locomotion.

Minimally invasive treatment of vascular disease demands dynamic navigation through complex blood vessel pathways and accurate placement of an interventional device. These challenging tasks have led to increased reliance on fluoroscopic guidance and commensurate radiation exposure to the patient and staff. Here we introduce a guidance system inspired by electric fish that incorporates measurements from a newly designed electrogenic sensory catheter with preoperative imaging to provide continuous feedback to guide vascular procedures without the need for ionizing radiation, image registration, or external tracking. Electrodes near the catheter tip simultaneously create a weak electric field and measure the impedance, which changes with the internal geometry of the vessel as the catheter advances through the vasculature. The impedance time series is then mapped to a preoperative vessel model to determine the relative position of the catheter within the vessel tree. We present navigation in a synthetic vessel tree and *ex vivo* biological tissue based on our mapping technique. Experiments in a porcine model demonstrated the sensor's ability to detect cross-sectional area variation *in vivo*. These initial results demonstrate the capability and potential of this novel bioimpedance-based guidance technology as a non-fluoroscopic technique to navigate intravascular devices.

ABSTRACT

Readers: Noah J. Cowan, Nassir Navab and Iulian Iordachita

Acknowledgments

First, I would like to acknowledge my advisor, Dr. Noah Cowan. His enthusiasm for biology is infectious. He demands hard work and rigorous science but freely expresses that he's very proud of his students' accomplishments. I especially thank him for his support of my academic tenure, career, and family.

Next, I thank my co-advisor, Dr. Nassir Navab. He trusted me with responsibility and freedom and always encouraged me to take advantage of professional opportunities like working temporarily in Germany. His work showed me that ambitious goals can really drive a project forward.

I would also like to thank my third thesis reader, Dr. Iuilian Iordachita. Since I first arrived at Johns Hopkins, I have admired Dr. Iordachita's research and technical skill, and I am very grateful for his input regarding this text.

I have been privileged to work with outstanding collaborators while at JHU. First, I am grateful to Dr. Eric Fortune of the New Jersey Institute of Technology for his help with the study design and interpretation of results for the multisensory integration research. Similarly, Dr. Sarah Stamper taught me everything I know

about electric fish and was an excellent friend and mentor throughout my graduate work. For the bioelectric sensing and navigation project, I worked very closely with Dr. Bernhard Fuerst. Besides his critical input to the research, I thank him for his vision and for making CAMP a strong social community. Finally, I appreciate the assistance of Dr. Reza Ghotbi of HELIOS Hospital, Munich West and HELIOS Amper Hospital, Dachau. He provided crucial clinical direction for the bioelectric sensing and navigation project. I am especially grateful for his granting me access to observe a range of endovascular procedures and answering all of my questions.

Finally, I could not have completed this work without my my colleagues in the LCSR, who helped me with everything from linear systems homework to obtaining a CTA of a live pig. I especially thank Ravi, Manu, Robert, Nicole, Mert, Shahin, Alison, Berk, Javad, Sing Chun, Mathias, Leila, Oliver, and Salvo for being wonderful friends to me.

I am deeply grateful to my Mom and Dad for instilling me with the confidence to take on this challenge and lovingly supporting me along the way. I thank my sister and best friend Claire. Finally, I thank Alican, a brilliant engineer who I am proud to call my husband.

Dedication

This thesis is dedicated to Alican and Evren.

Contents

List of Tables

List of Figures

List of Acronyms

PTFE polytetrafluoroethylene

DAQ data acquisition

DFT discrete Fourier transform

ANOVA analysis of variance

MRI magnetic resonance imaging

BSN Bioelectric Sensing and Navigation

IVUS intravascular ultrasound

OCT optical coherence tomography

CT computed tomography

CBCT cone-beam computed tomography

CSA cross-sectional area

OE-DTW Open-End Dynamic Time Warping

CAD computer-aided design

VMTK Vascular Modeling Toolkit

TKX Telazol, ketamine, xylazine solution

CTA computed tomography with angiography

PICC peripherally inserted central catheter

GUI graphical user interface

DRR digitally reconstructed radiograph

AAA abdominal aortic aneurysm

EVAR endovascular aorta repair

Chapter 1

Introduction

The processing of multimodal data streams is crucial to the success of both biological and engineered systems. In both cases, complementary sensors impart robustness and enable the perception of a coherent representation of the world given sometimes unreliable inputs to the processor. Therefore, close collaboration between biology and engineering leads to valuable insights and new tools for both disciplines.

Nature provides myriad examples of animals that combine data from independent sensory organs to inform their behavior. However, it has historically been difficult to tease apart the relative contributions of the sensors. Recently, there has been a push in the computational biology community to apply engineering principles to the study of biological systems [1, 2]. In particular, we use novel tools to quantify and analyze sensorimotor control during animal locomotion. My work focused on the elucidation of rules governing multisensory interaction during locomotion. The data streams in

this case arise from the visual and electrosensory systems of the weakly electric fish, whose nervous system integrates them to form a perception of the fish's environment.

Next, we apply an established method of sensory fusion in engineering to solve a clinical need. Our novel technology is founded on the integration of sensed measurements with a known anatomical model derived from medical imaging. Specifically, a pattern matching algorithm fuses electrical measurements of local blood vessel geometry to a global volumetric model. The algorithm yields an estimate of the location of a novel medical device in the human body. In this fashion, multisensory integration enables us to bridge the gap between sensing and navigation in the human body.

1.1 Thesis Organization

This dissertation is presented in two parts. Part I focuses on the application of control theoretic approaches to the study of multisensory integration during locomotion. The goal of this part was to shed light on two questions: (1) How is sensory information integrated during locomotion? (2) How are conflicts resolved during locomotion? Our model system was *Eigenmannia virescens*, a weakly electric fish native to South America. It is a convenient model system for multisensory research because, in addition to vision, it has an active electrosensory system that provides a complementary measurement of its surroundings [3]. Furthermore, it swims equally well forward and backward, facilitating the design of simple, one-dimensional locomotor

tasks. Finally, the fish exhibits a robust tracking behavior; without training, the fish swims to maintain position in a shelter. In this research, we investigated how *Eigenmannia virescens* integrate signals from two parallel sensory streams, vision and electrosense, while swimming inside a moving refuge. Our novel augmented reality experiment independently manipulates visual and electrosensory motion cues, revealing how the neural controller weights different senses. The experiments are performed in the dark, so the moving refuge is invisible to the fish's vision, and electrosense dominates the fish's response to the refuge motion. Gray stripes are projected onto the refuge and moved longitudinally in a prescribed trajectory independent of the physical refuge trajectory and serve as the visual cue of refuge position. In this study, we measured the fish response to a unimodal visual stimulus (stationary physical refuge), unimodal electrosensory stimulus (stationary stripes), and bimodal coherent stimuli in which the physical refuge and stripes followed the same trajectory. By analyzing the gain between the input trajectories and the fish's response, we discovered that the fish rely more heavily on vision when the electrosensory signal is degraded, and the fish linearly sum visual and electrosensory signals.

Part II of this dissertation introduces a novel system for arterial catheter navigation inspired by the electrosense of the weakly electric fish. Although minimally invasive treatment of vascular disease is becoming increasingly common, it remains extremely challenging to dynamically navigate complex 3D vessel pathways and accurately place an interventional device. After two decades of improvements to peri-

operative imaging, the limited visualization of complicated anatomical structures and surgical devices results in a substantial number of revisions after minimally invasive interventions [4, 5]. Surgical revisions lead to a deterioration of the disease prognosis and an increase in therapy costs. Faced with these pressures, surgeons have relied on near-continuous fluoroscopic imaging for visual feedback during common procedures, dramatically increasing the radiation dose [6]. With input from our clinical partners, we determined that the outcome of the vascular intervention can significantly benefit from a guidance system that fuses a local measurements from a sensor-equipped catheter to a global model of the vascular tree. Such a system would maintain accuracy during vessel deformation, a current obstacle to image-based guidance technologies. Our new catheter navigation system, modeled after the electrosense of the electric fish, features an active electrosensory catheter that measures a blood vessel from the inside-out. Our software identifies the vessel based on the catheter's local electric field measurements in a global map of possible paths the catheter could take through the vasculature, extracted from pre-interventional imaging. In this thesis, I describe the motivation, development, and experimental validation of the system, Bioelectric Sensing and Navigation. Once integrated into the clinical workflow, it could dramatically reduce patient, interventionalist and staff radiation exposure and make common endovascular procedures easier and quicker to perform.

Part I

Multimodal Control During Refuge Tracking in *Eigenmannia virescens*

Chapter 2

Multisensory Interaction During Locomotion

2.1 Introduction

How multimodal information is integrated for the moment-to-moment control of movement is not well understood, in part because different tasks, environments, and physiologies necessitate different strategies. In lobsters, motor control shifts between modalities in a context-dependent manner; tethered lobsters used vision to track the movement of a low-frequency stimulus and proprioception to track a high-frequency stimulus [7]. This strategy has also been observed in freely swimming sharks. Sharks switch between sensory modalities during hunting and substitute alternate modalities when necessitated by environmental changes or their own sensory limitations [8].

Rather than a switch or substitution, flies apparently integrate information contemporaneously across many sensory modalities for behavioral control. For example, a tethered fly does not locate the source of an attractive odor without a richly textured visual panorama [9]. Further, the odor has a context-dependent influence over the gain of the optomotor response [10]. The fly's motor responses to simultaneous visual and olfactory cues are a linear sum of the responses to these stimuli when presented alone [11].

Weakly electric fishes appear to re-weight multimodal information in relation to behavioral context. During prey capture, the relative contributions of vision, electrosense and mechanosense change as a function of environmental factors such as water conductivity [12, 13]. Similarly, these fish dramatically change their locomotor behavior based on ambient illumination. While they track a refuge smoothly in the light, the fish produce fore-aft movements in the dark that are believed to enhance electrosensory feedback [14].

Each of these studies used a similar approach in which the animal's performance was compared between conditions in which either the sensory modalities themselves were systematically restricted or the availability of sensory stimuli was altered (i.e. the animal did not have simultaneous access to more than one sensory modality). The application of control theory, however, requires the dynamic perturbation of sensory feedback. Here, we developed an augmented reality infrastructure that enables simultaneous and independent manipulation of the two sensory modalities, vision and

electrosense, relied on by weakly electric fishes to perform refuge tracking [15–18]. In this robust and natural behavior, untethered fish swim to maintain position within a moving refuge. Our novel system enables us to apply small perturbations to sensory feedback in each modality, which permits control theoretic analyses of multimodal integration during free behavior.

We evaluated the linearity of the multisensory interaction by simultaneously presenting either conflicting or coherent visual and electrosensory cues. We also quantified the effects of saliency of electrosensory cues on the relative weights given to electrosense and vision. Finally, we examined whether fish re-weight sensory information based on the magnitude of conflict between visual and electrosensory cues.

2.2 Dissemination and Organization

Portions of this work were published in a journal article [19] and presented at a national [20] and a regional conference [21]. The datasets and analysis code supporting Chapter 3 are available at dx.doi.org/10.7281/T1D798BQ. The following chapter, Chapter 3, details our theory, experimental framework, and findings related to multisensory integration during refuge-tracking by weakly electric fish.

2.3 Contribution

The work detailed in this part of the thesis was primarily executed by me. In particular, I was independently responsible for the collection and analysis of data and presentation of our findings. Alican Demir was was instrumental in the design and construction of the experimental apparatus. Sarah Stamper and Eric Fortune contributed to the conception of the experiment and interpretation of the results. Noah Cowan led the experimental design and interpretation of results.

Chapter 3

Dynamic modulation of visual and electrosensory gains for locomotor control

3.1 Closed-Loop Model of Multisenory Control

The neural computations involved in sensorimotor control are fundamentally closed-loop: sensing governs action, action changes the state of the animal in its environment, and these changes are sensed. Control theory provides a common framework to quantify and interpret the behavior of the whole animal through perturbations to

exogenous reference signals and measurements of corresponding behavioral responses (for reviews, see [1, 2]). Closed-loop neuromechanical modeling has been used to investigate the feedback control of diverse biological systems and behaviors, including flight control in moths [22,23] and flies [24–26], flower tracking in moths [27], postural balance in humans [28, 29], and refuge-tracking fish [14, 30, 31].

Building on this tradition of using control theory in the study of biological systems, we apply system identification techniques to analyze how the fish performs the complex sensorimotor task of refuge tracking. Refuge tracking is a closed-loop behavior; the fish continuously modulates its motor commands to stabilize itself with respect to the moving refuge. The behavior is enabled by the nervous system's ability to filter parallel visual and electrosensory streams in a modality-specific way and then fuse them into a unified precept of the refuge. Because our apparatus (Fig. 3.1a) enables us to provide independent cues to each sensory modaility, we can apply feedback control theory to elucidate the rules governing that multisensory interaction. The topology of our experiment is represented by the block diagram in Figure 3.1c, where all signals and subsystems are modeled in the frequency domain. In a recent study, Roth et al used a similar topology and analysis to show the linearity of vision and mechanosense in moths performing flower-tracking [27].

When the visual and electrosensory stimuli are congruent, $V(s)$, $E(s)$, and $C(s)$ can be collected into a single sensorimotor transform. Under this assumption, Cowan and Fortune showed that this lumped multisensory controller depends on a precise

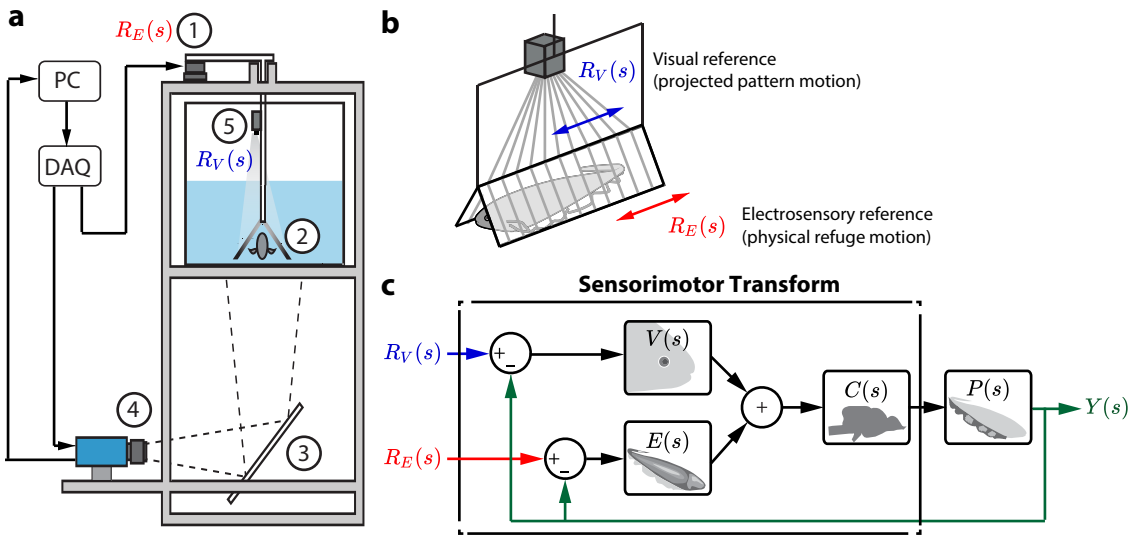

Figure 3.1: **Experimental setup and model**. **a)** The stepper motor (1) translates the refuge (2) according to a trajectory defined by the PC. A mirror (3) enables the camera (4) to collect video of the fish in the refuge from below. A projector (5) back-projects dim stripes on to the translucent refuge. **b)** The projected stripes and physical refuge present the fish with independent sensory cues to the movement of the refuge. **c)** Adapted from [2]. Blocks represent subsystems (transfer functions), and arrows depict signals. All signals are presented in the frequency domain where s is the complex Laplace variable representing frequency. The visual input, $R_V(s)$, is compared to the fish position, $Y(s)$, to create an error signal representing the relative position of the fish to the visual input. The error is transformed by the open-loop gain to vision, $V(s)$. The independent electrosensory input, $R_E(s)$, is compared to the fish position to create an error signal representing the relative position of the fish to the electrosensory input. The error is transformed by the open-loop gain to electrosense, $E(s)$. The resulting visual and electrosensory signals are combined and processed into muscle commands by the central nervous system, $C(s)$, with the putative goal of reducing both error signals. The fish swims by producing motor commands that are filtered by $P(s)$, the biomechanical plant; the resulting self-motion of the fish is fed back into the system. In this manner, the fish continuously stabilizes itself with respect to the time-dependent reference signals.

model of the plant [32]. Subsequently, Sefati et al. published a model of the plant, $P(s)$, based on a quasi-steady analysis of the fluid dynamics [33]. Critically, we do not yet understand how visual and electrosensory cues are integrated by the brain

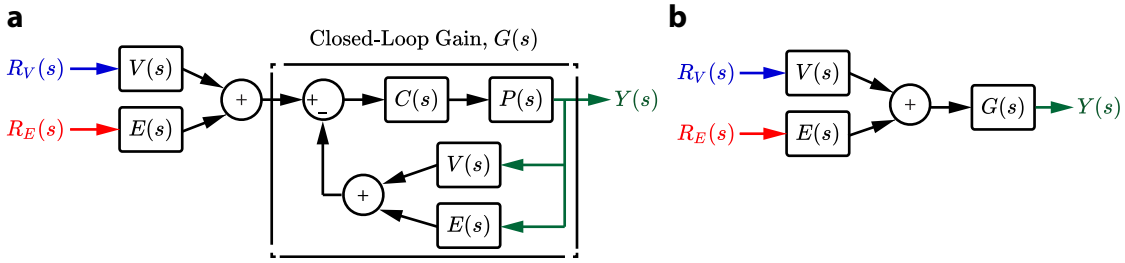

Figure 3.2: **Topological simplification of the experiment**. **a)** A reorganized diagram, mathematically equivalent to Figure 3.1c. **b)** The simplified model, where $G(s)$ is the closed-loop gain.

to control refuge tracking. Here, we are interested in the relative open-loop sensory gains to vision, $V(s)$, and electrosense, $E(s)$. These transfer functions represent the frequency-dependent perceptual "weight" given by the central nervous system to vision and electrosense, respectively, as a function of stimulus frequency.

To characterize $V(s)$ and $E(s)$, we measure the fish motion as it resolves the conflict between independent electrosensory and visual inputs, rather than the congruent stimuli used in previous studies. By examining the frequency content of the fish's tracking motion in response to independent perturbations to vision and electrosense, we quantify the performance of individual components of the closed-loop system in terms of a behavior-level model. Once the system is broken into its constituent subsystems, the equation predicting its response, $Y(s)$, to given reference signals can be derived from the block diagram. To make the transfer function algebra more intuitive, we rearrange the block diagram (Fig. 3.1c) such that the feedback loop is consolidated into a closed loop transfer function, $G(s)$ (Fig. 3.2a). Then, as shown in Figure 3.2b, we simplify the closed-loop block diagram to an open-loop cascade

of visual and electrosensory motion processing, $V(s)$ and $E(s)$, with the closed-loop transfer function, $G(s)$:

$$Y(s) = G(s)V(s)R_V(s) + G(s)E(s)R_E(s) \tag{3.1}$$

In Eqn. (3.1), $G(s)$ encapsulates the closed-loop dynamics, including the animal's reafferent stimulation of its own visual and electrosensory cues:

$$G(s) = \frac{C(s)P(s)}{1 + C(s)P(s)(V(s) + E(s))}$$

That is, the presence of $V(s)$ and $E(s)$ in the denominator of $G(s)$ reflects the fact that vision and electrosense still contribute to the feedback loop regardless of which modality is perturbed. Crucially, $G(s)$ multiplies both $E(s)R_E(s)$ and $V(s)R_V(s)$ in Eqn. (3.1) (Fig. 3.2). Therefore, the open-loop gains, $V(s)$ and $E(s)$, are proportional to closed-loop experimentally measured gains $G_V(s)$ and $G_E(s)$, respectively:

$$G_V(s) = G(s)V(s)$$

$$G_E(s) = G(s)E(s)$$

The closed-loop gain to vision, $G_V(s)$, is the proportion of the fish response due to the visual reference motion, while the closed-loop gain to electrosense, $G_E(s)$, is the proportion due to the electrosensory reference motion. In terms of $G_V(s)$ and $G_E(s)$, the fish response is:

$$Y(s) = G_V(s)R_V(s) + G_E(s)R_E(s)$$

In this manner, the input-output frequency response of the whole system enables

us to empirically observe the relative contributions of vision and electrosense in the sensorimotor transform.

3.2 Materials and Methods

3.2.1 Experimental Apparatus

Our multisensory stimulation method exploits the fish's natural tendency to seek refuge in narrow cavities. The experimental apparatus is similar to that reported in previous studies [14,30,32,34] and was equipped with an actuated refuge, a projector, and a high-speed video camera (Fig. 3.1a). The test environment is a 17-gallon rectangular tank made from non-tempered clear glass. We constructed a 12 cm x 5 cm x 4 cm triangular refuge of 0.05 cm white PTFE held in place by a clear and colorless acrylic frame. The frame was designed to give as little electrosensory information possible beyond that of the PTFE refuge. The frame connects the refuge to the linear stepper motor (STS_0620-R, H2W Technologies, Inc., Valencia, CA, USA) which actuates the refuge along the longitudinal centreline of the tank with up to 1 micron resolution. Uniquely, this apparatus includes a projector (Pocket Projector Pro, Brookstone, Merrimack, NH, USA) mounted on the stepper motor and aligned with the centre of the refuge. It back-projects the visual stimulus, a pattern of 15 vertical stripes, onto the refuge (Fig. 3.1b). The trajectory of the stripes is controlled independently from that of the refuge. Crucially, the PTFE

refuge is sufficiently translucent so that the projected light pattern can be seen by the fish from inside the refuge. As the fish maintains position under the refuge, it gathers electrosensory information from the physical refuge structure and visual information from the light pattern. The stripes are the dimmest that still elicit a tracking response when the refuge is stationary, because if too bright, the stripes partially illuminate the tank and the fish can see the refuge.

A high-speed camera (pco.1200 camera link, PCO AG, Kelheim, Germany) records the fish's position inside the refuge. A mirror placed at an angle below the tank provides direct viewing access to the fish for videography. Two infrared LED illuminators (CMVision-IR200, C&M Vision Technologies, Inc., Houston, TX, USA) are mounted under the tank to facilitate recordings in the dark. No markers are required.

3.2.2 Experimental Procedure

Five adult *Eigenmannia virescens* (length 12–15 cm) were obtained from a commercial vendor and housed according to published guidelines [35]. Fish were drawn from communal mixed-sex tanks at 27^{o}C and conductivity 150–250 μS·cm^{-1}. All experimental procedures were approved by the Johns Hopkins University Animal Care and Use Committee and followed guidelines established by the National Research Council and the Society for Neuroscience.

An individual fish was transferred to the testing environment at least 12 hours prior to a data collection session. Each fish received ten replicates of six stimuli

profiles (Table 3.1) at two conductivities, 150 μS·cm^{-1} and 500 μS·cm^{-1}, all in the dark. The profile order was randomized with the constraint that the fish complete every profile once before repeating any profile. Fish 3, Fish 4, and Fish 5 performed the trials at low conductivity first, and Fish 1 and Fish 2 performed high-conductivity trials first.

For a given profile, both the electrosensory and visual stimuli include a high-amplitude (2.4 cm·s^{-1}), low-frequency (0.05 Hz) base component which the fish has been shown to track accurately [14, 30, 32]. In addition, one or both of the sensory inputs contained a higher frequency (0.25 Hz) "probe" component at one of two amplitudes (0.36 or 0.18 cm·s^{-1}) with randomized phase. Both probe component amplitudes were deliberately chosen to be much lower than that of the base component, because we expected that the small amplitude probe signal would act as a cross-modal illusion and trigger an unconscious sensory re-weighting rather than an attentional switch [36]. For example, the input trajectory for the refuge in Profile 3 (high-amplitude electrosensory probe) was given as follows:

$$r_E(t) = 2.4 \cdot \cos(0.05 \cdot 2\pi t) + 0.36 \cdot \cos(0.25 \cdot 2\pi t)$$

Since there was no visual probe for that trial, the light pattern was given as follows:

$$r_V(t) = 2.4 \cdot \cos(0.05 \cdot 2\pi t)$$

Here, $r_E(t)$ and $r_V(t)$ indicate time domain representations of $R_E(s)$ and $R_V(s)$, respectively.

Table 3.1: Input Profile Probe Amplitudes ($cm \cdot s^{-1}$)

Profile	Electrosense	Vision
1	0	0.36
2	0	0.18
3	0.36	0
4	0.18	0
5	0.36	0.36
6	0.18	0.18

The fish completed ten "training" trials of the high-amplitude coherent stimuli (Profile 5) before a data collection session began. The fish performed approximately 36 trials in each session with an approximate inter-trial interval of two minutes in which the refuge and light pattern were stationary. To mitigate transient effects, each 100 second trial had 10 second ramps at the beginning and end which were excluded from further analysis. The base frequency of 0.05 Hz dictated that the period is 20 seconds, so each trial consisted of exactly four periods of the input. The camera frame rate was 20 Hz, meaning 1600 frames of data were collected for analysis for each trial. Video clips of a fish performing a profile at both conductivity conditions are included in supplemental material.

Because the fish were unconstrained, they occasionally performed movements unrelated to the tracking task. Experiments in which the fish left the refuge or reversed

orientation within the refuge were excluded from data analysis. All other volitional movement was included. Fish 1 only completed three successful trials of the high-amplitude electrosensory stimulus (Profile 3) at high conductivity, and those trials were also excluded.

3.2.3 Data Analysis

The absolute positions of the fish and refuge for each trial (N = 558) were digitized from the video in Matlab using custom code (MathWorks, Natick, MA, USA), and the time trajectory of velocity for the refuge, visual stimulus, and fish were calculated (Fig. 3.3A). The remainder of the analysis will be in terms of velocity, not position, because the fish were free to maintain an arbitrary position and initial orientation with respect to the refuge, as in previous studies of refuge tracking [14, 30].

The time-domain mean of a single fish's velocity for each profile for ten replicates was taken at each frame of that profile, a technique recommended to reduce the bias and variance of the frequency response function measurement [37]. For instance, the fish occasionally uses whole-body bending to extract additional electrosensory information from its surroundings [14] and rapid shifts in position to correct accumulated tracking error (drift with respect to the refuge), and time-domain averaging reduces the effects of these nonlinear behaviors (Fig. 3.4).

A discrete Fourier transform (DFT) was applied to the averaged velocity data using the fast Fourier transform algorithm. The DFT represents the time-domain

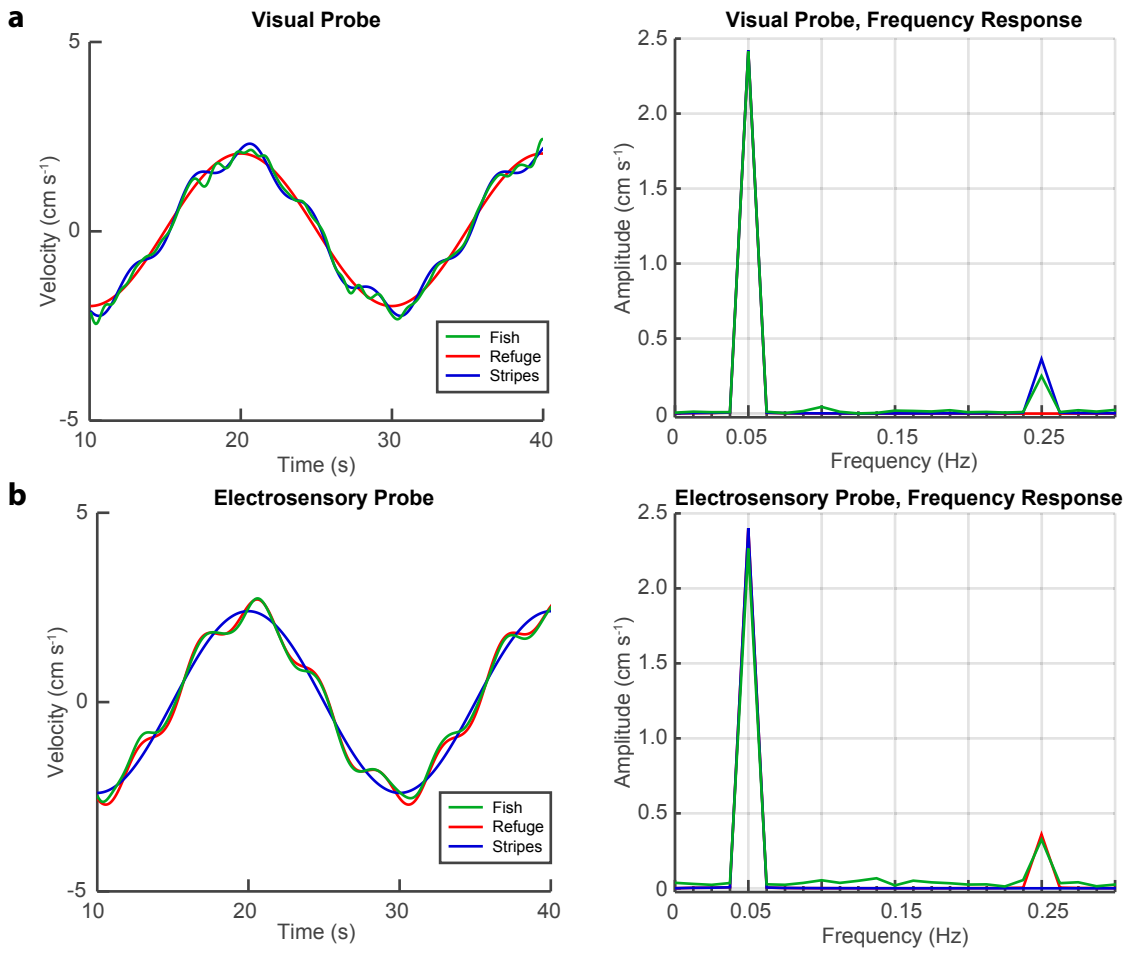

Figure 3.3: **Exemplary data**. For these stimulus profiles, the fish tracked the stimuli so closely that there is significant overlap in both the time (left panels) and frequency (right panels) domains. **a)** On the left, 30 seconds, excluding the ramp (1.5 input periods), of time domain velocity data for Profile 1, high-amplitude visual stimulus at low conductivity. The first ten seconds of each trial was a ramp, so the first input period began at $t = 10$ seconds. The fish (green) tracked the low frequency coherent base component and the high-frequency visual probe component (blue) of the stimulus. On the right, peaks in the fish's response are visible at the frequency of the base component (0.05 Hz) and visual probe component (0.25 Hz). **b)** Profile 3, high-amplitude electrosensory stimulus at low conductivity. The fish tracked both the low-frequency coherent base component and the high-frequency electrosensory probe component (red) of the stimulus.

signals as complex-valued functions of frequency (Fig. 3.4). From the frequency domain data, we extracted the gain at the base frequency in response to the coherent stimulus and the gain at the probe frequency due the modality of interest. Together, these terms compose the closed-loop gain, $G_V(s)$ or $G_E(s)$, and we calculated magnitude and angle from the resulting complex function.

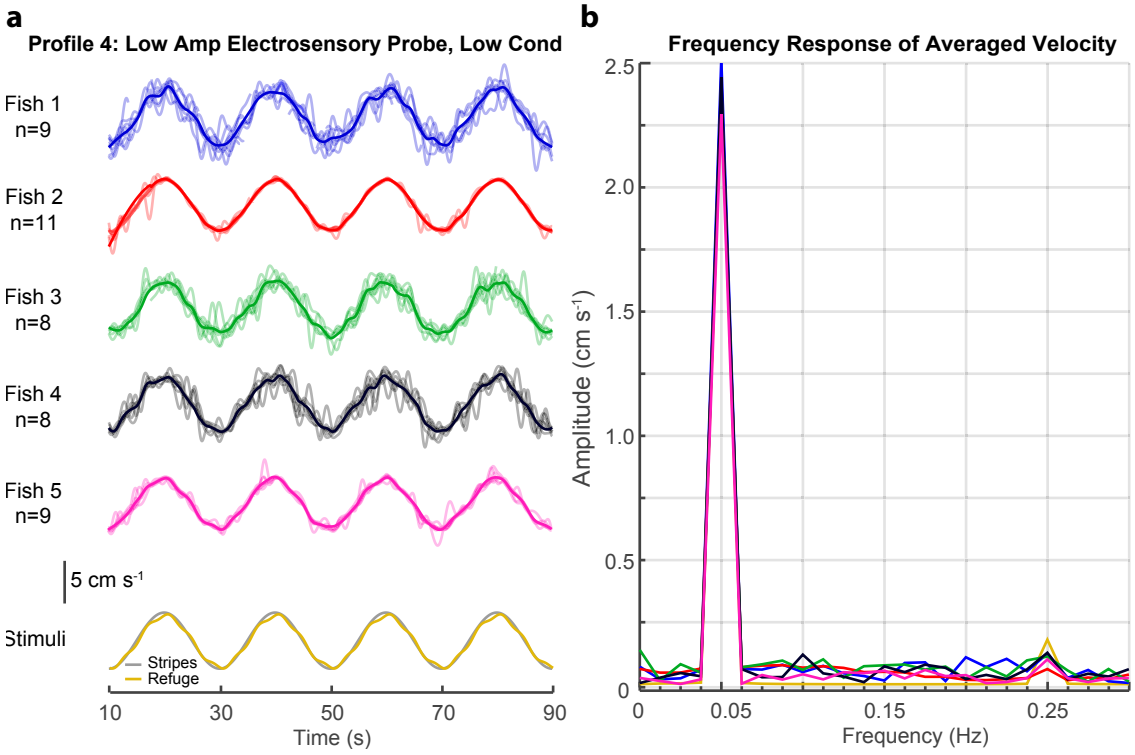

Figure 3.4: **Velocity trajectories yield frequency responses to Profile 4.** **a)** Velocity trajectories for individual trials (light) and mean trajectory (dark) for each fish performing Profile 4, low-amplitude electrosensory probe stimulus at low conductivity. Each fish performed n replicates of each profile at low conductivity. **b)** Discrete Fourier Transform around the base and probe frequencies for each fish's (color) time-domain averaged velocity. Noisier fish velocity trajectories (Fish 1 and 4) are visible as gains at frequencies other than the stimuli frequencies.

There was assumed to be no measurement error on the input or output, a reasonable assumption given the high precision of the measurement equipment and syn-

chronization built into the data collection system.

Unless otherwise noted, a full factorial two-way ANOVA tested the effect of conductivity and/or stimulus amplitude (depending on the hypothesis) on the fish response. All statistical analyses were performed using Matlab's anova1 and anovan functions (MathWorks, Natick, MA, USA).

3.3 Results

3.3.1 Fish Display Multisensory Enhancement

The highest peaks in output power occurred at the input frequencies at low and high conductivity. Experiments were conducted at low (150 μS/cm; Fig. 3.5) and high (500 μS/cm; Fig. 3.6) conductivity. For each conductivity, stimulus amplitudes were either low (0.18 cm/s) or high (0.36 cm/s). Salience and linearity were assessed using high-amplitude probe stimuli. Quantifying the affect of amplitude required including the low-amplitude probe stimuli.

As shown in Figure 3.6, at high conductivity fish generally exhibited responses to both low- and high-amplitude visual stimuli and these responses appear to be more robust in comparison to low conductivity (Fig. 3.5). There are some idosyncratic differences between fish. In particular, Fish 2 displayed the lowest noise to all input profiles, the highest gains to vision, and the lowest gains to electrosense at both conductivities. In addition, Fish 2 displayed higher gain to electrosense at

high conductivity than low conductivity. Note that it is experimentally infeasible to randomize conductivity on a trial-by-trial basis without endagering the health of the fish due to the time required to acclimate to differing conductivities, so all trials for a given conductivity were performed in one batch, and these batches were randomized across fish. Thus there may be an ordering effect and/or behavioral state change for Fish 2 between these conditions. Indeed, if one were to remove this fish as an outlier, our results regarding gain ratio become strongly significant as reported in the main text. Likewise, Fish 1 and 5 appear to exhibit noisier responses to the low-amplitude coherent stimulus (Profile 6) at high conductivity than than at low conductivity.

From this result, we conclude that the fish tracked the stimuli, and its response was not the result of other behaviors such as exploratory movements.

The magnitude of a response to a stimulus with coherent visual and electrosensory components was compared to that for the visual and the electrosensory stimuli alone. We expected multisensory enhancement: the sum of the gain to vision from a trial with a visual probe and gain to electrosense from a trial with an electrosensory probe would be less than the gain in a trial where the stimuli are coherent [36]. The fish displayed multisensory enhancement, exhibiting significantly higher gain for coherent cross-modal stimuli (Profiles 5 and 6) compared to single stimuli trials (Profiles 1-4) (Fig. 3.7). That result is consistent with the literature in fish [14, 15] and mammals [38, 39] and indicates that the fish uses visual-electrosensory integration during refuge tracking.

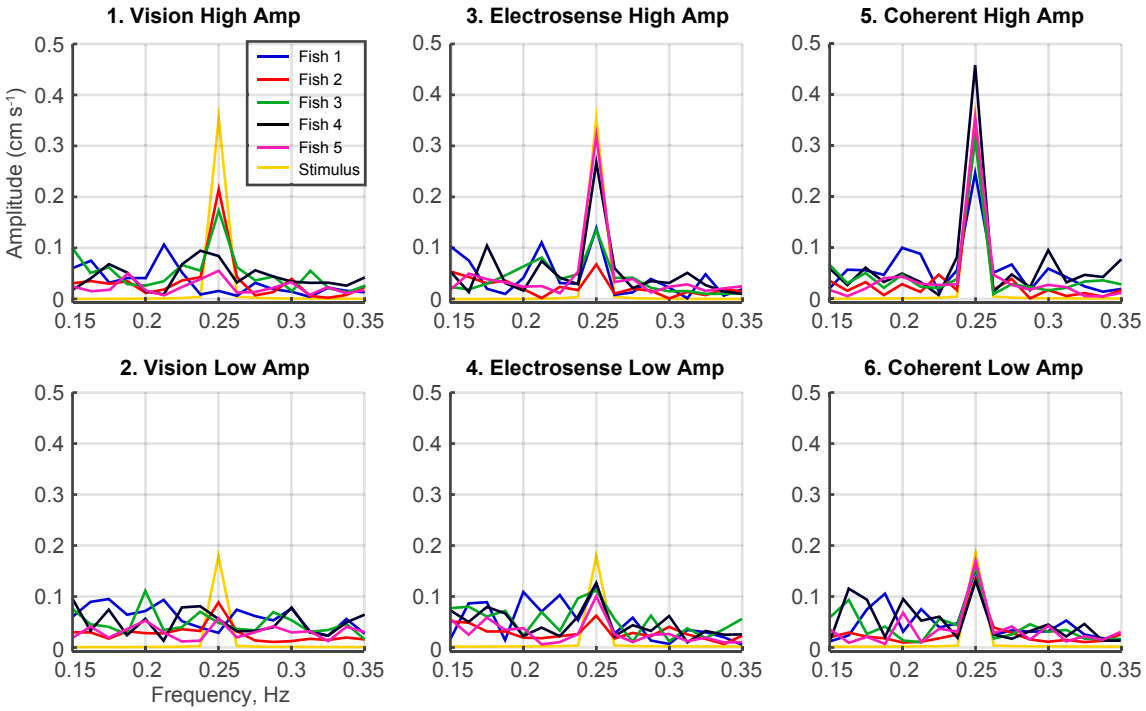

Figure 3.5: **DFT around probe frequency at low conductivity**. Each line represents the magnitude around the probe frequency of a single fish's time-averaged velocity. The low-frequency base component is omitted but the response closely matched the input for all fish at all conditions. The fish showed increased responses to unimodal electrosensory stimuli (Profile 3 and 4, middle column) compared to unimodal visual stimuli (Profile 1 and 2, left column) at both amplitudes. Only two fish strongly tracked the low-amplitude unimodal visual stimulus (Profile 2, lower left).

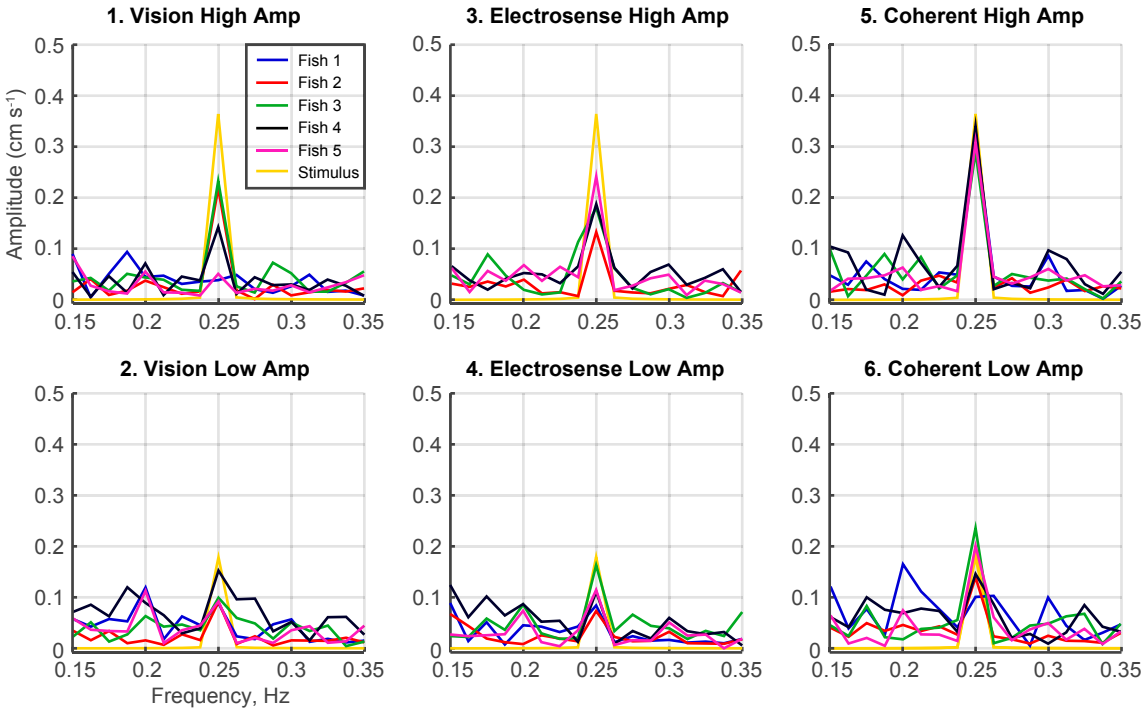

Figure 3.6: **DFT around probe frequency at high conductivity**. Again, each line represents the magnitude around the probe frequency of a single fish's time-averaged velocity. The fish generally showed increased responses to unimodal electrosensory stimuli (Profile 3 and 4, middle column) compared to unimodal visual stimuli (Profile 1 and 2, left column) at both amplitudes.

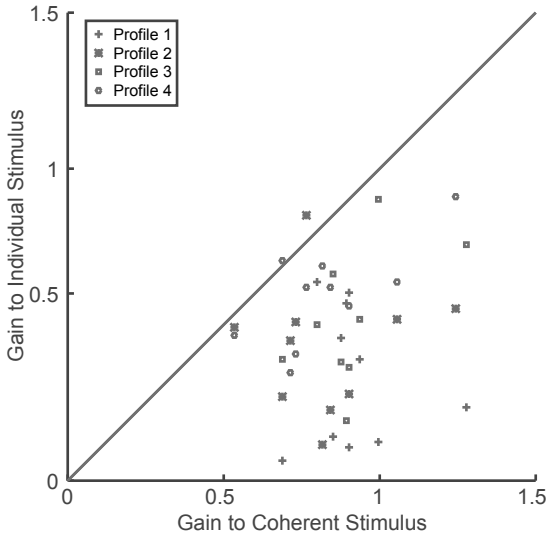

Figure 3.7: **Fish response reveals multisensory enhancement**. Each marker represents the average gain across fish for a single profile at a single conductivity compared to the gain to the coherent stimulus at the same amplitude and conductivity. Data falling close to the line represent conditions in which the the gain to a single stimulus was equal to the gain to a coherent stimulus. The fish showed significantly higher gain to cross-modal (coherent) stimulus than a probe stimulus to a single modality, regardless of modality, amplitude, or conductivity ($p = 2.013\text{x}10^{-13}$, one-way ANOVA).

3.3.2 Multisensory Interaction is Approximately Linear

From our first hypothesis, we expected that for trials with the high amplitude probe, the sum of the gains to vision from a trial with a visual probe and gain to electrosense a trial with an electrosensory probe would be approximately equal to the gain in a trial in which the stimulus contains coherent visual and electrosensory components at high amplitude. Specifically, $G_{Co} = G_V + G_E$, where here G_V is the closed loop gain to vision in trials with profile 1, G_E is the closed loop gain to electrosense in trials with profile 3, and G_{Co} is the closed loop gain to electrosense in trials with profile 5.

Since the frequency response is characterized by both a phase shift and magnitude, we consider its position on the complex plane, where gain magnitude is the distance from the origin and phase shift is the counterclockwise angle from the positive real axis [30]. The multisensory integration appears to be approximately linear (Fig. 3.8a). At low conductivity, when the stimulus contained coherent visual and electrosensory components, the gain magnitude was slightly higher than the sum of the incoherent stimuli, but the effect was insignificant (Fig. 3.8b). At high conductivity, the response was indistinguishable from linear.

In low conductivity, not all fish exhibit a robust response to the unimodal visual probe (see supplemental material). However, when the visual probe is coherent

with the electrosensory probe, there is a strong enhancement over the unimodal electrosensory response, demonstrating that the visual stimulus is salient. This indicates a supralinear integration of vision and electrosense at low conductivity. This supralinear relationship is borne out on the complex plane (Fig. 3.8a).

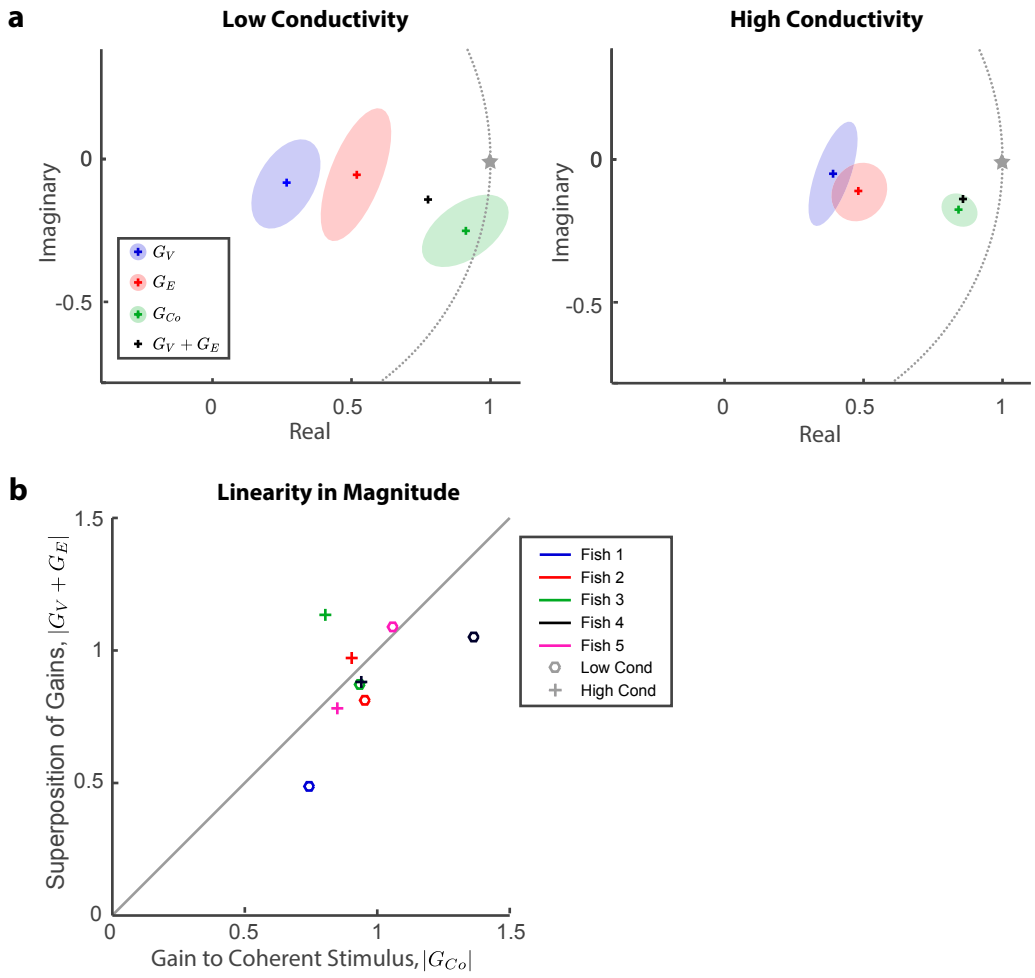

Figure 3.8: **Evidence for linear multimodal integration**. **a)** For a given frequency, the fish's response is characterized by a phasor, a point on the complex plane $\alpha e^{i\phi}$, where α is the magnitude of the gain and ϕ is the phase shift, with positive phase measured counterclockwise from the positive real axis. Each frequency response point represents the mean phasor across fish for a given profile. The ellipses show the standard error for each stimulus profile across fish. Tracking error is the distance from one frequency response point to the grey $\star$ at (1,0i), which represents unity gain and zero phase lag. The average sum of the response to the individual stimuli are shown (black) to the empirical response to the coherent stimuli is shown in green with an error ellipse. For a linear system, these responses would agree. At low conductivity, when the stimulus contained coherent visual and electrosensory components, the mean gain magnitude was slightly increased compared to incoherent stimuli. At high conductivity, the response appears to be linear in phase and magnitude. **b)** The magnitude of the fish response to high amplitude probe stimuli was indistinguishable from linear at both low ($p = 0.356$) and high conductivity ($p = 0.548$).

3.3.3 Electrosensory Saliency Modulates Visual Gain

When the conductivity of the water was increased, the fish experienced decreased contrast in the perceived electrosensory image of the refuge [12]. We found that the gains for trials with coherent stimuli (Profiles 5 and 6) were unchanged between conductivity conditions, suggesting that the fish accurately tracked the refuge despite the categorical change in electrosensory saliency (Fig. 3.8). While unintuitive, this result has been described once before [14]. What remains unknown, and what we investigated here, is the extent to which the fish re-weights electrosensory and visual information in adverse environmental conditions.

We anticipated that the fish would re-weight the electrosensory and visual signals to favor vision when electrosensory saliency was reduced. The gain ratio $G_V(s)/G_E(s)$ is useful to evaluate the fish's sensory re-weighting. A gain ratio equal to 1 would indicate that the fish weights visual and electrosensory stimuli equally, and $G_V(s)/G_E(s) > 1$ indicates a higher weight to vision than electrosense. At low conductivity, only Fish 2 weighted vision higher than electrosense, suggesting that given a salient electrosensory stimulus, fish relied more heavily on electrosense than vision (Fig. 3.9a). We observed significantly higher gain ratios for high-conductivity trials compared to low-conductivity trials for four out of five fish (Fig. 3.9a).

The fish up-weighted vision when the electrosensory signal was degraded (Fig. 3.9b). Specifically, in profiles with a visual probe (Profiles 1 and 2), gain to vision was significantly higher at high conductivity than low conductivity across fish and

amplitudes, implying that the re-weighting was mediated by modulating the gain to vision rather than a change in electrosensory gain.

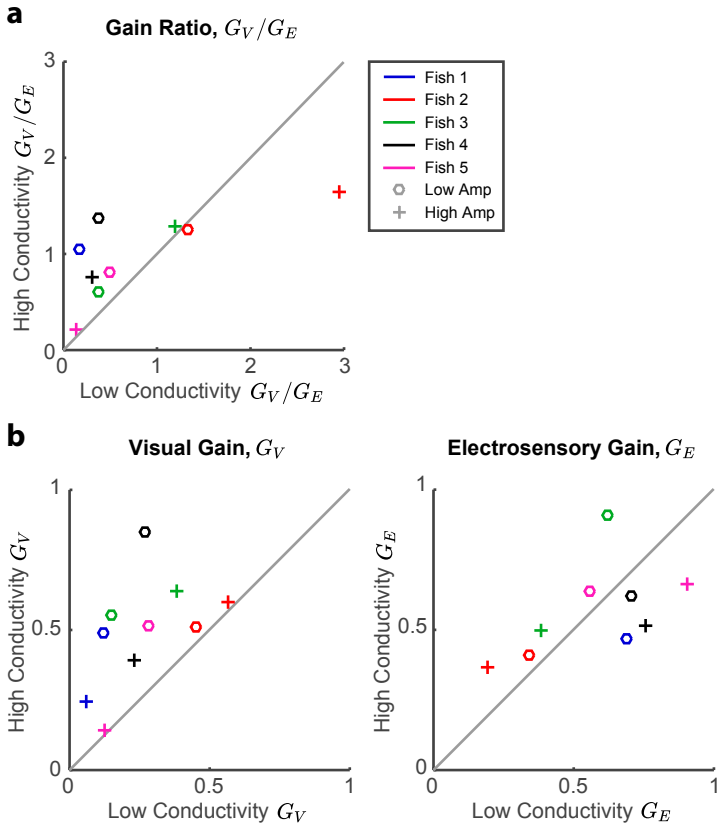

Figure 3.9: **Effect of conductivity on the magnitude of the response**. **a)** The magnitude of each fish's gain ratio for low- and high-amplitude stimuli. Fish 2 weighted vision three times higher than electrosense at high amplitude in low conductivity. With Fish 2, the gain ratio shift was insignificant ($p = 0.482$). Excluding Fish 2, the gain ratio was significantly higher ($p = 0.045$) at high conductivity than at low conductivity. **b)** Gain to vision was significantly higher ($p = 0.018$) at high conductivity than low conductivity across fish and amplitudes, while gain to electrosense remained statistically unchanged ($p = 0.948$).

The gain is a complex number containing both magnitude and phase information about the fish's response. The tracking error, or Bode error, captures both phase and magnitude at the probe frequency, so it is a useful measure to compare tracking

performance between profiles [30]. On the complex plane, the tracking error is the distance from the frequency response point to the point representing perfect tracking (unity gain and zero phase shift) (Fig. 3.8a). In terms of tracking error, the fish displayed more accurate tracking of the visual stimulus at high conductivity than the same stimulus at low conductivity (Fig. 3.10). Again, the electrosensory response was unchanged by conductivity.

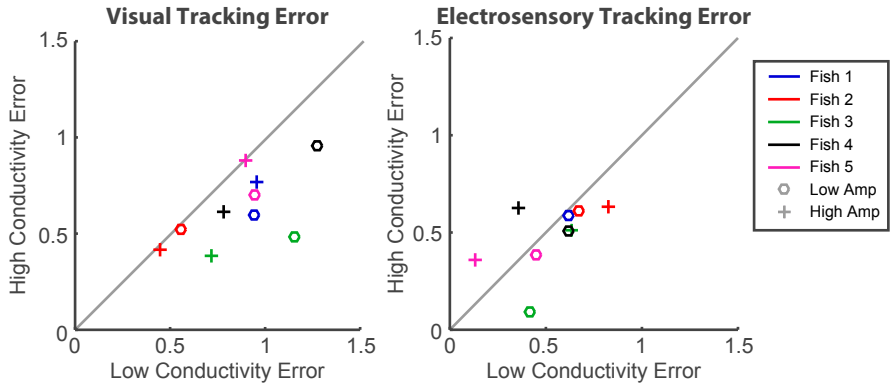

Figure 3.10: **Effect of conductivity on error**. Each fish's mean tracking error, distance from the frequency response point to the point representing perfect tracking, for visual (left) and electrosensory (right) stimuli. The tracking error for vision is significantly lower ($p = 0.038$) at high conductivity across amplitudes, and the trend appears more pronounced for low amplitude stimuli. Electrosensory error was unchanged between conductivity conditions ($p = 0.633$).

3.3.4 Stimulus Amplitude Has Little Effect on Gain

Based on the literature [28], we expected the fish to interpret a lower amplitude probe as more reliable and increase the gain to the probed modality. However, when the visual signal had low amplitude, two of the five fish decreased the magnitude

of the gain to vision. Similarly, one fish decreased the gain to electrosense when the electrosensory stimulus amplitude was low. Gain to the visual stimulus was not affected by stimulus amplitude at either conductivity ($p = 0.340$). Similarly, gain to electrosense was not significantly affected by amplitude at either conductivity ($p = 0.419$). The tracking error was unaffected by the stimulus amplitude for visual ($p = 0.211$) and electrosensory stimuli ($p = 0.749$) for both conductivities. One might expect a significant result from testing a large number of fish, but the failure to detect significance with five fish suggests that any amplitude-dependent nonlinearities are small relative to the variability between conditions.

3.4 Discussion

Robustly interpreting sensory input is central to successful interaction with the environment in general and this tracking task in particular. Our experimental setup enabled us to quantify the change in relative weights given to vision and electrosense during a complex locomotor task. We found that *Eigenmannia virescens* employed flexible, saliency-based locomotor control. Specifically, the animals up-weighted visual information when electrosensory salience was compromised (high conductivity).

3.4.1 Response is Biased Toward Electrosense

Fish routinely showed greater response to electrosensory stimuli than visual stimuli; three fish favored electrosense even at high conductivity for some amplitude conditions. Since *Eigenmannia virescens* is nocturnal, electrosense might be its more biologically relevant sensory modality in the dark, causing it to up-weight electrosense over vision. Analogously, humans show a strong bias toward vision over audition in a spatial tracking task [40]. In both cases, the multisensory interaction seems to be obeying "modality appropriateness" where the modality with the highest appropriateness to a given task dominates [41]. Indeed, we observed oscillatory swimming patterns like those previously associated with no light (electrosensory-only) conditions [14], indicating that in our experiments the fish may have been relying more heavily on electrosensory information than vision. A visual stimulus better matched to the electric fish eye physiology may induce greater the reliance on vision, but research into such physiology remains sparse.

3.4.2 Mulitsensory Integration is Approximately Linear

In a previous tracking study with coherent visual and electrosensory inputs (i.e. a visible physical refuge), the fish's response approximately conformed to the scaling property of linearity [30], so we expected that the response would also obey super-

position across modalities. Indeed, we found that the fish's multisensory integration approximately obeyed superposition. Specifically, the sum of the gains to vision and electrosense in profiles with unimodal probes was approximately equal to the gains measured for coherent, cross-modal stimuli at both low and high conductivity. This result is consistent with previous research on multisensory interaction in insects: in a similar task, flower tracking, freely flying moths obeyed scaling [22] and superposition [27] of vision and mechanosense, and tethered flies showed a linear superposition of visual and olfactory motor responses during odor plume tracking [11].

3.4.3 Salience Drives Gain Ratio

As hypothesized, the ratio of visual gain to electrosensory gain increased at high conductivity, suggesting that the fish re-weighted the open-loop gains to vision and electrosense according to the relative saliency of the sensory inputs. These results are similar to those in a recent study of multisensory integration in sharks in which sharks dynamically substituted alternate modalities during hunting based on sensory and environmental conditions [8]. Analogously, when faced with adverse electrosensory conditions, the fish up-weighted vision to maintain accurate refuge tracking. This up-weighting of vision resulted in significantly lower visual tracking error in high conductivity.

The fish's saliency-dependent response agrees with the human multisensory interaction literature. In a spatial tracking task, when visual uncertainty was low, auditory

signals exerted little or no influence on perceived target location, but with increasing visual uncertainty, the participants demonstrated increased auditory influence [42]. The fish were biased toward electrosense when the electrosensory uncertainty was low, but the weight to vision increased with electrosensory uncertainty. This finding supports the view that multisensory integration is mediated by the relative saliency in individual sensory domains. Strong intramodality dependence enables the nervous system to dynamically adapt to changing environmental conditions.

In a task similar to the one presented here, freely flying moths displayed a small decrease in gain at high frequencies to the motion of the flower during flower tracking in dim conditions compared to bright conditions [22]. Based on this result, we expected to find a decrease in open-loop electrosensory gain at high conductivity, but the closed-loop gain to electrosense did not diminish in this condition. Perhaps the fish produced more active sensing movements to increase the electrosensory contrast; indeed, the fish has been shown to increase the amplitude of its forward-backward oscillations in response to increased conductivity and achieve similar tracking performance across conductivities [14]. These active "wiggles" in the fish's fore-aft movement would have contributed to variability in our estimates of tracking gain at high conductivity but enabled the fish to maintain tracking performance. In this way, active sensing may explain why the electrosensory gain did not decrease at high conductivity even though the magnitude of the gain to vision and the relative gain to vision over electrosense increased.

3.4.4 Reliability and Conflict

Contrary to our third hypothesis, the fish did not decrease gain to a given modality based on a high-amplitude probe stimulus to that modality. In cases where the gain magnitude was higher for high-amplitude stimuli than low-amplitude stimuli, the fish actually moved farther (did more mechanical work) to follow the unreliable signal. This finding differs with results from research in human multisensory integration. For instance, humans were found to down-weight visual information in favor of auditory information in the presence of decreased visual signal reliability (spatial offset) during spatial localization [40]. In another study, humans down-weighted the higher-amplitude stimuli of either touch or vision during postural stabilization [28]. The ability to down-weight unreliable signals is crucial: fall-prone older adults are hypothesized to be more visually dependent, failing to shift reliance toward somatosensory cues in environments where visual inputs are unstable [43]. The discrepancy between our results and these human studies may come from the different task goals: self-orientation versus refuge tracking.

Our results could also be explained by an attentional switch to following the high-amplitude, high-frequency unimodal probe stimulus. At low amplitude, perhaps the sensory illusion was strong; the fish could not distinguish between the probe and base components of the cross-modal input and unconsciously re-weighted the sensory signals (as expected). In the spatial localization tasks, human participants reported being unaware of a spatial discrepancy between the auditory and visual

signals [40]; but we do not have enough information about the fish's visual processing to determine if the fish detected the sensory conflict in our task, and the fish were unable to complete post-trial surveys.

3.4.5 Predictive Models of Multisensory Integration and Control

In the present study, the single probe frequency used here was the minimum necessary stimulus to investigate the phenomenon of multisensory integration and control. A limitation of this approach is that it is impossible to predict the response to stimuli other than sinusoids at the probe frequency. In other words, a model fitted to these data would be underconstrained. Furnishing a predictive dynamical model requires broadband stimuli such as sums of sines [30], band-limited noise [29], chirps [31], and step functions [44].

Determining how the dynamics depend on sensory salience also requires an independent set of perturbations to the quality of the sensory cues themselves. For fish refuge-tracking behavior, this could be achieved by degrading the visual signal—blurred stripes, incoherent pattern movement, etc.—in a way analogous to degrading electrosense through increased conductivity. Ultimately, one could use the responses from these richer stimuli, together with a model of the locomotor mechanics [33], to produce a predictive closed-loop model of control [1, 2]. Such a model might include

Bayesian inference for multisensory integration and state estimation, i.e. a Kalman filter [45].

There are two challenges to developing a Bayesian model of sensory integration in the context of closed-loop control. First, one must understand how the animal interprets the change in saliency and uses it to inform its estimate of the variance of the sensory signal. Second, active sensing behavior violates the separation of sensing and action, an implicit assumption in most engineering approaches to state estimation. An exciting frontier lies in integrating Bayesian inference and active sensing [46, 47].

Part II

Bioinspired Non-Fluoroscopic Catheter Navigation

Chapter 4

Endovascular Navigation

4.1 Introduction

4.1.1 State of the Art in Endovascular Navigation

Approximately eight million vascular procedures are performed under fluoroscopic guidance annually in the United States, and interventional fluoroscopy accounts for 15% of all effective radiation dose from medical sources in the United States [48]. Fluoroscopy has enabled minimally invasive treatments for common vascular conditions. In these percutaneous endovascular procedures, fluorosocpy is used to localize lesions, navigate devices, monitor procedures, and document the end result [6, 49].

However, there are inherent risks such as the radiation dose to the patient [50–52] and interventionalist [53]. The average effective patient dose for an interventional

fluoroscopy procedure is 5-70 mSv, the dose equivalent of 250-3500 chest x-rays [54]. Furthermore, significantly higher dose was reported in patients with a high body mass index [55], those with complex anatomy [56], and those undergoing fenestrated graft procedures [57]. Children, pregnant women, and patients allergic to the contrast agent [58] are especially vulnerable to complications secondary to fluoroscope use. Based on these risks, the National Cancer Institute has called on physicians to optimize patient radiation dose [59]. Aside from the health risks, there is the technical difficulty of estimating the position of a device inside the vasculature based on 2D images, often necessitating multiple contrast injections, guidewire exchanges, and images [49].

There are existing techniques to limit radiation use during endovascular procedures. Previous work by ourselves and others focused on registration of pre-interventional images to live interventional images to track catheters and guidewires [60–63]. Adapting those techniques to endovascular navigation requires deformable registration, a task that has proven challenging due to substantial, unavoidable vessel deformation as devices are inserted and manipulated [64–66]. Additionally, the most successful algorithms are designed for and tested on a specific anatomical region and yield dramatically different results when applied to different vasculatures [60].

Systems using external electromagnetic or electric sources to localize catheters in the cardiac chamber have revolutionized electroanatomic mapping of the heart [67–70]. In particular, cardiac mapping systems like CARTO 3 (Biosense Webster, Diamond Bar, CA), Rhythmia (Boston Scientific, Marlborough, MA), and Ensite

NavX (St. Jude Medical, Saint Paul, MN) have substantially reduced the patient radiation dose during electrophysiological diagnostic and ablation procedures [71–73]. However, these methods have not been successfully implemented for general navigation because the accuracy of the position estimate is greatly diminished in the presence of vessel deformation, patient motion, and unstable heartbeats [69, 74, 75], and the sensing volume is constrained to the cardiac chamber. Additionally, these systems are expensive, require additional hardware, and necessitate significant changes to the surgical workflow [73].

Interventional magnetic resonance imaging (MRI) has also been proposed as an external method of catheter tracking. MRI tracking is especially promising for electrode placement during cardiac electrophysiology, since it could potentially yield nearly real-time 3D position estimates [76]. However, the electroanatomic map and the MRI image tend to lose coherence in the presence of patient respiratory and cardiac motion [77]. Recently, real-time tracking of a catheter using MRI in a mouse model has been achieved, but only for very slow (1 cm/min) and short duration (3 seconds) translations of the catheter [78]. The most accurate methods require custom coated [78] or contrast-eluting catheters [79] [80]. For the foreseeable future, the clinical utility of interventional MRI for endovascular procedures remains uncertain given the technological challenges, cost, and training/workflow modifications required.

4.1.2 Our Proposed Solution

To navigate to a treatment area, the interventionalist is interested in the real-time position of the catheter or guidewire relative to the vessel tree. That is, one only needs a series of consecutive local measurements of the device's surroundings to identify the branch and excursion into the branch. Therefore, a sensor directly on the device's tip could be used to detect features of the local vessel geometry. Our solution, described in the following chapters, integrates bioelectric impedance monitoring by sensors on the device with pre-interventional imaging to estimate the device's position in the vessel tree.

4.2 Dissemination and Organization

Parts of this work were published in a conference paper and presented orally at the 2016 Medical Image Computing and Computer Assisted Interventions Conference [81]. The tumor-monitoring system outlined in Chapter 9 has been disclosed as an invention to Johns Hopkins Technology Ventures. Chapter 5 introduces the theory and inspiration underlying bioelectric sensing and navigation. Chapter 6 presents experimental validation in synthetic vessel phantoms. Chapter 7 documents the system's validation in biological tissue. Chapter 8 outlines the development and preliminary testing of a novel guidewire designed for bioelectric sensing and navigation. Finally, Chapter 9 summarizes the next steps recommended for the project before

commercialization efforts can begin.

4.3 Contribution

Bioelectric Sensing and Navigation was conceived by Noah Cowan, Nassir Navab, Bernhard Fuerst, and Eric Fortune, and a patent application was filed in 2014 as: US2014/0276190 System and Method for Bioelectric Localization and Navigation of Interventional Medical Devices. I joined the project in 2013 and performed much of the hands-on research and development since then. In particular, I was independently responsible for all of the simulations, experiment design and execution, clinical applications research, clinical collaboration, and mechanical design. Additionally, I led the drafting and submission of all conference papers, journal articles, and grants. I also made significant updates to the literature review, signal processing, and analysis software.

Chapter 5

Bioelectric Sensing and Navigation Theory

5.1 Introduction

5.1.1 Bioelectric Sensing and Navigation Concept

To navigate to an area of interest, the interventionalist requires feedback about the current position of the catheter relative to the vessel tree. We realized that a sensor directly on the catheter tip could be used to detect features of the local vessel geometry without Fimage registration or external sensors. Crucially, the interventionalist does not aim to "image" the surrounding vessel during navigation, simply navigate through it. Our proposed system, Bioelectric Sensing and Navigation (BSN) compares a local

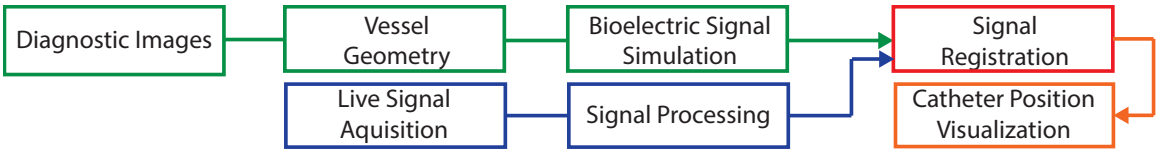

Figure 5.1: **Schematic diagram of BSN**. Software registers the live bioelectric measurements from the catheter to the simulated signals from a pre-interventional image to determine the catheter's estimated position.

measurement from sensors on the catheter to predicted measurements from a pre-interventional image to identify the global position of the catheter relative to the vessel tree (Fig. 5.1).

5.1.2 Sensorized Catheters

The first step in implementing BSN is to identify an appropriate sensor technology with which to augment the catheter. Intravascular ultrasound (IVUS) has been in clinical use for two decades, and its most valuable application has been plaque visualization [82]. To perform an IVUS examination, the ultrasound catheter tip is positioned at the distal end of the area of interest. Echogenic elements include the blood vessel wall inner lining, atheromatous disease within the wall, and connective tissues covering the outer surface of the blood vessel. Blood and the healthy muscular tissue portion of the blood vessel wall is relatively echolucent. The ultrasound catheter is slowly pulled back under motorized control over short distances. IVUS does not localize the plaque; the sensorized catheter still must be tracked using fluoroscopic images.

An alternative to IVUS is optical coherence tomography (OCT), an optical imaging technique primarily used to generate high-resolution cross-sectional images of tissue. Analogous to B-mode ultrasound imaging, an OCT device measures the intensity of back-reflected near-infrared light to measure the thickness of different biological tissues. OCT was first introduced for transparent tissues like those in the eye [83, 84] but was quickly adapted to imaging the GI tract [85], skin surface [86], brain [87], and vasculature [88]. In blood vessels, the signal is greatly attenuated in areas of high red blood cell turbulence, so the vessel must be flushed with saline before a scan and OCT can map only very short arterial segments at a time. [88]. Because it uses light instead of sound, OCT has significantly higher spatial resolution than ultrasound. However, its penetration distance is only 2-3 mm, limiting its use in larger vessels. Finally, while it has recently been shown effective at differentiating thin-cap fibroatheroma from less vulnerable plaques [89], Like IVUS, OCT does not localize the plaque; the sensorized catheter still must be tracked using fluoroscopic images. OCT is a very promising diagnostic tool but is not appropriate for integration into our catheter tracking system. OCT and IVUS can be used together [90] (Fig. 5.2) or with additional imaging [82, 91] for diagnostic purposes.

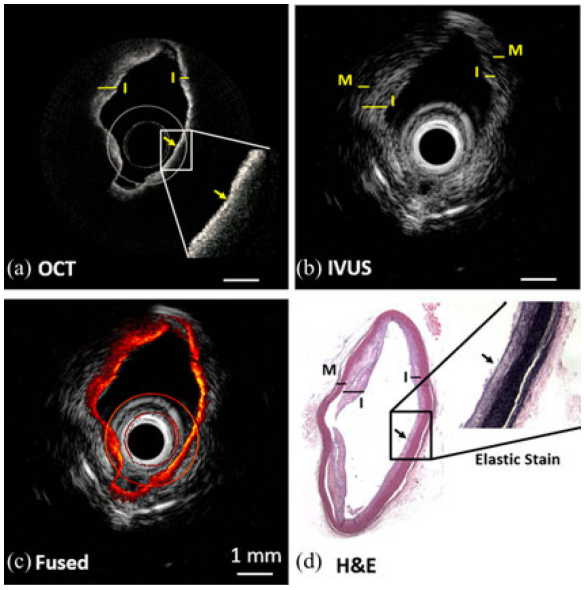

Figure 5.2: **OCT and IVUS a)** In an atherosclerotic rabbit aorta with eccentric plaque, elastin layers are visible on the OCT cross-section. **b)** The IVUS cross-section shows the media of the blood vessel, not visible in the OCT image. **c)** Fused OCT/IVUS cross-section. **d)** Histology images showing both layers of the vessel and the elastin layer. Figure from [92].

5.1.3 Bioinspiration

Given the disadvantages associated with existing catheter-based sensors and our experience with weakly electric fish, we investigated the application of the fish's electrosensing capabilities. This fish has an electric organ that discharges a signal, generating a weak electric field around its body. The electrical current flowing through the epidermis of the fish allows the measurement of the amplitude and phase, which is referred to as the "electrical image". If an object is within the range of propagation of the signal, it influences the field, and the distribution of the measured signal changes (Fig. 5.3). Based on the electrical properties of the object, the electrical image is distorted [93]. Studies have shown that weakly electric fishes not only consider the intensities of the responses but also the modulation on the surface, the normalized modulation and the slope-to-amplitude ratio to detect the distance [94, 95], material, size [96] and electrical properties [93] of surrounding objects individually. Furthermore, fishes are able to change the type of discharge to inspect objects in more detail. It has been recently shown that by altering its own shape, a weakly electric fish not only increase its sensing volume, but is also able to obtain modality-specific information from the sensing feedback [97].

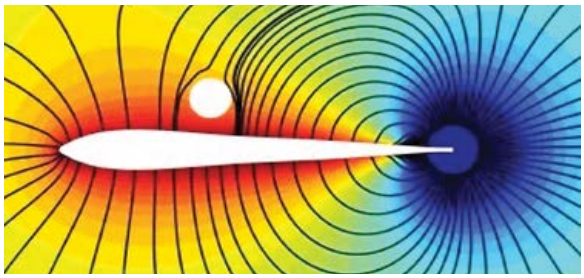

Figure 5.3: **The electric field of a weakly electric fish.** The color indicates voltage, and the equipotential field lines are black. The object with higher impedance than water leads to decreased current density in the area around the object, causing a perceived voltage amplitude decrease at the electroreceptors close to it and making the object visible. Like the fish, the proposed catheter sends out a signal and measures the disruption to its electric field caused by the vessel wall, providing a highly localized measurement of its surroundings. From [97].

5.2 Theory Underlying Bioimpedance Acquisition

5.2.1 Impedance measurement

Like the fish, our sensorized catheter measures changes to its self-generated electric field to sense its local surroundings. Electrodes distributed near the catheter tip simultaneously create a weak electric field and measure the impedance. The impedance of blood is much lower than that of vessel walls and surrounding tissue [98], so the catheter detects local vessel geometry (bifurcations, stenoses, aneurysms) from measured impedance changes. It is based on Ohm's Law, which is as follows:

$$Z_T = V/I = \frac{L}{A\sigma} + Z_p \tag{5.1}$$

Total impedance, Z_T, is measured by the electrodes on the guidewire, blood conductivity, σ, is known and constant, L is the known distance between the electrodes, and parallel impedance, Z_p is proportional to cross-sectional area, A. Therefore, relative changes in vessel cross-sectional area are detected by changes in Z_T, measured by the electrodes. In practice, as the device passes a bifurcation, it detects a significant disturbance to the electric field caused by the dramatic increase in vessel cross-sectional area. The catheter records those disturbances over time to get a distinctive profile of the path taken through the vessel tree.

5.3 Bioimpedance in Medical Research

Bioimpedance has been used for measuring vital physiological parameters such as blood flow and blood constituents [99] as well as conditions like internal hemorrhage, muscle injury, and prostate cancer [100, 101]. Endovascular bioelectric sensing aims to adopt this impedance measurement to estimate the internal geometry of the blood vessel.

5.3.1 Tissue Classification

Endovascularly, the primary use of electrolocalization is tissue classification for detection of plaque. By simulating the electrical field on a plane around the catheter using the Poisson equation, researchers have shown the potential of bioelectric signals

to classify tissue in two dimensions [93, 102–104]. However, for catheter localization and navigation, it is not sufficient to simulate the electrode-electrolyte interface on a two-dimensional plane. The simulation identified the presence of plaque but not its location, limiting the clinical utility of their proposed device for navigation. Still, it points towards the feasibility of our proposed technique, because there appears to be a significant change in the electric image when objects are introduced into the environment.

5.3.2 Cross-Sectional Area Measurement

Researchers have also introduced impedance-measuring catheters for accurate and reproducible measurement of vessel cross-sectional area (CSA) [105]. Their method is not appropriate for navigation because it requires a stationary catheter and injections of saline at two conductivities. However, some of their results support bioelectric navigation since the catheter itself is similar to ours. The key results were equations relating vessel and catheter diameter and *ex vivo* validation of the CSA measurement. In simulation, the authors found that the voltage potential tends to be fairly uniform in the vessel lumen domain followed by an exponential decay into the surrounding tissue for both concentrations of saline. The drop-off at the vessel wall seems relatively gradual. This is encouraging for our experiments because it means that when the catheter is slightly off-center in the cross-section, we can still expect a reasonable impedance signal. The authors combined all of their data and found the optimized

relationship between vessel diameter, D_v, and catheter diameter, D_c, in mm:

$$D_c = -0.064D_v^2 + 1.07D_v - 2.35 \tag{5.2}$$

Unlike the authors of that study, we do not aim to accurately measure the vessel CSA; instead, we measure the relative change in voltage due to CSA variations. Nevertheless, this finding suggests that a 6F catheter like the one used in our experiments would experience the least distortion in 7-10 mm diameter vessels. A smaller 0.889 mm diameter guidewire would be more appropriate for 3.5-7 mm vessels.

5.4 Bioimpedance Enables Catheter Navigation

The generation and measurement of bioelectric signals within vessels and their mapping to a patient-specific vessel model has never been proposed for endovascular navigation. By identifying the path corresponding to the real-time signal from the catheter, our software informs the interventionalist of the most likely position of the device relative to the vascular tree. In this fashion, BSN bridges the gap between catheter-based sensing and catheter navigation. The local voltage measurement from the catheter is compared to predicted "reference" measurements derived from a pre-interventional anatomical model to identify the global position of the catheter relative to the vessel tree. The generation of those reference measurements is addressed in

the following sections.

5.4.1 Simulation

A complete bioimpedance model requires solution of the 3D Poisson equation, assuming known permittivities of blood and tissue. Given a relatively simple geometry, one can employ finite element analysis to numerically solve for the electric potential distribution. For our first feasibility experiments, we designed an eight-path vessel phantom with two stenoses and one aneurysm. We imported the 3D CAD model into Comsol Multiphysics (COMSOL, Inc., Stockholm, Sweden) and simulated the signal as a two-electrode catheter passed through the six primary branches (Fig 5.4a). The simulation yielded six distinct models, one for each path. For a synthetic vessel tree, the simulated voltage at the emitting electrode was inversely proportional to the cross-sectional area extracted from the cone-beam CT (CBCT) (Fig 5.4b). We conclude that cross-sectional area is adequate for localization with a two-electrode catheter, the minimum required for Bioelectric Navigation.

The simulations greatly simplify the algorithm that maps the temporal electric signals to the spatial vessel information. Furthermore, they enable the modeling of difficult, but realistic, scenarios such as the influence of contact with a vessel wall or the presence of stents. We require that the catheter be able to detect branchings significantly smaller than then primary vessel, and this simulation framework provides the means to modifiy the acquisition strategy to achieve this goal. In particular, the

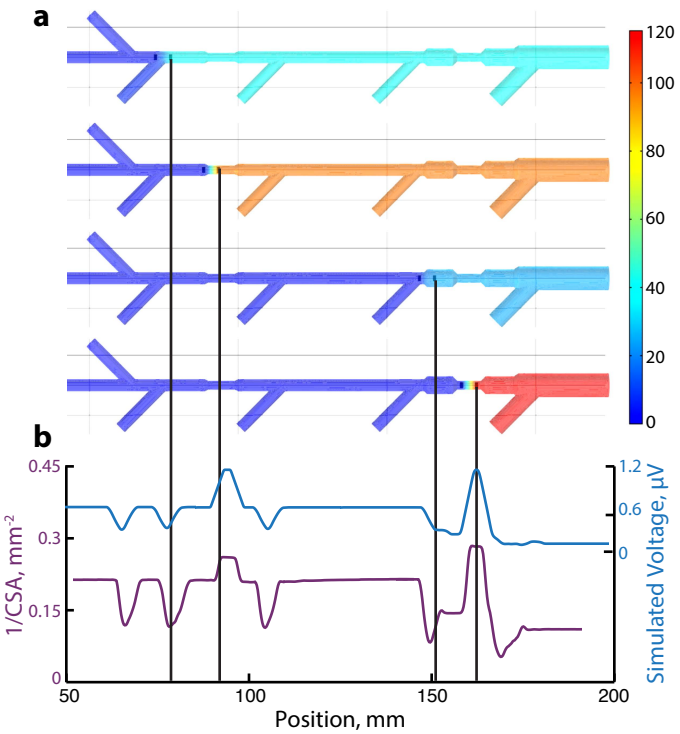

Figure 5.4: **a)** Simulation of synthetic vessel phantom from imported CAD geometry. The electrodes (black) span the left-most stenosis in the top image. The voltage decreases at a bifurcation and increases at a stenosis. **b)** Simulated voltage magnitude (blue) and the inverse of the cross-sectional area (purple) from the segmented CBCT.

simulation framework we developed enables the efficient evaluation of changes to the localization system (e.g. signal modulations, electrode configurations, catheter diameters).

5.4.2 Vessel Segmentation and CSA Extraction

There are many methods for the segmentation of the vascular tree in CT images, and selecting the optimal method is not a contribution of this work. In fact, our system is largely invariant to the segmentation algorithm chosen. It uses the relative variation between segments to guide the catheter, so as long as it captures major geometric features, the extracted model need not have high resolution. We use a few methods of segmentation in the following experiments, all based on the open-source Vascular Modeling Toolkit (vmtk.org). First, we select segmentation parameters specific to the imaging modality (e.g. threshold, shape, background suppression) based on published techniques [106, 107]. After manual initialization at an entry point, the algorithm detects the centerline and the shortest path between two points in a vessel-like segmentation. It generates the wire mesh vessel model. With that model, we use commercial and custom software to compute the cross-sectional area at each segment for each possible path.

Chapter 6

Bioelectric Sensing and Navigation Benchtop Testing

6.1 Benchtop Sensing Validation

Before I began work on this project, initial tests of the catheter in a phantom made of tubing indicated that the catheter successfully detected bifurcations [108]. The experiments that we first conducted and that are outlined in this section tested two additional aspects of sensing: Could the commercially available catheter with ring electrodes be used to detect from which side a bifurcation branched off of a vessel? How would the measurement be affected by blood flow? These proof-of-concept experiments form the basis for later work.

6.1.1 Signal Generation and Measurement

The electronic equipment for signal generation and measurement was kept constant throughout the experiments in this chapter, unless otherwise noted. A function generator supplied a sinusoidal signal to the current source, and the current source supplied a constant μA-scale signal to the emitting electrode on the catheter (Fig. 6.1). A neighboring electrode was grounded. The signal between the two electrodes was amplified and filtered by a low-power biosignal acquisition system (RHD2000, Intan Technologies, Los Angeles, USA). The Intan software (Intan Interface 1.4.2, Intan Technologies, Los Angeles, USA) logged the AC voltage measurement from the electrodes at 25 kHz and filtered the signals. Finally, a sliding window discrete Fourier transform converted the signal into the frequency domain, and the magnitude at the input frequency was extracted for each window. In this fashion, the input signal enabled relatively simple signal identification. Although real-time implementation is crucial to navigation, all of these experiments involved only post-hoc analysis.

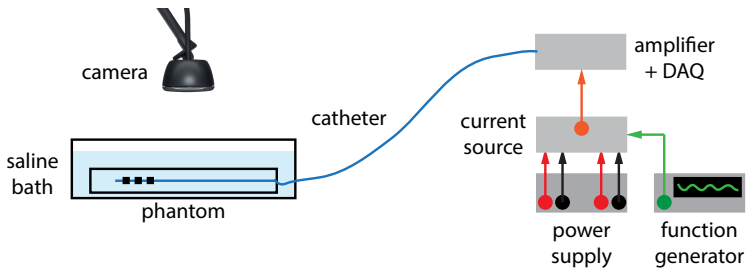

Figure 6.1: **Schematic of Signal Generation and Recording**. The phantom is placed in a saline bath. A camera captures video as the catheter advances through the phantom. A power supply powers the constant current source, and a function generator provides the input AC signal to the current source. The measured signal from the catheter is amplified and recorded by a DAQ. The voltage data collection and the video recording are synchronized such that the position of the catheter is verified by the video throughout each trial.

6.1.2 Detection of Branch Orientation in Rectilinear Phantom

We would eventually like to detect the orientation of a branching vessel relative to the trunk. Essentially, we would like a 2D reading (CSA and branch orientation angle) rather than a 1D CSA signal. Because all of our catheters have ring electrodes rather than arrays, as a preliminary test, we occluded half of the input electrode to measure changes on one side of the vessel.

6.1.2.1 Methods

We used a 6F cardiac electrophysiology catheter (MultiCath 10J, Biotronik, Berlin, Germany). Its ten ring electrodes were 2 mm wide with 5 mm spacing. The input to the current source was ±5 mV at 430 Hz, and the current source supplied a con-

stant 18 μA to the emitting electrode, Electrode 2. we occluded part of Electrode 2 by puncturing a 0.5 cm length of heat shrink tubing before shrinking it over the catheter.

We designed a custom phantom for this and several subsequent experiments. It is designed like a mold, with channels cut into the top and bottom pieces. The two halves of the phantom were machined from acrylic and sealed with a thin layer of transparent waterproof grease. When assembled, it measures 10 cm $\times$ 25.4 cm $\times$ 5 cm. The paths are $3-10$ mm diameter. The experiment was conducted in main path of the phantom. The phantom was immersed in 0.9% saline to simulate blood.

For the first pass, the exposed part of the input electrode faced Path 1 (Fig. 6.2a). For the second pass, the exposed part faced Paths 2-5. A camera recorded the trajectory of the catheter. The catheter was manually pulled through the phantom at $1-2$mm/s. Four replicates were performed for each direction.

6.1.2.2 Results

When the exposed part of the input electrode faced toward a bifurcation, that branch's impact on voltage magnitude was greater than when the occluded portion faced the same branch (Fig. 6.2).

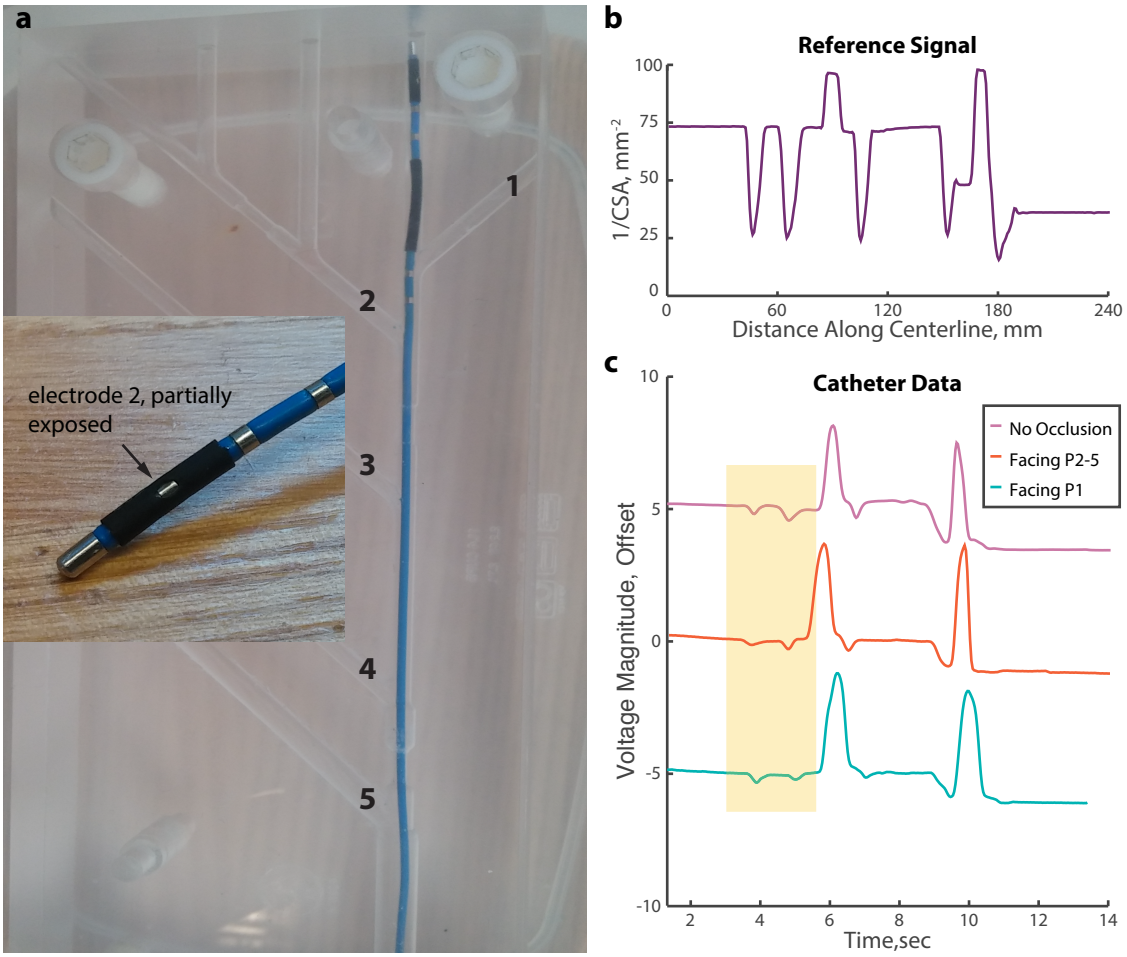

Figure 6.2: **Exemplary Result from Branch Orientation Experiment. a)** Initial catheter position in the rectilinear phantom. Electrode 2 has been partially occluded. The exposed portion of the electrode is facing Path 1 in this photograph. **b)** The reference signal is the inverse of the cross-sectional area along the centerline of the phantom's main branch. **c)** Voltage magnitude measured by the catheter as the catheter was pulled back through the main branch. The teal and pink traces are offset by -5 mV and $+5$ mV, respectively.

6.1.3 Simluated Blood Flow in Rectilinear Phantom

Arterial catheters are generally advanced from a peripheral insertion point toward the heart, so we conducted a preliminary study of the effect of flow on the catheter's voltage measurement. A peristaltic pump connected to the acrylic phantom simulated a beating heart.

6.1.3.1 Methods

The same catheter, input signal, and phantom were used for this experiment as were used in the previous experiment. A peristaltic pump (MityFlex 907, Anko Products, Bradenton, FL). The flow rate was approximately 200 mL/min with 1/4" ID tubing connecting it to the trunk of the phantom. The pump "beat" at 58 RPM. The catheter was advanced against the flow, as it would be during an intervention.

6.1.3.2 Results

There was no discernible difference in voltage between the trials with the pump on and those with the pump off (Fig. 6.3). In this case, flow did not have a significant impact on the voltage magnitude. This result agrees with a study that demonstrated in simulation, *ex vivo*, and *in vivo* experiments that saline injection changes the flow characteristics but doesn't negatively affect lumen measurement by a conductance

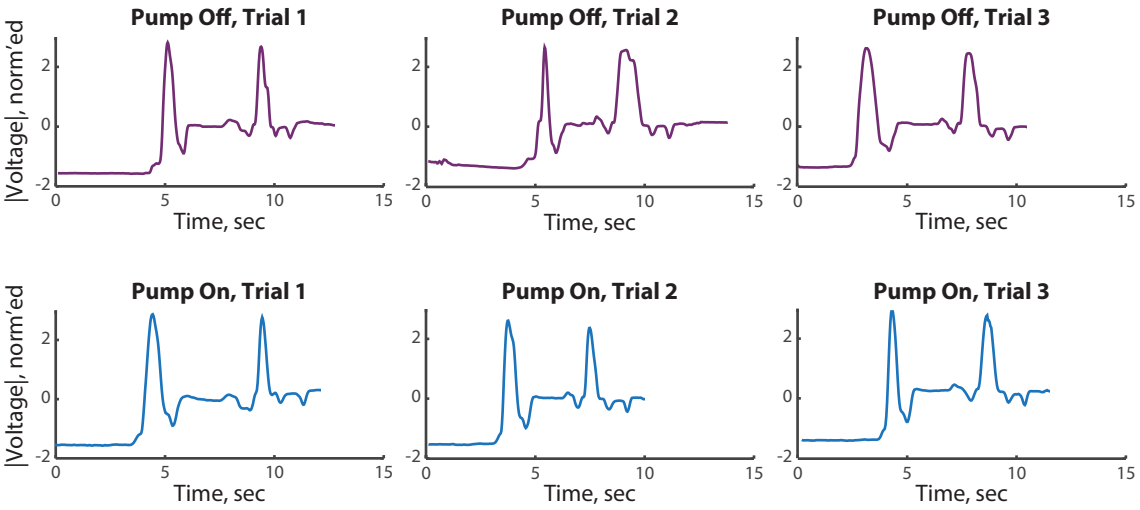

Figure 6.3: **Results from Flow Experiment.** The variation toward the end of some trials, especially visible in "Pump Off, Trial 1", is due to the catheter being pushed into the mouth of the inflow fitting.

catheter [109]. However, it is possible that the voltage would be affected by the alignment of red blood cells, so validation with whole blood should be performed. This was a primary factor in deciding to perform an *in vivo* study outlined in Chapter 7.

6.2 Benchtop Matching Validation

6.2.1 Modeled and Empirical Signal Matching

The bioimpedance signal is a scaled and time-warped version of the vector of vessel cross-sectional areas, so the alignment of measured bioimpedance from the catheter with the modeled vessel tree is the foundation of our technique. While we are investigating other alignment methods, in these initial experiments we use open-

ended dynamic time warping (OE-DTW) [110]. OE-DTW was chosen because it can be adapted to provide feedback to the interventionalist during a procedure, and it includes a similarity measure that enables the determination of the most likely position of the catheter with respect to the vessel model.

OE-DTW enables the alignment of incomplete test time series with complete references. Ideally, the incomplete voltage series during a procedure is incrementally compared to each of the complete references from the model to obtain constant feedback about the predicted location of the catheter. In our implementation, cross-sectional area along each path forms the reference dataset, and the experimentally measured voltage magnitude is the test time series.

Since it is not our original work, we omit details of the OE-DTW algorithm. A full explanation can be found in Tormene et al. [110]. There are a few parameters specific to our implementation of the OE-DTW algorithm, and they are listed in Table 6.1. Note, it is rarely useful to start matching from a very short reference signal since that would represent very little progress down a given path. Therefore, to save computation time, the minimum fraction of the reference signal tested, *minper*, was 85% unless otherwise noted.

Table 6.1: Parameters used in OE-DTW implementation

Parameter Name	Symbol	Value
normalization function	$\nu(N, j)$	$N + j$
slope weight	w_d,w_r,w_c,	1
min reference length	*minper*	0.85

6.2.2 Navigation in Rectilinear Phantom

6.2.2.1 Methods

The same catheter, input signal, and acrylic vessel tree phantom were used for this experiment as were used in the previous experiment. A camera recorded the trajectory of the catheter through the phantom as it was manually advanced through the six main paths at $1 - 2$mm/s. Five replicates for each path were performed, all with different and unknown catheter velocity.

6.2.2.2 Results

The OE-DTW algorithm correctly identified the path taken in 25/30 trials. The similarity measure was 0.5245 ± 0.0683 for misidentified trials and 0.6751 ± 0.1051 for correctly identified trials.

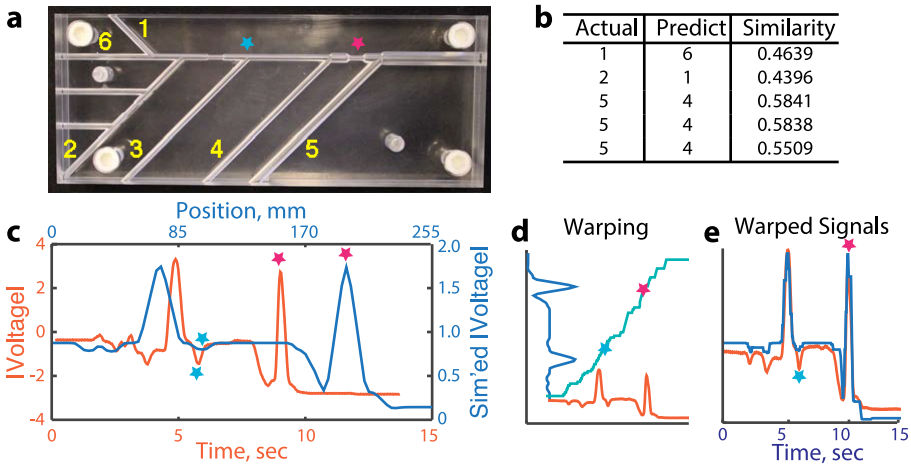

Figure 6.4: **Navigation in Rectilinear Phantom) a)** Rectilinear phantom with labeled paths. **b)** Trials for which OE-DTW incorrectly predicted catheter position.**b)** The measured voltage (blue) and the simulated signal (green) identify the two stenoses and four bifurcations. The signals appear correlated but misaligned. **d)** The OE-DTW algorithm found a correspondence path between the two signals. **e)** OE-DTW aligned the simulated data to the measured data and calculated the cross-correlation between the two signals.

6.2.3 Navigation in Anatomical Phantom

6.2.3.1 Methods

This experiment was conducted in a custom 3D-printed (multijet modeling process) UV-cured acrylic phantom (Fig. 6.5). This phantom was designed with anatomically relevant branching, CSA, and tortuousity. It has threaded inlets and outlets to enable easy connection to tubing. Furthermore, the phantom is designed to interface with the same components used in the operating room: Luer-lock fittings, guidewires, and introducer sheaths. The phantom is filled with 0.9% saline solution and a catheter is introduced through a sheath.

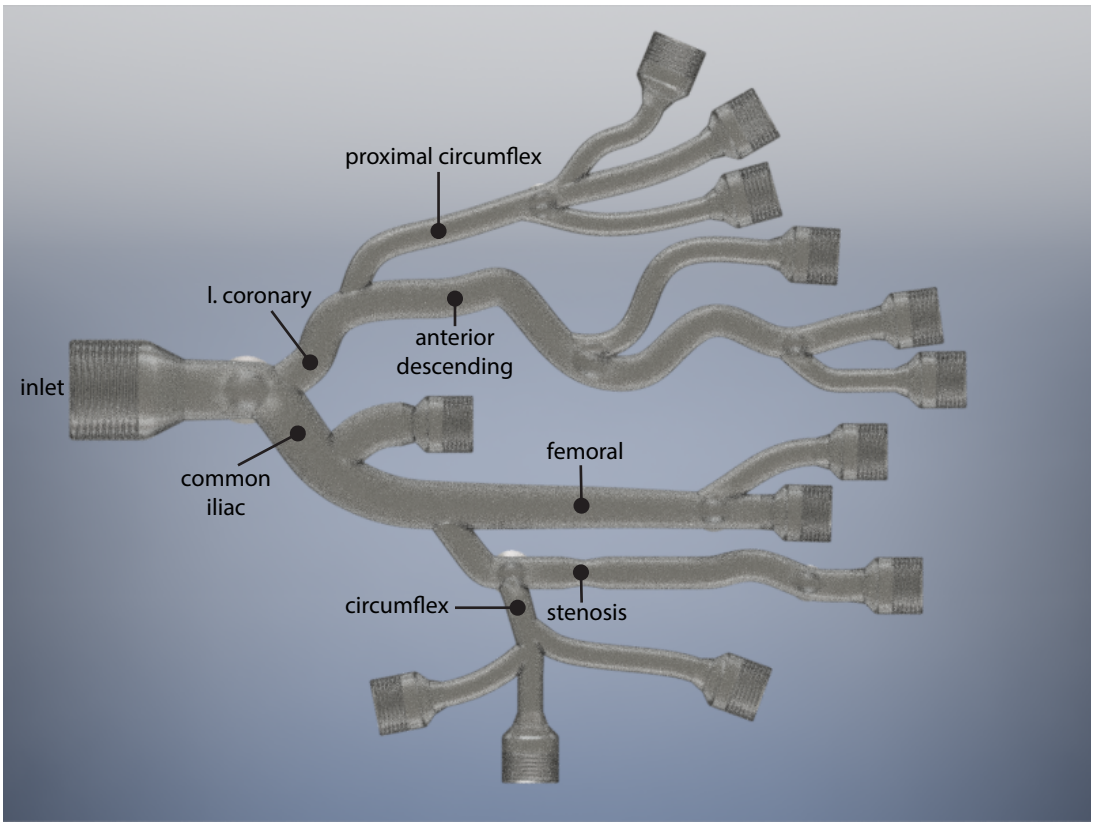

Figure 6.5: **Rendering of 3D-Printed Anatomical Phantom.** In this image, the top half of the phantom is modeled after the branches of the left coronary artery. The bottom half mimics the branches of the external iliac artery. The entire phantom measures 22 cm $\times$ 16 cm $\times$ 4 cm, and the interior diameters are $3 - 10$ mm. For durability, we coated the exterior of the phantom in clear epoxy.

Before the experiment, we computed the cross-sectional area along the centerlines of six paths of the phantom. These unique cross-sectional area profiles representing the possible paths of the phantom served as the reference signals for the signal matching algorithm (Fig. 6.6a).

To navigate through the tortuous vessels, we used a steerable commercially available cardiac electrophysiology catheter (ViaCath 5F, Biotronik, Berlin, Germany). We recorded the voltage as the catheter was manually advanced through six of the

phantom's paths, which yielded a unique voltage magnitude signal for each branch. Video was recorded simultaneously with the voltage to confirm the catheter's trajectory during each trial. Four replicates were performed for each path for a total of 24 trials.

Given the more complex phantom geometry, this experiment merited more analysis than the previous, so we also investigated the ways in which the classification algorithm failed. we created a normalized distance measure, d, to compare signal matching between paths:

$$d = \frac{D(i_2) - D(i_1)}{D(i_1)} \tag{6.1}$$

Here, i_1 is the index of the best-matched path and i_2 is the index of the second-best-matched path. Then, $D(i_1)$ is the minimum OE-DTW distance between a given test signal and all of the reference signals. In other words, $D(i_1)$ is the distance between the test signal and the reference to which it has been matched. Similarly, $D(i_2)$ is the distance between the test signal and the second-best-matched reference. Therefore, d gives a scaled measure of how well the algorithm has discriminated between reference signals for a given test signal. As d approaches zero, the best and second-best matches become indistinguishable.

6.2.3.2 Results

For complete test signals, the algorithm correctly classified the test path in 19/24 trials (Fig. 6.6c). When it failed, the second-best match was consistently the correct

path. That is, the correct classification was always in the algorithm's top two choices for best match.

Paths with substantial overlap are not distinguished very well. For instance, Path 3 and Path 4 are identical for 95% of their lengths, so the distance between a test signal from either path and a reference from either path is dominated by the large fraction of the distance matrix that they share in common.

In Figure 6.6c, τ is the estimated accuracy $\pm$ the 95% confidence interval computed using the textbook limit as defined in [111]:

$$\tau = \epsilon \pm \left(\frac{0.5}{M} + 1.96 \sqrt{\frac{\epsilon(1-\epsilon)}{M}} \right) \tag{6.2}$$

where ϵ is the mean accuracy and M is the number of predictions for a given test path. Paths 1, 2, and 6 were the most accurately predicted, Path 4 was confused for Path 3, and Path 5 was confused for Path 6 (Fig. 6.6c).

We also considered the normalized distance measure for correctly classified trials, d (mean $\pm$ one standard deviation) Eqn. (6.1). We expected that for paths with lower classification accuracy, the distance between the best and second best classifications would be low. The data generally bear out this trend. Note that the converse is not necessarily true; Path 1 was accurately classified but "close" to being classified as Path 5.

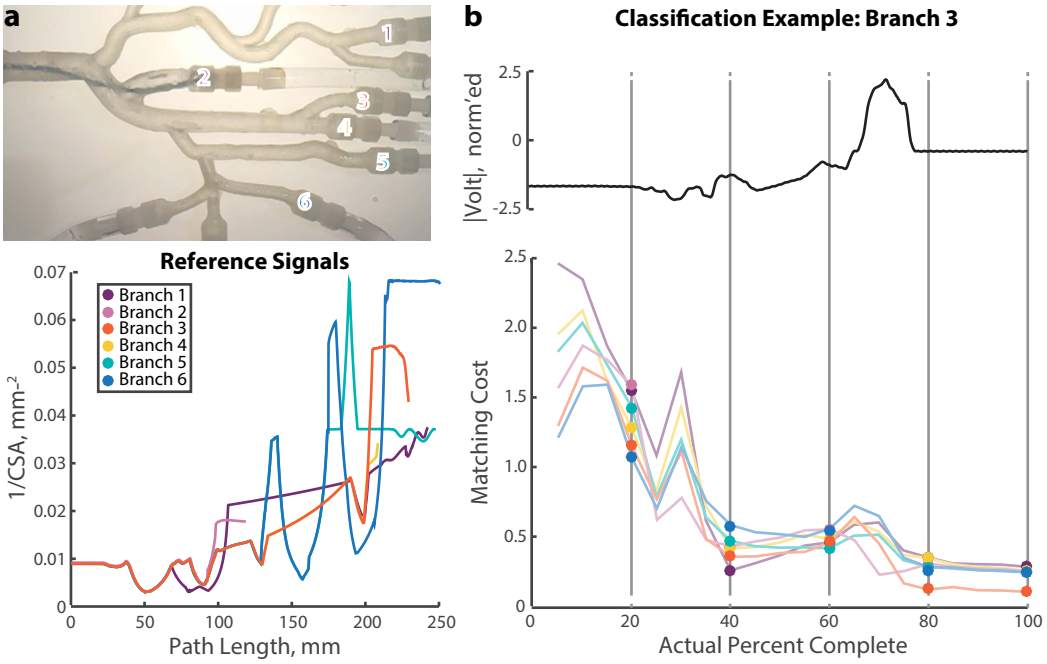

c Classification Performance

Actual Path \ Predicted Path	1	2	3	4	5	6
1	4	0	0	0	0	0
2	0	4	0	0	0	0
3	0	0	3	1	0	0
4	0	0	2	2	0	0
5	0	0	0	0	2	2
6	0	0	0	0	0	4

Path	τ	$d_{correct}$	i_2
1	1.0-0.125	0.034±0.120	5
2	1.0-0.125	0.166±0.020	4
3	0.75±0.549	0.057±0.025	4
4	0.5±0.615	0.023±0.003	3
5	0.5±0.615	0.063±0.044	6
6	1.0-0.125	0.074±0.056	5

Figure 6.6: **Navigation in Anatomical Phantom a)** Phantom with six paths marked. The catheter was manually advanced from the trunk on the left side of the photograph into the branches on the right. The catheter is in Branch 2 in this image. Below, the reference signals for this experiment were the inverses of the cross-sectional areas extracted from the CAD geometry. Each trough represents bifurcation or widening, and each peak indicates a stenosis or narrowing. **b)** In this example, the catheter traveled through Branch 3. As it progressed, the matching algorithm computed a matching cost between the incomplete test signal and all possible lengths of each reference signal. The branch with the lowest cost was selected as the most likely location of the catheter. **c)** The matching algorithm correctly classified the test path for 19/24 trials.

6.3 Discussion

Classification accuracy was lower for the anatomical phantom than for the rectilinear phantom. It is possible that the discrepancy can be explained by the behavior of the electric field as the catheter bends. That is, in the more tortuous vessels of the anatomical phantom, the catheter's electric field was not accurately modeled in the cross-section of the vessel. To test this hypothesis, COMSOL modeling of the electric field inside the anatomical phantom could be performed in future studies.

Similar trials were misclassified in both the rectilinear (Paths 1 and 6) and anatomical (Paths 3 and 4) phantoms. Clinically, this result indicates that it is difficult to distinguish between two branches of a vessel unless the catheter travels a considerable distance down either branch. However, this is not expected to negatively affect the clinical workflow. In the clinical state-of-the-art, catheter tracking with fluoroscopy, clinicians routinely employ a "guess and check" method of advancing the catheter, checking its position on a fluoroscopic image, and re-positioning the catheter. Our algorithm requires the same movement of the catheter, but without relying on x-ray acquisition for feedback.

Furthermore, for cases in which the distance between a test and two possible references is small, we envision our algorithm prompting the clinician to take an x-ray image to confirm the position of the catheter. At that point, we could use existing software methods to localize the catheter in the x-ray image [63, 112]. Then the interventionalist can, at any time, verify the position of the catheter and our algorithm

will use the position extracted from the x-ray image to inform the subsequent position estimates.

Chapter 7

Bioelectric Sensing and Navigation Validation in Biological Tissue

7.1 Introduction

The magnitude of the bioelectric signal depends on the impedance difference between tissues. Because the impedance difference between saline and vessel is less dramatic than between saline and acrylic, we expected lower amplitude signals in biological tissue. To test the effect, we first validated the catheter sensing and navigation in *ex vivo* biological tissue. Finally, we conducted a preliminary *in vivo* investigation.

7.2 *Ex Vivo* Bioimpedance Sensing

The first experiment in biological tissue tested the relationship between voltage difference at consecutive electrodes and cross-sectional area variation in biological tissue.

7.2.1 Methods

7.2.1.1 Signal Generation, Measurement, and Analysis

We used a 6F cardiac electrophysiology catheter (MutliCath 10J, Biotronik, Berlin, Germany). Its ten ring electrodes were 2mm wide with 5mm spacing. The input to the current source was a sine wave at ±250 mV at 2300 Hz. The current source supplied a constant 60 μA to the emitting electrode. A neighboring electrode was grounded. The voltage between the two electrodes was amplified and filtered by a low-power biosignal acquisition system (RHA2000, Intan Technologies, Los Angeles, USA). A higher amplitude and frequency than previous experiments was required with the analog acquisition system used for this experiment. Note that all other experiments used the digital RHD2000 system. The Intan software (Intan Interface 1.4.0, Intan Technologies, Los Angeles, USA) logged the signal from the electrodes. A windowed discrete Fourier transform converted the signal into the frequency domain, and the magnitude at the input frequency was extracted from each window.

For this simple experiment, a linear actuator drove the catheter through a porcine

aorta of known geometry at a constant velocity, so there was no need for synchronization methods (e.g. Dynamic Time Warping) to align the CSA measurements and voltage signals.

7.2.1.2 Experimental Procedure

The porcine aortae used in this and subsequent experiments were procured fresh from a local meat processing facility. They were rinsed with cold tap water, stored in an airtight plastic bag with most of the air removed, and refrigerated overnight. The specimen for this experiment came from an adult female Berkshire swine. We sutured the specimen to a piece of foam board and submerged it in saline. The linear actuator drove the catheter through the main path at 11 mm/s.

7.2.1.3 Reference Signal Acquisition

To obtain the reference signal set, a CT of the aorta was collected at Johns Hopkins Hospital using a clinical CT machine. The CT was processed and the vessels segmented, and the radii of the maximum inscribed spheres along the centerline were extracted using Vascular Modeling Toolkit (https://www.vmtk.org).

7.2.2 Results

The results indicate that the voltage signal can form an electric image of the vessel cross-sectional area changes (Fig. 7.1). In particular, the catheter measured a large

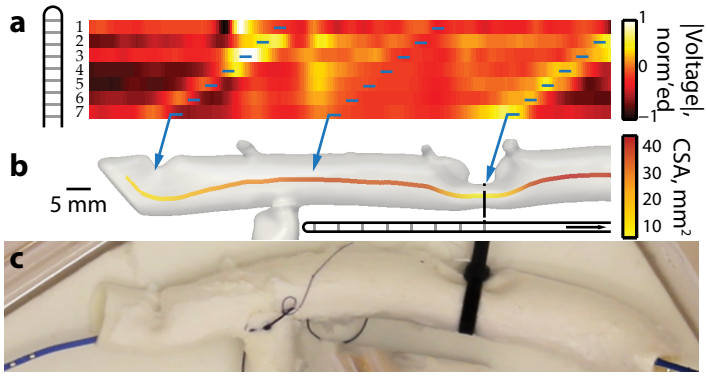

Figure 7.1: **First Experiments in Biological Tissue a)** Normalized voltage difference between consecutive electrodes as the catheter was pulled from left to right through the specimen. Bright areas correspond to diameter changes. **b)** CT of biological specimen with radius overlay. The blue arrows indicate the anatomical features corresponding to the bands in the voltage plot. The black dashed line indicates the position of the catheter in the stenosis at the moment when the seventh and eighth electrodes span a dramatic diameter change, causing an associated peak in the voltage difference plot. **c)** Photograph of the biological specimen (porcine aorta) in 0.9% NaCl solution.

voltage difference at the stenosis.

7.3 *Ex Vivo* Matching Validation

While the previous experiment suggested that the catheter strongly detected stenoses, the bifurcation was not visible in the cross-sectional area because the method of centerline extraction used neglects small bifurcations. For the next experiment, we created a Y-shaped biological phantom with two porcine aortae to test bifurcation detection.

7.3.1 Methods

7.3.1.1 Signal Generation, Measurement, and Analysis

We used a 6F cardiac electrophysiology catheter (MutliCath 10J, Biotronik, Berlin, Germany). Its ten ring electrodes were 2mm wide with 5mm spacing. The input to the current source was a sine wave at ± 5 mV at 430 Hz, and the current source supplied a constant 18 μA to the emitting electrode. A neighboring electrode was grounded. The voltage between the two electrodes was amplified and filtered by a low-power biosignal acquisition system (RHD2000, Intan Technologies, Los Angeles, USA). The Intan software (Intan Interface 1.4.2, Intan Technologies, Los Angeles, USA) logged the signal from the electrodes. A windowed discrete Fourier transform converted the signal into the frequency domain, and the magnitude at the input frequency was extracted from each window. The most likely path was identified.

7.3.1.2 Experimental Procedure

We sutured two porcine aorta into a Y-shaped vessel tree and simulated a stenosis in the trunk with a cable tie. We embedded the vessel in a 20% gelatin solution and filled the vessel with 0.9% saline. The ground truth catheter position was recorded from fluoroscopic image series collected simultaneously with the voltage measurements. The catheter was advanced six times through the long path and three times through the short path.

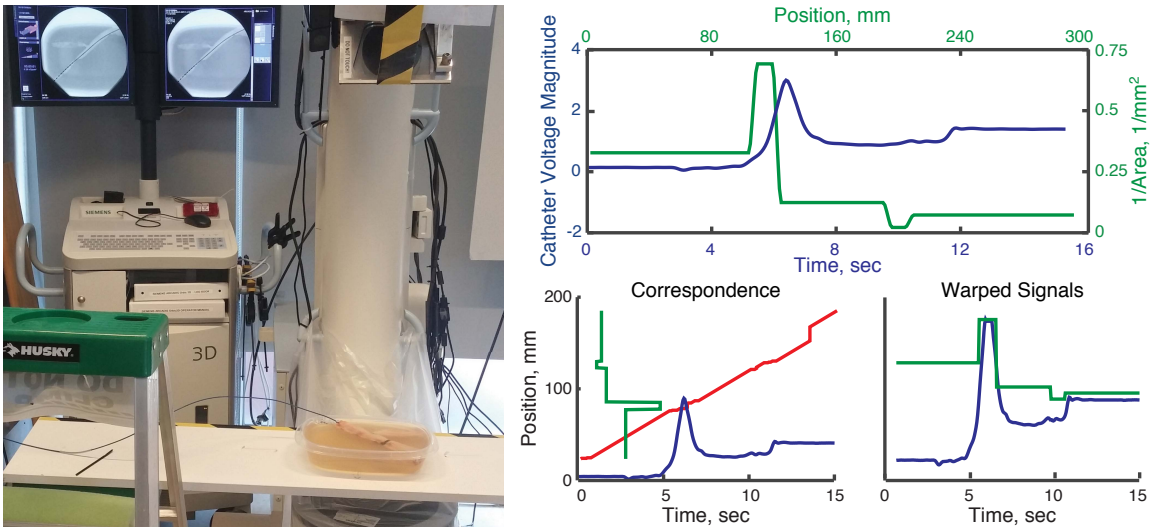

Figure 7.2: **Results in Y-Shaped Tissue Phantom.** Biological tissue experiment (left) and results from one trial in the long path (right). The stenosis and bifurcation are visible in both the inverse of the cross-sectional area and voltage magnitude.

7.3.1.3 Reference Signal Acquisition

A cone-beam CT of the specimen was obtained with a clinical c-arm (ARCADIS Orbic 3D, Siemens, Malvern, PA). The CT was processed and the vessels segmented, and the radii of the maximum inscribed sphere along the centerline were extracted using Vascular Modeling Toolkit (https://www.vmtk.org).

7.3.2 Results

The algorithm correctly identified the path 9/9 times with similarity measure 0.6081 ± 0.1614 (Fig 7.2).

7.4 *In Vivo* Matching Validation

The primary purpose of this experiment was to test if the catheter tracking system was capable of detecting vascular branches *in vivo*. We suspected that this would be challenging given the heterogeneity of whole blood, blood flow, and electrical noise associated with the operating room.

7.4.1 Methods

7.4.1.1 Signal Generation, Measurement, and Analysis

We used a 6F cardiac electrophysiology catheter (MutliCath 10J, Biotronik, Berlin, Germany). Its ten ring electrodes were 2 mm wide with 5 mm spacing. The input to the current source was ± 5 mV at 730 Hz, and the current source supplied a constant 18 μA to the emitting electrode. Due to a technical failure in the Intan system, a digital oscilloscope (PicoScope2203, Pico Technology, Cambridgeshire, United Kingdom) recorded the voltage from the catheter. Signals were analyzed as in the previous section.

7.4.1.2 Reference Signal Acquisition

A full body CT with angiography scan of the sedated animal was obtained using a clinical CT machine. The abdominal aorta neighboring the renal arteries was segmented using commercial software (VMTKLab 1.5.4, Orobix, Bergamo, Italy). Cus-

tom software computed the cross-sectional area along the centerlines of four paths of the segmented model. The set of inverse cross-sectional areas was the reference set for this experiment (Fig. 7.3a).

7.4.1.3 Surgical Procedure

This animal study was conducted at Klinikum Rechts der Isar in Munich, Germany in accordance with international guidelines. Animal care and use was performed by qualified individuals supervised by clinical veterinarians. A single female German Country pig (body weight 72 kg) was used for *in vivo* validation of bioelectric sensing.

The animal was sedated with an intramuscular injection of TKX at a dose of 1 cc/50 lb. After sedation, an intravenous catheter was placed in the animals ear vein and the animal was intubated to maintain an open airway. General anesthesia was maintained with isoflurane $(0.5 - 5.0\%)$ with oxygen supplementation, and the animal was mechanically ventilated for the duration of the imaging and experiment. The femoral artery was located, prepared, punctured and cannulated. An angiographic roadmap of the area of interest was obtained. The 6F bioelectric catheter was inserted through a sheath, the tip of which was positioned in the infrarenal abdominal aorta under fluoroscopic guidance. Bioelectric signals were collected simultaneously with fluoroscopic images as the catheter was manually advanced through the sheath into the suprarenal aorta, left superior renal artery, and left inferior renal artery at approximately $1-2$ mm/s. At the end of the experiment, sacrifice of the anesthetized

animal was carried out via anesthetic overdose.

7.4.2 Results

The BSN system behaved as expected and detected the renal artery ostia and several branches of the left renal artery (Fig. 7.3). While there was increased high frequency noise compared to previous experiments, it did not substantially affect the detection of branches. In fact, the matching algorithm successfully classified all trials in this experiment. The left renal artery was not mistaken for the right renal artery. The path with the lowest d Eqn. (6.1) was Path 3, whose second nearest neighbor was Path 2. It seems that the slight narrowing at the opening of the left renal artery was sufficient to distinguish it from the right renal artery.

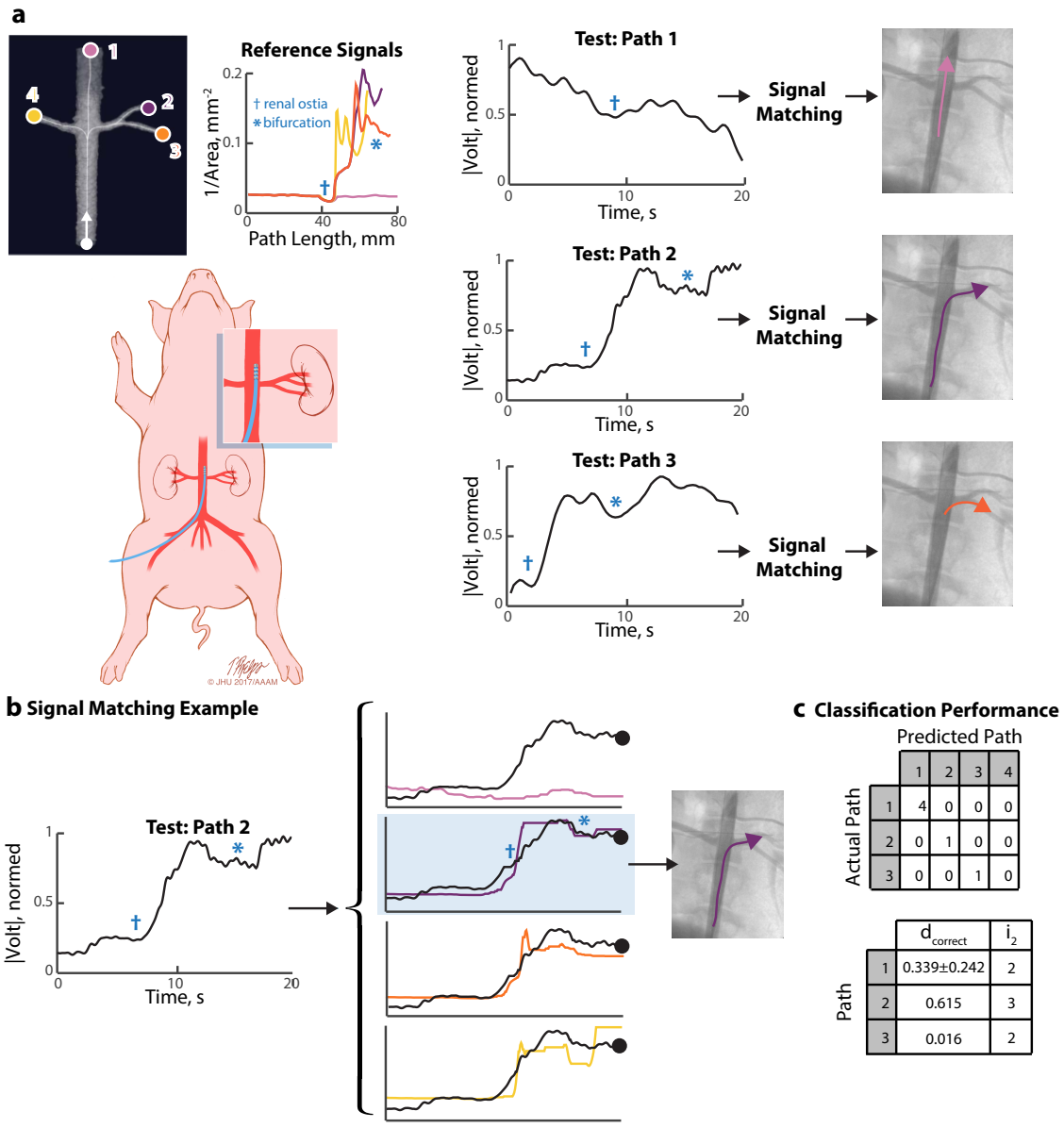

Figure 7.3: ***In vivo* renal artery navigation. a)** Before the surgical procedure, the segmented CTA was processed to extract the reference signals (inverse cross-sectional area). The catheter was not advanced down the right renal artery (yellow, Path 4), but it was included as a reference signal to test if the system could distinguish between the left and right renal arteries. **b)** OE-DTW takes in a test signal and set of reference signals. The test signal (from Path 2 in this case) is matched against warped versions of the reference signals, and the warping with the lowest cost is selected as the most likely classification. **c)** All trials were correctly classified.

7.5 Discussion

These initial *ex vivo* and *in vivo* experiments were instrumental in showing that the system detects branches in biological tissue. In particular, strong correspondence between the interventional voltage and the pre-interventional model geometry suggests that the interventional signal from the catheter is suitable for navigation *in vivo*. These results were promising, but the regions of interest were limited in these experiments in biological tissue. There were few reference signals, so the matching algorithm was restricted. Also, the signals have very few features. Combined, these two factors meant that the matching algorithm was highly sensitive to filtering, and only complete signals were analyzed. A rigorous *in vivo* study of bioelectric signals and their mapping to a pre-interventional model for a large region of interest is necessary before further development takes place.

Chapter 8

Bioelectric Sensing and Navigation Guidewire Development

8.1 Introduction

The state of the art for intravascular navigation is to first navigate a guidewire under fluoroscopy to the area of interest then advance a catheter over the guidewire (Fig. 8.1). Guidewires are used for navigation because they are smaller in diameter and more flexible, so there is less risk of puncturing a vessel or getting stuck in a small artery. The current BSN prototype uses a commercially available, non-irrigated 6F catheter, too large to be used as a guidewire. The goal of this project is to create a guidewire based on the BSN technology.

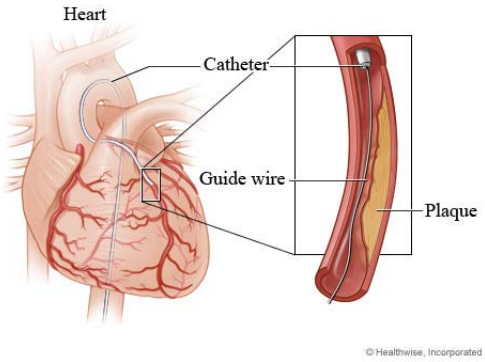

Figure 8.1: **Endovascular Navigation.** Catheters are advanced to a target by coaxial movements over a guidewire. In this illustration, the guidewire is inserted into the femoral artery, and advanced into the aortic arch. The catheter is pushed over the guidewire into the aortic arch. The surgeon uses the catheter to selectively stiffen the guidewire in order to navigate into the coronary artery. Then the guidewire crosses the lesion. Image from [113].

8.1.1 Relevance

While results with the catheter-based BSN system indicated that it is a promising technology to reduce the dependence on x-ray for catheter guidance, its clinical utility was limited by the fact that the prototype was a catheter rather than a guidewire. Our clinical collaborator specifically asked for a guidewire to test the navigation capabilities of BSN *in vivo*, and the success of this project was integral to the eventual adoption of the technology.

8.2 Preliminary Research

8.2.1 Clinical and Technical Literature

8.2.1.1 Clinical Guidewires

There are many types of guidewires for different applications, but the most common for navigation is the "workhorse". These wires generally are made of an inner core and inserted into an outer helical hollow strand (Fig. 8.2). The stiff inner core tapers distally and does not extend to the guidewire tip to reduce trauma to vessel walls. The standard diameter for a workhorse guidewire is 0.035" (0.889mm). The wire is usually made from ASTM 316L stainless steel, nitinol, or Platinum-Iridium. The three most important factors in choosing a wire are:

- Trackability: The wire must be able to follow the tip down a vessel, especially through tortuous vessels.
- Torquability: The ability to transfer a torque applied at the proximal end of the wire to the tip of the wire.
- Flexibility: The ability of the wire to flex on its longitudinal axis while maintaining torque and trackability.

Based on these factors, we used a commercially available 0.014" (0.356mm) guidewire as the core of my prototype. While more flexible than a 0.035" guidewire, it is be

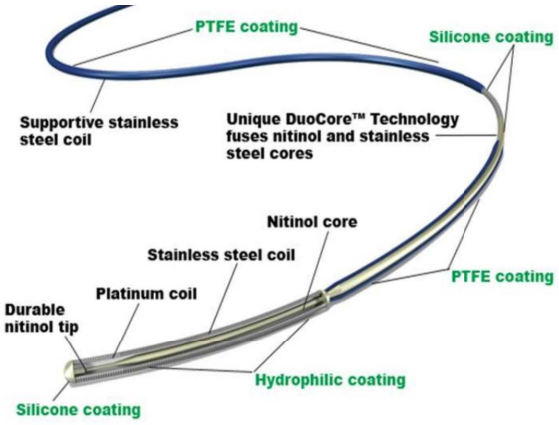

Figure 8.2: **Commercial Guidewire.** Schematic diagram of a commercially available workhorse guidewire (Runthrough NS, Terumo Interventional Systems, Somerset, New Jersey). From [114].

stiffened slightly by the electrical wires required for bioelectric signal acquisition. Furthermore, the core is guaranteed to be biocompatible.

8.2.1.2 Conductance Guidewire

While BSN is a new concept, one study of an impedance-monitoring guidewire has been published. The goal of this research was to validate a conductance guidewire's placement of a peripherally inserted central catheter (PICC) *in vivo* [115]. The key result was that important anatomical landmarks were accurately and repeatedly located solely with the conductance guidewire system. In benchtop and *in vivo* tests, the system measured large conductance step increases when the wire advanced in the correct direction. When the guidewire was advanced in the incorrect direction the conductance dropped. When incorrect advancement occurred, the wire was retracted to the previous location in which the conductance was the highest. The guidewire was

then advanced in the correct direction as evidenced by the step increases in conductance at each new location in the simulated anatomy. Once the simulated cavoatrial junction was identified, the wire was held stationary, and the PICC was advanced over the wire. When the PICC was placed, the conductance reading dropped almost to zero because of the small CSA of the PICC. Therefore, the authors' guidewire system enabled feedback during PICC placement, a procedure previously performed without guidance. Unfortunately, the authors gave no information about the guidewire's construction, materials, or electrode spacing.

While our guidewire could also be used for PICC placement, BSN has broad applicability because it incorporates a pre-interventional model. Because our software maps conductance to that vessel model, without knowing the landscape of the arteries along the path to an area of interest, the interventionalist will be given the location of the device in the vessel tree.

From the same team of researchers, Eqn. (5.2) from Chapter 5 and Figure 8.3 have been extremely useful to the design of the guidewire. The authors' model showed the best agreement with for a 0.889 mm catheter in a 3.8 mm (medium-sized) vessel. Therefore, we can expect accurate impedance measurements from our proposed 0.889 mm guidewire. The authors summarized their findings into three main points which we used as starting points for the guidewire design:

- The detection electrodes should be placed equidistant from the excitation electrodes.

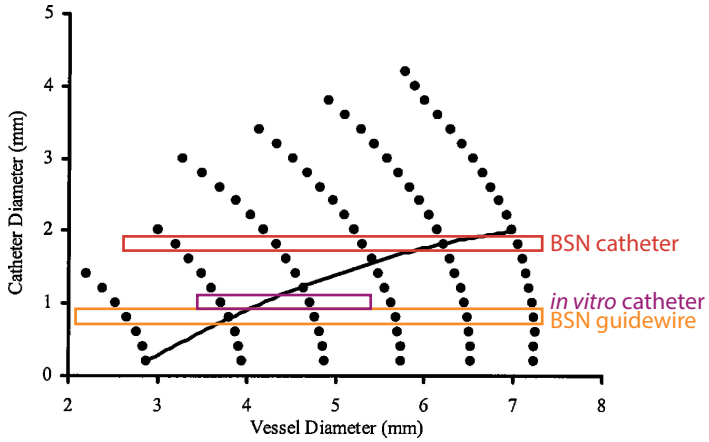

Figure 8.3: **Catheter-Vessel Diameter Relationship** The FEA was executed for a range of catheter and vessel diameters as shown by the six curves. The solid curve represents the optimized relationship between vessel and catheter diameter. We have highlighted the range of vessels we navigate with the BSN catheter (red) and the range we proposed to navigate with the guidewire (orange). From [105], modified with colored annotations.

- The distance between the current excitation electrodes should be much greater than the distance between the voltage detection electrodes.

- The distance between the detection and excitation electrodes should be comparable with the vessel diameter, or the diameter of the vessel should be small relative to the distance between the excitation electrodes.

8.2.2 Simulation

To test the performance of the guidewire under various electrode configurations, we simulated the voltage in a model of the vessel phantom. Extraction of a complete bioimpedance model requires the three-dimensional and multi-material solution of the generalized Poisson equation, assuming known permittivities of blood and tissue.

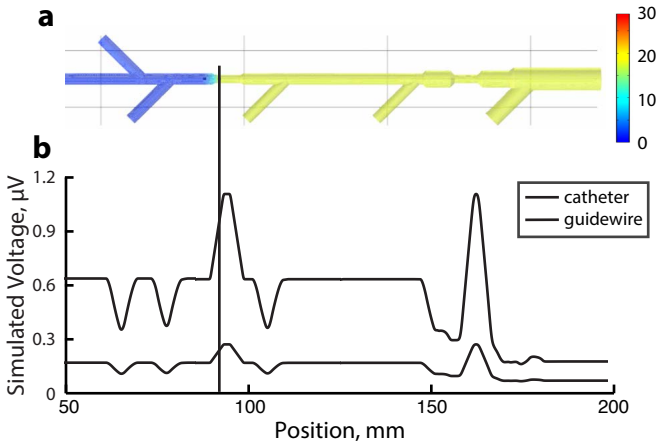

Figure 8.4: **a)** Simulation in rectilinear vessel phantom based on imported CAD geometry. The electrodes (black) span the first stenosis in this image. **b)** Voltage magnitude from simulation for the catheter (dashed line) and guidewire (solid line), measured at 1 mm increments.

Given a relatively simple geometry, one can use finite element analysis to numerically solve the generalized Poisson equation. For the first feasibility experiments, we designed an eight-path vessel phantom with two stenoses and one aneurysm. We imported the 3D CAD model into Comsol Multiphysics (COMSOL, Inc., Stockholm, Sweden) and simulated the signal as a two-electrode guidewire passed through the primary branch, measuring once every 1 mm. The simulation yielded a voltage profile for the path. As expected, the simulated voltage at the emitting electrode was inversely proportional to the CSA extracted from the CAD model (Figure 8.4), and the results matched the profile generated by a catheter in the same geometry.

8.3 Guidewire Development

8.3.1 Design Specifications

The guidewire must meet some general specifications for guidewires and the electrical needs of our specific application.

- Safety: biocompatible, atraumatic tip to avoid perforation and dissection
- Evidence: patents, literature, existing electrode-equipped vascular devices
- Electrode Surface Area: sufficient current transmission
- Durability: strong electrode/wire connection, corrosion-resistant
- Ease of Manufacture: prototype-able given my skills, available tools, off-the-shelf components
- Flexibility: able to withstand repeated bends in tortuous paths

Finally, we found an article presenting the construction of custom electromagnetic guidewires [70] and applied some of the design principles to my prototype. Those elements included a helical nitinol core and biocompatible heat shrink covering.

8.3.2 Design Selection

With these specifications in mind, we developed three design alternatives: Cylinder, Spring, and Braid (Fig. 8.5). Detailed drawings and Bills of Materials for each

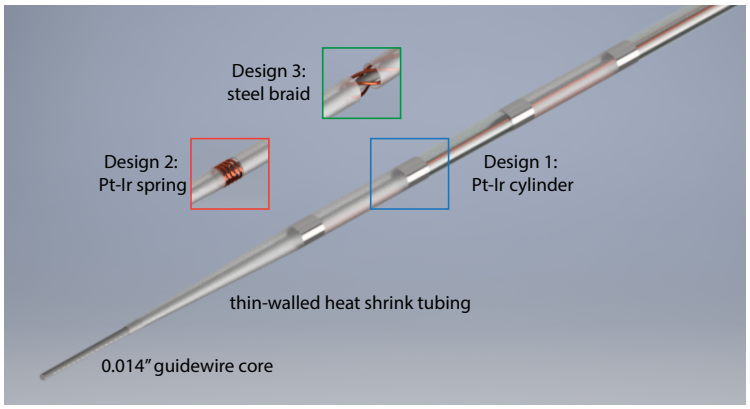

Figure 8.5: **Design Alternatives.** The three designs vary in the electrode design (inset).

can be found in Appendix A. We quantitatively evaluated each design (Table).

8.3.2.1 Design 1: Cylinder.

This guidewire is the closest to commercially available electrophysiology catheters. It has platinum-iridium cylinders soldered to stainless steel wires and threaded onto a commercial 0.014" guidwire core. It scored highest in evidence and electrode surface area. The most challenging part of this design is the manufacture of a prototype because the tiny (0.889 mm diameter) platinum cylinders might be difficult to solder to the wires.

8.3.2.2 Design 2: Spring.

This guidewire incorporates a Pt-Ir coil in place of the cylinder of Design 1. This design would be relatively easy to manufacture with Pt-Ir wire. However, it lacks durability because the wires may uncoil, and the electrode surface area is relatively

small compared to the cylinder.

8.3.2.3 Design 3: Braid.

This guidewire incorporates insulated stainless steel wires braided around the core. The insulation would be selectively removed from the wire, exposing the wire at intervals. This design is expected to be flexible, but we found no evidence to support this design, and the electrode surface area is the lowest of the three alternatives.

Table 8.1: Decision Analysis

		Cylinder		Spring		Braid	
Specification	Weight	Raw	Weighted	Raw	Weighted	Raw	Weighted
Safety	5	10	50	10	50	10	50
Evidence	5	10	50	7	35	3	15
Ease of Manufacture	4	5	20	8	32	6	24
Durability	4	8	32	4	16	3	12
Flexibility	3	5	15	7	21	7	21
Electrode Surface Area	5	10	50	6	30	3	15
Total			**217**		184		137

8.3.3 Prototype Construction

Based on my analysis, we chose Design 1: Cylinder as the embodiment design (Table 8.2). We first cut three 50 cm lengths of enameled copper wire. For each

wire, we sanded 3 cm of enamel from both ends. We threaded one end through a platinum electrode and soldered it to the exterior of the electrode. We soldered a lead to the other end. All three electrodes were threaded over the guidewire and applied a flew drops of silicone sealant between the electrodes to insulate them from each other and relieve some strain. Electrode spacing was adjustable but set to 7 mm. Finally, we manually braided the three strands of copper wire with the guidewire. Ideally, we would have covered the exposed wires in thin-walled heat shrink tubing as in [70], but we did not find a distributor with sufficiently small diameter tubing in stock. Furthermore, the 0.014" commercial guidewire core that we used has an extremely long atraumatic tip at 20 cm, so we threaded the electrodes onto the stiffer proximal end of guidewire. Therefore, this prototype is non-biocompatible and lacks an atraumatic tip, so it will only be used in the rectilinear phantom. The prototype meets the other design specifications (Fig. 8.6).

Table 8.2: Prototype Bill of Materials

Description	Manufacturer	Model	Quantity	Length	Part Number
0.014" guidewire	Abbott	Hi-Torque Traverse Guidewire	1	120 cm	22379H
enameled Cu wire	Conrad	0.15 mm Küpferlakdraht	3	50 cm	605196
Pt-Ir marker band	NuTec Medical	0.0315" OD × 0.0285" ID × 0.03937" long 90Pt/10Ir	3	1 mm	n/a
adhesive sealant	DAP	All-Purpose Silicone Adhesive Sealant	1	n/a	n/a

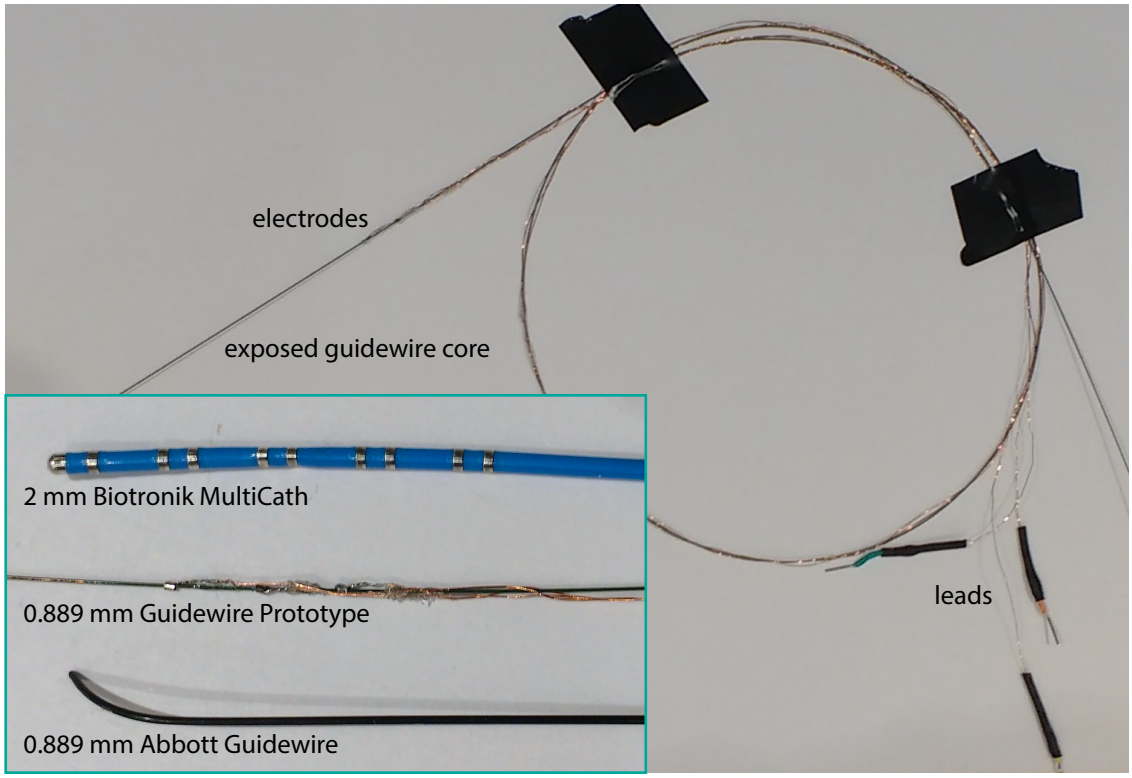

Figure 8.6: **Guidewire Prototype** The prototype guidewire was constructed around a 0.014" guidewire core. Its diameter matches that of a 0.035" workhorse guidewire (inset).

8.4 Experimental Validation

The objective of this experiment was to test if the prototype guidewire detects bifurcations, widenings, and stenoses as expected in the rectilinear phantom.

8.4.1 Experimental Setup

For comparison with the prototype guidewire, we used a 6F cardiac electrophysiology catheter (MutliCath 10J, Biotronik, Berlin, Germany). Its ten ring electrodes are 2mm wide with 5mm spacing. For the guidewire and the catheter, the input to the current source was ± 5 mV at 430 Hz, and the current source supplied a constant 18 μA to the emitting electrode on the catheter. A neighboring electrode is grounded. The signal between the two electrodes is amplified and filtered by a low-power biosignal acquisition system (RHD2000, Intan Technologies, Los Angeles, USA). The Intan software (Intan Interface 1.4.2, Intan Technologies, Los Angeles, USA) logs the AC voltage measurement from the electrodes and filters the signals. Finally, a sliding window discrete Fourier transform converts the signal into the frequency domain, and the magnitude at the input frequency is extracted for each window. We performed the first validation experiments in the rectilinear phantom immersed in 0.9% saline (Fig 8.7). A camera recorded the trajectories of the guidewire and the catheter as they were separately drawn through the six paths at $1 - 2$mm/s.

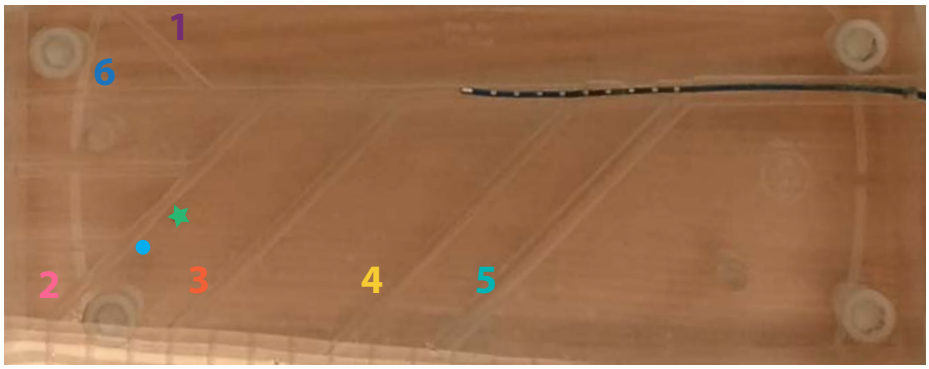

Figure 8.7: **Rectilinear phantom with labeled paths.** The two halves of the phantom were machined from acrylic and sealed with a thin layer of transparent waterproof grease. When assembled, it measures 10 cm × 25.4 cm × 5 cm. The paths are 2.5-10 mm diameter.

8.4.2 Results

The guidewire behaved as expected in the phantom, based on the literature and simulations. The catheter and the prototype guidewire had very similar performance in the phantom (Fig. 8.8). The guidewire even out-performed the catheter in the detection of a side branch, possibly because the guidewire's slightly smaller electrode spacing. These results suggest that this guidewire design could be pursued as an option for non-fluoroscopic guidewire navigation.

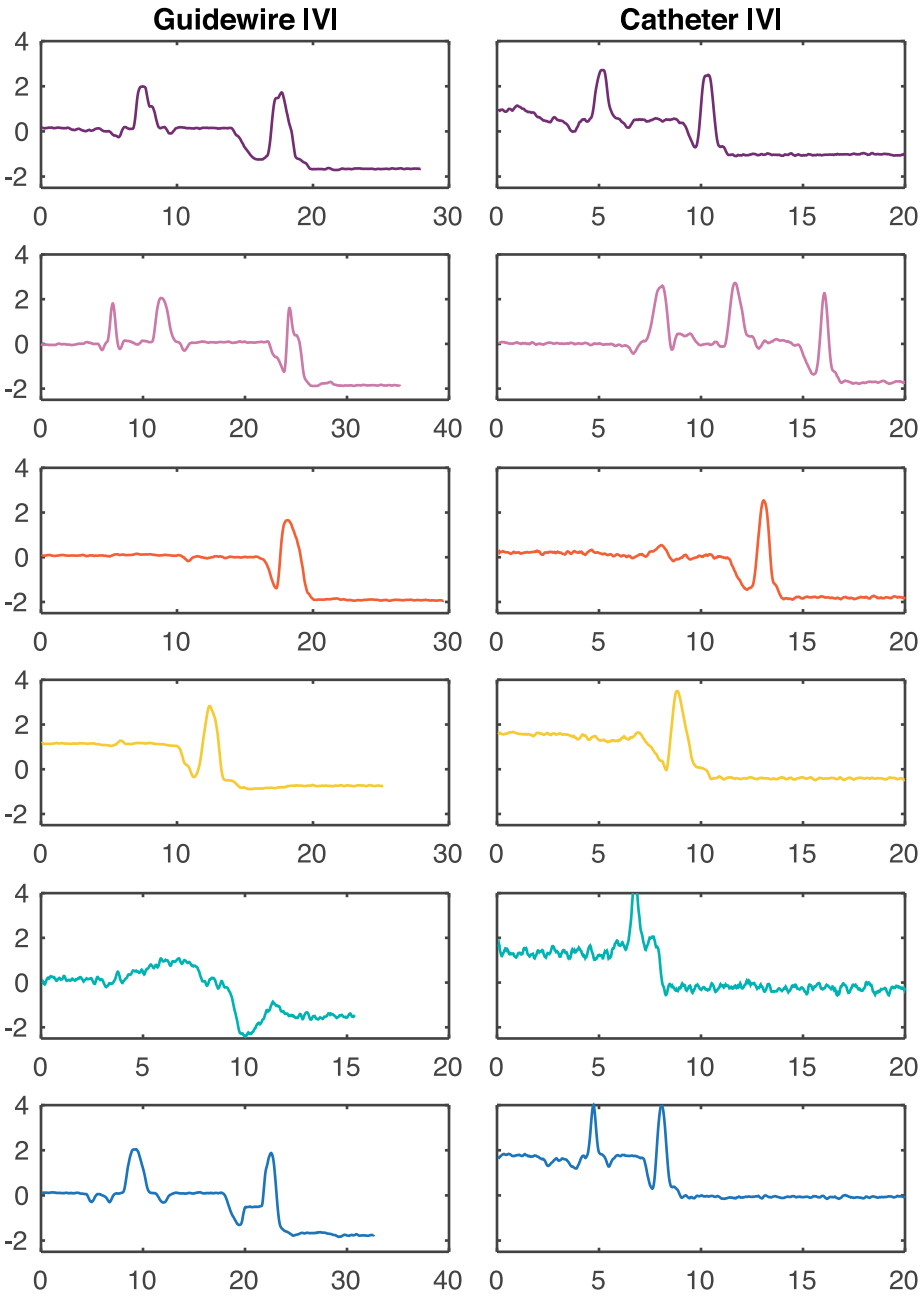

Figure 8.8: **Results.** Measured voltage from the guidewire (left) agrees with the catheter (right) in 6 paths of the phantom. Peaks (e.g. star) indicate that the device is at a stenosis and valleys (e.g. circle) indicate bifurcations, as confirmed by the video recordings. In Path 2, the guidewire detected a 2.5 mm diameter side branch (circle) not detected by the catheter.

Chapter 9

Bioelectric Sensing and Navigation Outlook

9.1 Next Steps

9.1.1 Guidewire Hardware and Testing

The next step in this project is to manufacture a biocompatible prototype. While infeasible to construct in-house, we have designed a slightly more complex prototype (Fig. 9.1). The design features distal and proximal sets of four electrodes arrayed around the guidewire with a ground ring electrode between the two sets. The arrays can operate together as ring electrodes to enable direction detection. Additionally, this configuration enables side-dependent bifurcation sensing to aid navigation. Be-

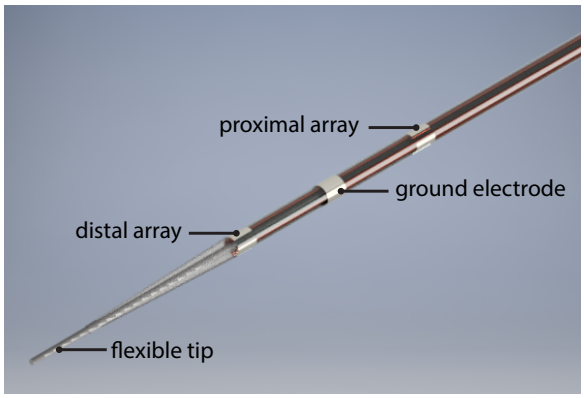

Figure 9.1: **Proposed Guidewire Design.** Electrode "arrays" consisting of four electrodes each are distributed around the guidewire core at two locations to measure side-dependent voltage changes.

cause the signal from a single electrode covers roughly a quadrant of the blood vessel, it does not necessarily sense cross-sectional area, so further simulations of the electric field behavior are necessary. However, in adding this feature to the prototype, we lend flexibility to further improve navigation. Given the immediate clinically applicability of the bioelectric guidewire, we would also perform mechanical testing for trackability and torqueability for this to ensure that it meets the ASTM guidelines. Similar tests are outlined in [70]. These tests are crucial to clinical acceptance, and not only because they are required by the Food and Drug Administration for 510(k) clearance. We aim for our guidewire to impart the same haptic feedback as a conventional guidewire, given haptic feedback's importance in clinical catheter navigation.

9.1.2 Mapping Algorithms

Bioelectric navigation depends on a software algorithm to match the bioelectric signal to the model from a pre-interventional image. To display the real-time position estimate, our next step is to compare techniques that match simulated and live data in real time (e.g. OE-DTW, Hidden Markov Models, random forests, particle filters, SLAM for graphs). A limitation of these matching algorithms is that they fail when the catheter changes direction (insertion vs retraction). One way we could address this is by attaching a simple encoder to the introducer sheath to detect the catheter's heading and prompting our software to only analyze data from when the catheter is being inserted. We will implement the best performing solution and integrate it into the surgical workflow.

Additionally, we see an interesting opportunity to apply fish-inspired multisensory integration to catheter localization. In our current implementation, the position of the catheter is estimated using the complete path and entire reference set at every time step independently; our navigation algorithm lacks "memory". We could incorporate memory such that it uses previous estimates to improve the current estimate. Inspired by the fish's sensory re-weighting, the weight given to previous estimates could be commensurate with the confidence of the previous measurements. For example, when a string of measurements has high confidence, the algorithm could upweight previous estimates in making its current estimate. That is, it could take into account that it is unlikely that the catheter would diverge to an unconnected branch. Modifying the

matching algorithm to include a saliency-weighted record of estimates could greatly reduce computation time, a major obstacle to clinical implementation.

9.1.3 Graphical User Interface

Next, building on our experience with image registration and image-guided surgical techniques, we will create a graphical user interface (GUI) to display most likely position of the guidewire in a digitally reconstructed radiograph (DRR), a simulated fluoroscopic image generated from the CT or MR image (Fig. 9.2). Throughout the development process, we will solicit critical feedback from our collaborator at Johns Hopkins School of Medicine, Dr. Clifford Weiss. A future user study will be used to further refine the user interface and assess the system's impact on the surgical workflow.

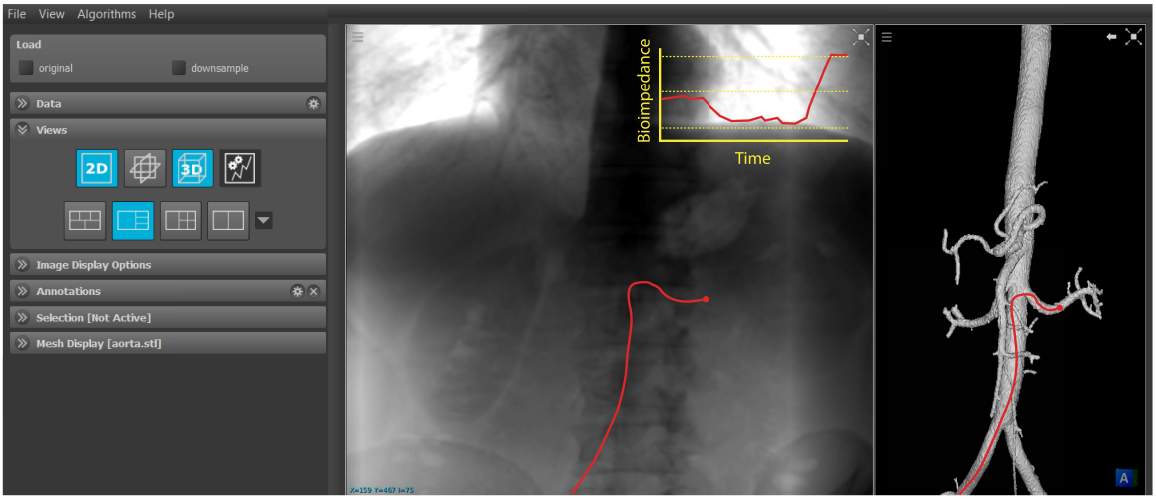

Figure 9.2: **User Interface Mock-Up**. *Left:* The interventionalist chooses desired views and their configuration. *Middle:* The DRR reconstructed from the 3D pre-interventional scan. The red trace is the most likely position of the guidewire as predicted by our system. In yellow, the bioimpedance signal indicates that the wire has just entered an area of relatively small diameter. *Right:* The guidewire's position in the 3D vessel tree extracted from the pre-interventional scan.

9.1.4 Pre-Clinical Animal Study

The real-time guidewire system must enable navigation to the area of interest with minimal fluoroscope use and without disruption to the clinical workflow. We will perform an *in vivo* experiment in porcine model, in which the catheter is advanced from a femoral insertion to the carotid arteries without fluoroscopy, relying entirely on bioelectric signals and their matching to a pre-interventional map. We suggest that this real-time "A to B" navigation be repeated with the guidewire. An Animal Care and Use proposal has been submitted at Johns Hopkins University for this experiment (Appendix B).

9.2 Possible Applications

We envision bioelectric sensing to be of primary benefit to catheter navigation. Furthermore, inspired by the way electromagnetic tracking and mapping systems have enabled cardiac radiofrequency ablation with greatly reduced fluoroscope use [71, 116–118], we feel that bioelectric sensing could be used to augment some specific procedures. For the most part, these examples do not require a pre-interventional image and instead present bioelectric sensing as additional feedback for a procedure.

9.2.1 Endovascular Aorta Repair

9.2.1.1 Clinical Motivation

An abdominal aortic aneurysm (AAA) is a localized enlargement of the abdominal aorta. Commonly located inferior to the renal arteries, an AAA requires emergency surgery because rupture of the aneurysm often results in death (Fig. 9.3).

Endovascular aorta repair (EVAR) is a minimally invasive treatment for AAA. I observed an EVAR procedure in 2015 at Helios Klinikum München West performed by Dr. Reza Ghotbi, Chief of Vascular Surgery. For this procedure, the surgeon first inserts large diameter introducer sheaths into both femoral arteries. Using fluroscopic images for feedback, guidewires are placed in the suprarenal aorta, superior to the aneurysm. The introducer catheter containing the main body of the graft is pushed along the guidewire. The surgeon partially deploys the main body of the graft,

checking on the fluoroscopic image that the renal arteries are not occluded (Fig. 9.4). If the renal artery ostia are occluded by the graft, renal function could be compromised. The main body of the graft is repositioned, to the extent possible. Next, a guidewire is navigated into the main body of the graft from the opposite femoral artery. The delivery catheter containing the contralateral limb of the graft is inserted over the wire and into the main body of the graft. Dr. Ghotbi mentioned it would be catastrophic to deploy the short limb of the graft outside the main body of the graft, so for this stage, surgeons rely extensively on high-dose (2D) angiographic images for placement. Finally, a balloon catheter is inserted and inflated to tack hooks into the vessel way at proximal edge, joints, and distal edge of the graft. This procedure smooths out folds and helps to prevent Type 1 leaks. Dr. Ghotbi prefers not to use a balloon especially in fragile vessels but he cannot be sure of the configuration of the graft from images alone. The procedure I observed lasted 122 minutes.

EVAR is a major fluoroscopic intervention, with fluoroscopy used to localize the lesion, monitor the procedure, and control and document the end result. Even neglecting the dose due to angiographic imaging used in diagnosis of AAA and planning of EVAR, patient EVAR radiation dose in one study was 13.4 ± 8.6 mSv, [52]. Significantly higher dose was reported in patients with a high body mass index [55], those with complex anatomy [56], and those undergoing fenestrated procedures [57]. The risk of radiation to surgeons, staff, and trainees during EVAR is also significant. In a study of vascular surgeons, those who regularly perform EVAR were shown to have

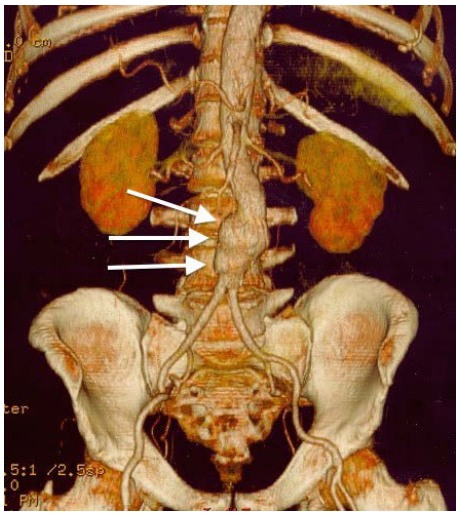

Figure 9.3: **Abdominal Aortic Aneurysm.** CT reconstruction of a patient with AAA (arrows), image from Bakerstmd / CC-BY-SA-4.0.

the highest radiation exposure to body, eye, and hand [119].

The major acute complications of EVAR are renal artery obstruction, vascular perforations caused by the very stiff guidewires used to support the large delivery catheters, and inability to cannulate the contralateral gate which can lead to iliac rupture or dissection. Finally, contrast-induced nephropathy due to the high volume of contrast injected is a constant medical concern with fluoroscopy-intensive procedures like EVAR. Commonly, 50-100 mL of dye is injected during the procedure [121], and contrast-induced nephropathy resulting in acute renal failure occurs in 6.7% of cases, according to one national survey [122].

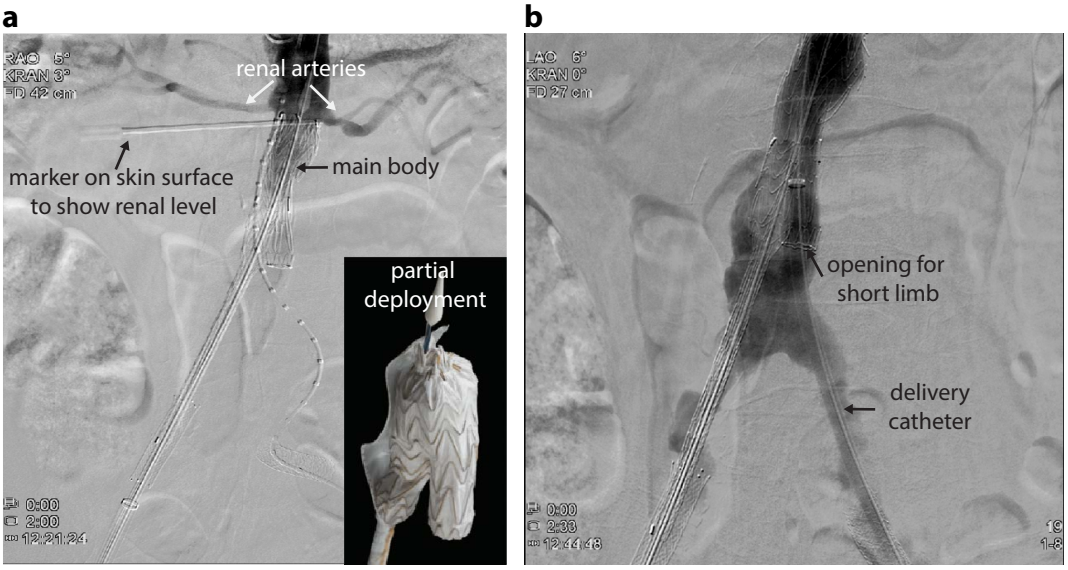

Figure 9.4: **Endovascular Aorta Repair.** EVAR observed at Helios Klinikum München West (Pasing) performed by Dr. Reza Ghotbi. **a)** Deployed main body of the graft, carefully avoiding occlusion of the renal ostia. Inset: schematic of a partially deployed main body, image from [120]. **b)** Positioning the delivery catheter containing the contralateral limb of the graft.

9.2.1.2 Proposed Implementation

Once incorporated into the clinical workflow, there are three specific areas where we feel bioelectric sensing could improve this procedure, in addition to navigation from the femoral artery to the area of interest. First, incorporating a bioimpedance sensor into the tip of the main body's delivery catheter would help to ensure that the renal ostia are not occluded before the stent is deployed. Currently, angiographic imaging is of limited use to the positioning of the device because the operator must study the graft markers and arterial anatomy simultaneously. In contrast, when the bioelectric catheter passes a bifurcation, the electric impedance changes dramatically. Similarly, bioelectric sensing and navigation could provide feedback to the surgeon

when the stiff guidewire for the contralateral limb is being inserted into contralateral gate. Again, the signal would be dramatically different depending on the catheter's position, either inside the large lumen of the stent or in the small space between the stent and the vessel wall. Finally, a BSN catheter could be used to ensure that the graft is fully deployed, since the final desired geometry of the graft lumen is known before the procedure. Passing through the full length of the graft, the catheter could detect unobstructed visceral ostia as well as any anomalous folds in the graft material. The smaller diameter bioelectric guidewire could be navigated into the side branches to check their connection to the main branch. The surgeon could employ the balloon catheter as described above, but only if a fold is detected.

Bioelectric Sensing and Navigation's inside-out sensing could change the current practice for graft deployment by providing real-time feedback about stent positioning from inside the stent itself. Furthermore, the reduced reliance on angiography could reduce the instance of contrast-induced nephropathy by keeping contrast injection to a safe level.

9.2.2 Umbilical Catheterization

9.2.2.1 Clinical Motivation

Umbilical catheterization is the easiest way to catheterize an infant. It is usually performed without guidance. These lines can be placed by physicians, nurses, and

paramedics. There are two arteries and one vein in the umbilicus. For both arterial and venous catheterization, the primary concern is perforation leading to internal hemorrhage, and it is difficult to detect based only on haptic feedback. The most common complication is the creation of a false luminal tract by cannulation of the layer between the vascular intima and the muscle. [123].

Catheterization of the umbilical artery is the standard of care for arterial access in neonates. It is employed for blood sampling, angiography, blood pressure monitoring, and blood gas monitoring. The catheter size is 3.5F-5F, depending on the weight of the infant. The recommended placement is superior to the renal, superior mesenteric and celiac arteries. Catheters are commonly misplaced in the femoral or gluteal arteries. Insertion depth is estimated by the following formula: insertion depth (cm) = 3× birth weight (kg) + 9 [124]. This method was found to be 57% accurate in predicting correct insertion depth [125]. Once advanced to the predetermined depth, placement is confirmed with chest and abdominal radiography (Fig. 9.5).

Umbilical vein catheterization is performed for blood, intraveneous fluid, and drug delivery during emergency resuscitation. The catheter size is 5F-8F, depending on the weight of the infant. Generally, catheters are placed in the inferior vena cava below the right atrium. To estimate insertion depth, the shoulder-to-umbilicus length is used. Again, placement is confirmed with a chest and abdominal radiograph. Complications specific to venous catheterization include hepatic abscess or nectrosis due to misplacement in the portal vein, arrhythmia, and pericardial tamponade [126].

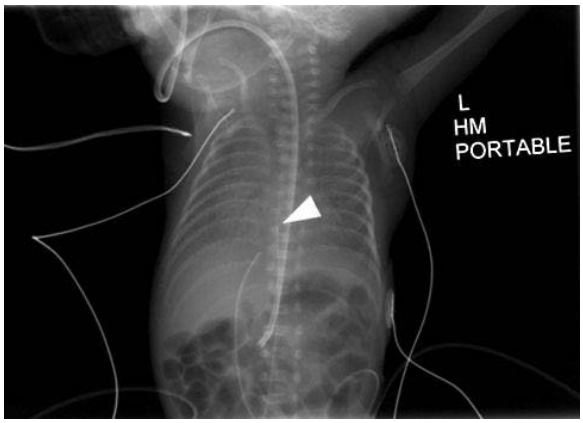

Figure 9.5: **Umbilical Artery Catheterization.** Radiograph of correctly positioned umbilical artery catheter with tip at T8-9, image from [124].

9.2.2.2 Proposed Implementation

Umbilical catheterization is often performed in an emergency setting without image guidance. Bioelectric sensing could lend critical feedback to this procedure, making it much safer to perform. For instance, when an arterial umbilical catheter is correctly placed, the vessel cross-sectional areas monotonically increase from the umbilical artery, through the iliac artery, and up into the aorta. If incorrectly placed in the gluteal or femoral artery, there will be a sharp decrease in cross-sectional area. Similarly, during venous placement, the cross-sectional area would decrease dramatically if the catheter were to enter the portal vein rather than continuing up the vena cava.

Guidewires are not typically used during this procedure, but a flexible bioelectric guidewire with two electrodes could be threaded through the single-channel catheter and advanced with the catheter during placement. We envision that the voltage

signal between the two electrodes would be displayed to the clinician along with the expected signals. To make the analysis more intuitive, we would most likely display the inverse of the voltage from the catheter and the expected cross-sectional areas along the path to the area of interest, which should be proportional. No changes to the clinical workflow would be necessary, except that the clinician would have access to the visual display and would be able to quickly recognize a misplacement.

Furthermore, bioelectric sensing would detect the creation of a false luminal tract. First, the false luminal tract would be much smaller diameter than vessel lumen, causing an obvious decrease in the inverse voltage signal that lasts as long as the catheter is in the false lumen. Also, in the frequency range used by our system, the conductivity of blood is more than twice that of muscle and vessel wall [98]. Therefore, there will be a sudden and temporary voltage increase as the vessel wall is perforated. The clinician currently relies on haptic feedback, detecting perforations with a "popping" sensation. Bioelectric sensing could augment the haptic feedback by disambiguating expected resistance felt due to tortuous vessels and resistance preceding a perforation.

9.2.3 Tumor Ablation Monitoring

9.2.3.1 Clinical Motivation

Unresectable tumors are usually treated with percutaneous ablation and embolization treatments (Fig. 9.6). In ablation procedures, a thin, needle-like probe is inserted directly into a tumor under ultrasound or fluorscopic guidance. In radiofrequency ablation, a high frequency current is passed through the tip of the probe, heating the tumor to the point of cell death. In microwave thermotherapy/thermoablation, microwaves transmitted through the probe heat and destroy the tumor cells. In cryoablation/cryotherapy, very cold gasses are passed through the probe, freezing the tumor cells. Ablation procedures are usually monitored with intraoperative ultrasound and evaluated with post-operative CT. Often, some surrounding tissue is damaged.

Embolization may be performed alone or alongside ablation. In arterial embolization procedures, a catheter is inserted into the hepatic artery under fluoroscopic guidance. Small particles are injected through the catheter into the artery, forming a blockage that starves the tumor of oxygen and nutrients. Additionally, in chemoembolization, either the particles contain chemotherapy drugs or chemotherapy drugs are injected directly into the blood vessel feeding the tumor. In radioembolization, the particles carry a radioactive isotope that delivers radiation to the tumor for several days. In all types of embolization, success is evaluated from a post-operative CT/MR image taken at a follow-up visit. Embolization carries a higher risk of damaging

healthy tissue, for instance, if a large branch of the hepatic artery is embolized.

9.2.3.2 Proposed Implementation

Our proposed technology is an add-on to existing treatments. Multiple catheters equipped with at least two electrodes are positioned within the volume of a tumor to be treated. Each catheter creates a weak electric field in its near surroundings at a unique frequency. Combining the measurements from each catheter results in an impedance map of the tumor volume. During treatment, the catheters monitor changes to the tissue caused by the treatment and display the changes to the interventionalist. Specifically, changes to relative water content, cell packing density, and several other factors affect the impedance.

The impedance change mediated by tissue death could be displayed as a single impedance trace per catheter or a color-coded map of the impedance around each catheter, with color indicating the catheter and intensity indicating the impedance. The traces or map would be displayed directly on the ultrasound (ablation) or angiogram (embolization) to facilitate monitoring of tumor tissue health and repositioning of treatment delivery devices, if necessary (Fig. 9.7). Additionally, an algorithm could use the tumor health distribution as determined by the impedence map to optimal redeploy the catheters.

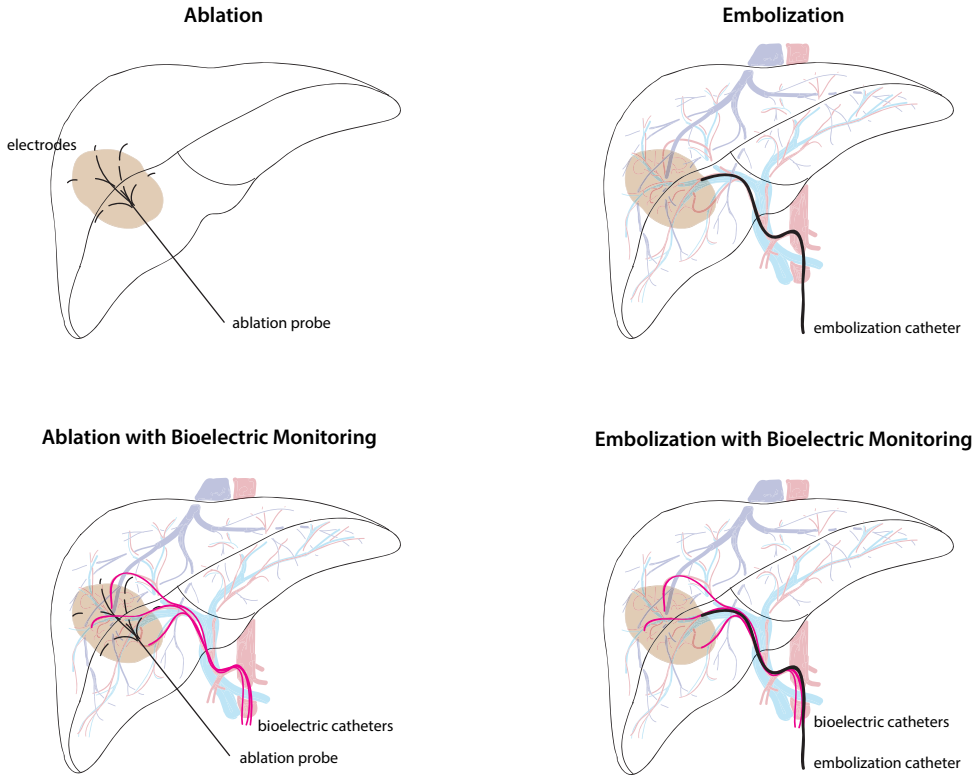

Figure 9.6: **Ablation and Embolization**. The top figures illustrate the two most common state-of-the-art local treatments for hepatocellular carcinoma. The bottom figures show how impedance-based monitoring augments those procedures. In both techniques, one or more bioimpedance catheters (pink) are inserted through the hepatic artery and into the tumor volume. Each catheter is equipped with electrodes to send and receive electric signals. In particular, each catheter outputs a unique signal and measures the impedance, which indicates tissue health. In this manner, we can provide the interventionalist with real-time feedback about the progress of the embolization procedure.

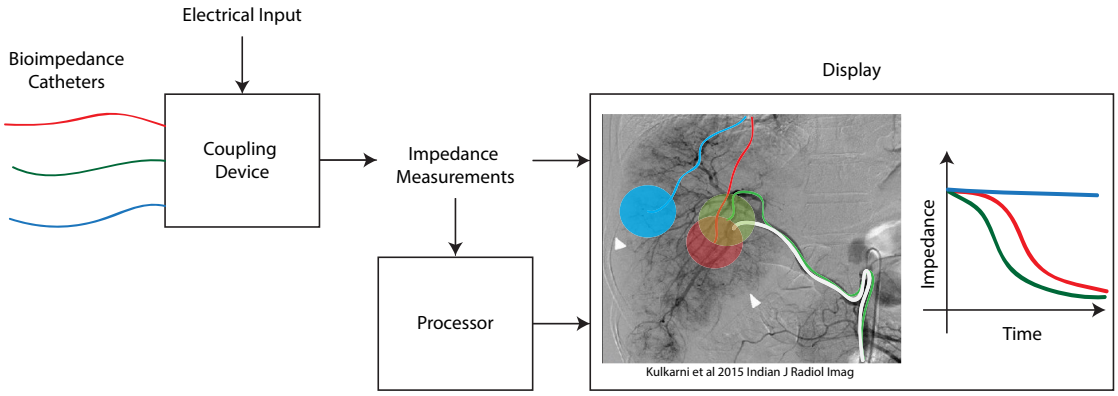

Figure 9.7: **Tumor Ablation Conceptual Schematic.** Electrical input signals create distinct electric fields around each catheter. The coupling device records the impedance from each catheter and sends those signals to the display and the processor. The processor creates an image overlay, highlighting the catheters and electric fields on the angiographic image. In the image, the white catheter has embolized a branch of the right hepatic artery. The red, blue, and green catheters measure tumor health. The green and red catheter signals indicate cell death, but the volume covered by the blue catheter is not adequately embolized. The display shows both the map of the impedance superimposed on the interventional angiographic image and the time series since the beginning of treatment.

9.3 Discussion

The generation and measurement of bioelectrical signals within vessels and their mapping to a patient-specific vessel model has never been proposed for catheter navigation. BSN circumvents many clinical imaging challenges such as catheter detection, motion compensation, and catheter tracking. As such, it holds several important advantages over the existing catheter navigation techniques. Its primary benefit would be a reduction in radiation exposure for the patient, interventionalist and staff. Furthermore, it does not substantially change the clinical workflow, since we will design it to be compatible with commercially available catheters. The relative ordering and amplitude of the features (e.g. bifurcations, stenoses) used for matching the live signal to the pre-interventional reference signals is unchanged under deformation, so the system remains unaffected by movement and manipulation of the surrounding tissue and does not require 2D/3D deformable registration. The system determines the position of the endovascular device *relative to surrounding anatomy*, so our proposed technology has the highest accuracy in the feature-rich environments most challenging to navigation and most relevant to an interventionalist. The ability to integrate 3D imaging obtained prior to the procedure with real-time endovascular sensing offers the potential for case planning, improved efficiency for achieving difficult destinations, and precision for endovascular device deployment.

Once incorporated into the clinical workflow, Bioelectric Navigation has the potential to significantly reduce fluoroscope use during common endovascular proce-

dures. Its impact need not be restricted to procedures currently performed under fluoroscopy. It could ease the positioning of complex grafts, for instance a graft to repair abdominal aortic aneurysm. These custom grafts incorporate holes such that the the visceral arterial ostia are not occluded. Angiographic imaging is of limited use to the positioning of the device because the operator must study the graft markers and arterial anatomy simultaneously. In contrast, when the bioelectric catheter passes a bifurcation, the electric impedance changes dramatically. Bioelectric Navigation's inside-out sensing could change the current practice for device deployment by providing continuous, real-time feedback about device positioning from inside the device itself.

Chapter 10

Conclusion

This dissertation demonstrated the mutual benefit of interdisciplinary research between biology and engineering. Part I focused primarily on the application of control theoretic analysis to understanding how animals alter their sensory integration to respond to environmental change. With their highly interconnected sensory modalities, animals show extraordinary behavioral robustness in unpredictable environments. The inherent challenge to uncovering the neural control mechanisms of multisensory integration lies in the presentation of independent sensory inputs. In our novel augmented reality apparatus, the weakly electric fish *Eigenmannia virescens* swam to maintain position in a translucent refuge which moved to a prescribed trajectory. The experiments were performed in the dark, so the moving refuge was invisible to the fish's vision, and electrosense dominated the fish's response to that stimulus. Gray stripes were projected onto the refuge in a prescribed trajectory independent

of the physical refuge trajectory and served as the visual cue of refuge position. By examining the relationship between the reference trajectories and the fish's motion at two water conductivities and two input amplitudes, we evaluated the linearity of multisensory integration, the change in relative perceptual weights of vision and electrosense, and the effect of the magnitude of sensory conflict. We found evidence of multisensory enhancement, indicating that the fish uses visual and electrosensory feedback to resolve sensory conflict and maintain position in the moving refuge. The tracking behavior obeyed superposition at both input amplitudes, suggesting linear sensorimotor integration. The fish increased the perceptual weight to vision when electrosensory salience was degraded. Interestingly, we saw no substantial effect of stimulus amplitude in our experiment. Robustly interpreting sensory input is crucial to an animal's successful interaction with the environment, and we found that weakly electric fish employ a flexible, saliency-based locomotor control.

Part II of this dissertation outlined the development of a novel navigation system for endovascular devices: bioelectric sensing and navigation. Inspired by the electrosense of weakly electric fish, our technique is founded on the acquisition of endovascular electrical measurements and their correlation with reference signals extracted from standard diagnostic imaging. First, I reviewed the technical and clinical literature motivating the research. Next, I documented the simulations, benchtop, *ex vivo* tissue, and *in vivo* animal experiments validating the use of bioelectric signals in navigation. The results suggest that our system is capable of providing intraopera-

tive feedback to clinicians about the location of the catheter relative to bifurcations, stenoses, and aneurysms. Critically, the evidence outlined in these chapters provides the foundation for future pre-clinical trials. The generation and measurement of bioelectrical signals within vessels and their mapping to a patient-specific vessel model has never been proposed for catheter navigation. If successfully adopted into clinical use, this new technology will significantly reduce the dependence on fluoroscopy and, in turn, patient and interventionalist radiation dose.

In conclusion, our inherently interdisciplinary research contributes to a growing body of literature that supports the use of engineering to probe difficult questions in neuroscience. By applying system identification, we discovered some of the tools used by the nervous system of intact, freely behaving animals. Conversely, as engineered systems become more complex, the need for efficient signal integration becomes ever more important. On our interdisciplinary team, it was natural to look to biology for inspiration. In our case, simply adding a sensor to a catheter would provide only limited benefit. To have real clinical impact, we combine the sensor's measurement with a geometric model, creating a technology with the potential to improve the safety and efficacy of many common endovascular procedures.

Appendix A

Guidewire Design

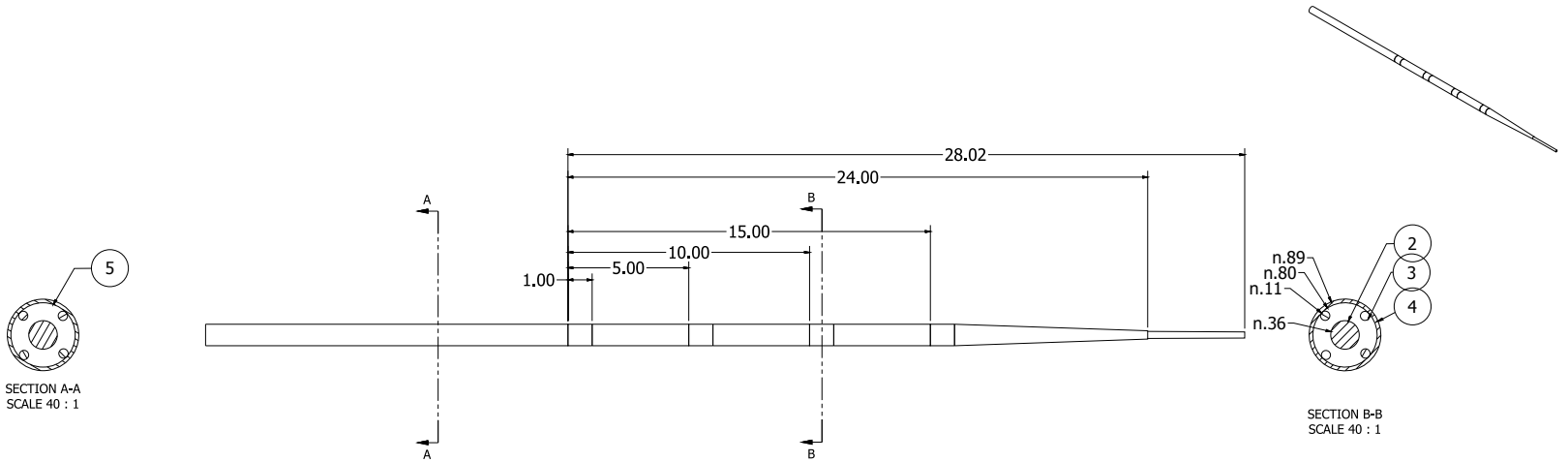

PARTS LIST			
ITEM	QTY	PART NUMBER	MATERIAL
1	4	copper_wire	Copper, enameled
2	1	commercial_wire	Stainless Steel, Austenitic
3	4	copper_exposed	Copper, Alloy
4	4	electrode	90Pt-10Ir
5	1	tubing_long	Polyethylene, High Density
6	2	tubing_med	Polyethylene, High Density
7	1	tubing_short	Polyethylene, High Density
8	1	tubing_tap	Polyethylene, High Density

DRAWN Erin Sutton	3/13/2017	
CHECKED		
QA		TITLE: Alternative 1: Cylinder
MFG		
APPROVED		SIZE D / DWG NO guidewire_4 / REV
		SCALE 12 : 1 / SHEET 1 OF 1

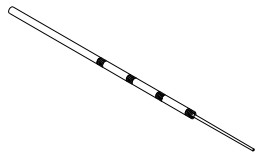

SECTION A-A
SCALE 40 : 1

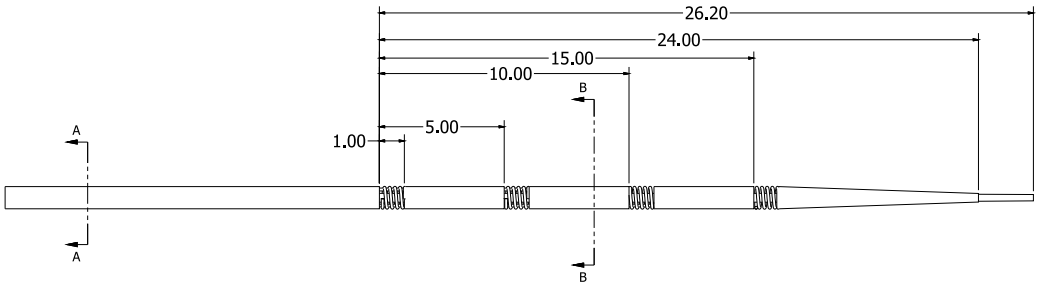

SECTION B-B
SCALE 40 : 1

PARTS LIST			
ITEM	QTY	PART NUMBER	MATERIAL
1	4	copper_wire	Copper, enameled
2	1	commercial_wire	Stainless Steel, Austenitic
3	1	tubing_long	Polyethylene, High Density
4	2	tubing_med	Polyethylene, High Density
5	1	tubing_short	Polyethylene, High Density
6	1	tubing_tap	Polyethylene, High Density
7	4	spring	90Pt-10Ir

DRAWN Erin Sutton	3/13/2017	
CHECKED		
QA		TITLE: Alternative 2: Spring
MFG		
APPROVED		SIZE: D; DWG NO: guidewire_spring; REV:
		SCALE: 12 : 1; SHEET 1 OF 1

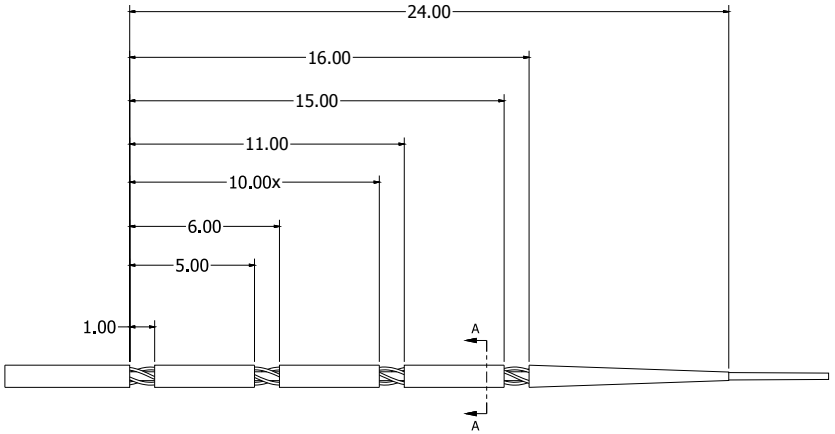

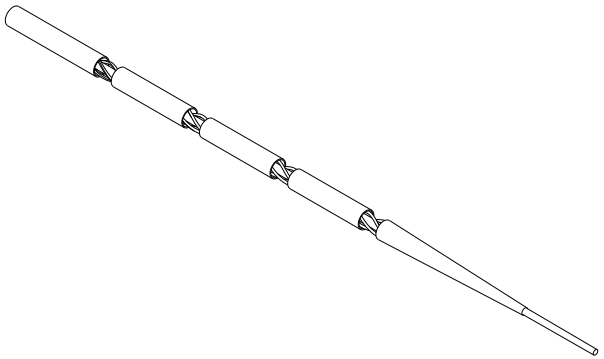

SECTION A-A
SCALE 40 : 1

PARTS LIST			
ITEM	QTY	PART NUMBER	MATERIAL
1	1	braid	Copper, enameled
2	1	commercial_wire	Stainless Steel, Austenitic
3	1	tubing_long	Polyethylene, High Density
4	2	tubing_med	Polyethylene, High Density
5	1	tubing_short	Polyethylene, High Density
6	1	tubing_tap	Polyethylene, High Density

DRAWN	Erin Sutton	3/16/2017
CHECKED		
QA		
MFG		
APPROVED		

TITLE: Alternative 3: Braid

SIZE: D | DWG NO: guidewire_braid | REV:

SCALE: 12 : 1 | SHEET 1 OF 1

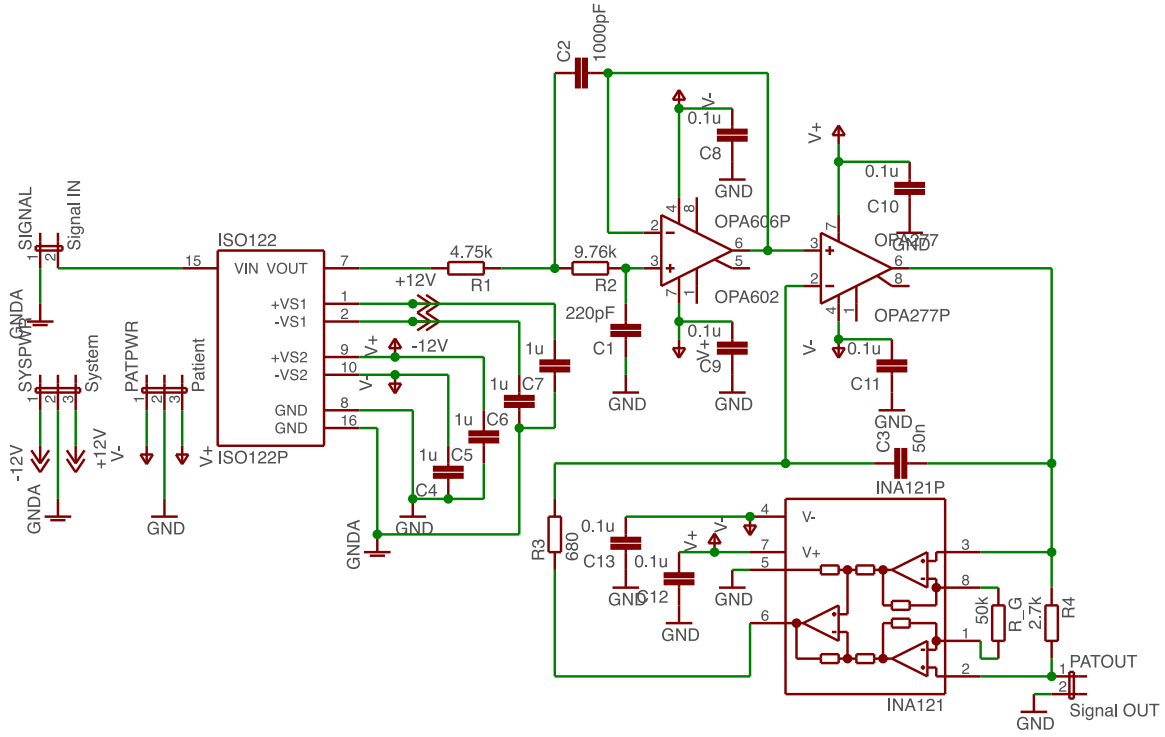
SIGNAL
Signal IN
GNDA
SYSPWR
System
PATPWR
Patient
-12V
+12V
V-
V+
GNDA
GND
ISO122
VIN VOUT
+VS1
-VS1
+VS2
-VS2
GND
GND
ISO122P
4.75k
R1
9.76k
R2
+12V
-12V
1u
C7
1u
C6
1u
C5
1u
C4
GNDA
GND
C2
1000pF
0.1u
C8
GND
OPA606P
OPA602
220pF
C1
0.1u
C9
GND
V+
V-
0.1u
C10
OPA277P
0.1u
C11
GND
C3
50n
INA121P
R3
680
0.1u
C13
GND
0.1u
C12
GND
V-
V+
INA121
50k
R_G
2.7k
R4
PATOUT
Signal OUT
GND

Appendix B

Live Animal Surgical Plan

APPENDIX B. LIVE ANIMAL SURGICAL PLAN

A Description of Procedures

All animal housing and procedures will be performed at the Johns Hopkins University Medical Center in the facilities of Research Animal Resources (RAR). Three domestic swine (*sus scrofa domestica*) of either sex will be housed in the RAR facilities. For both experiments, the animal will undergo one day of imaging, rest for approximately one week, then one of the minimally invasive procedure will be conducted. On the imaging day, full-body soft tissue CTA and MRA scans will be acquired in in the RAR radiology suite. While the animal rests for a week, we will segment the CTA and MRA images to extract a 3D model of the vasculature. The centerlines of the vessels in that model become reference signals for our sensing system. We propose two distinct surgical procedures: Bioelectric Sensing, and Bioelectric Navigation.

A.1 Bioelectric Sensing

This experiment requires one animal. In the operating room, the animal will be anesthetized and ventilated, and femoral access will be obtained by a cutdown of the femoral artery. The artery will be cannulated with a 6F sheath. Our guidewire will be inserted into the sheath and a 4-5F catheter regularly used in human angiography will be advanced over the guidewire to mechanically support it. During the procedure, we will take continuous fluoroscopy and bioimpedance recordings while our clinical collaborator oversees the advancement of the guidewire by a linear actuator at a constant speed from the femoral artery into the aortic arch, providing torque as necessary to steer the wire. If needed for navigation, contrast material (300-330 mg/mL iodine) will be injected through the catheter. After the procedure, we will compare the bioimpedance signal to the surrounding geometry ground truth from the CTA and fluoroscopic image series. We expect that the guidewire will detect all major branching arteries (brachiocephalic, left subclavian, celiac, cranial mesenteric, renal, caudal mesenteric, contralateral external iliac, and internal iliac trunk).

A.2 Bioelectric Navigation

This experiment requires two animals. The user will perform *in vivo* navigation using only our navigation GUI from femoral access to carotid arteries, blind to fluoroscopic images acquired simultaneously with the bioimpedance signal. In the operating room, the animal will be anesthetized and ventilated, and femoral access will be obtained by a cutdown of the femoral artery. The artery will be cannulated with a 6F sheath. Our guidewire will be inserted into the sheath and a 4-5F catheter regularly used in human angiography will be advanced over the guidewire to mechanically support it. When the carotid artery is cannulated, the user will take a fluoroscopic image with contrast (300-330 mg/mL idoine) as a final ground truth image to measure accuracy (carotid artery placement, inserted past the proximal electrode). In the same animal, we will repeat navigation with fluoroscopic guidance available to surgeon. We will compare time to goal and placement accuracy for the bioimpedance-only and fluoroscopy-only conditions.

B Justifications

Domestic swine was selected based on the similarities between human and porcine anatomy and physiology, especially the cardiovascular anatomy. Domestic swine have been shown to be especially useful in the testing of novel endovascular devices, and our research team has performed many previous studies in this model system. These *in vivo* procedures are only a part of our research plan, which also includes simulation, synthetic, gelatin, and *ex vivo* validation. However, they are crucial to investigate the safety and effectiveness of our novel device, because the electrical environment inside a live animal is more complicated than simulations and benchtop phantoms can replicate. For instance, we have a peristaltic pump to approximate bloodflow through our phantoms, but it lacks surrounding tissues like organs and fat deposits that might influence the electric field of our guidewire.

C Minimization of Pain and Distress

All animals will be premedicated by an intramuscular injection of atropine (0.05 mg/kg), midazolam (0.1 mg/kg), and ketamine (20 mg/kg). General anesthesia will be induced 15 min after premedication by an intravenous injection of thiopental (5 mg/kg), and maintained with mechanical ventilation and a mixture of ethrane (1.5$\pm$2%) and oxygen (1.5L/min). At the end of both experiments, sacrifice of the anesthetized animal will be carried out in accordance with the AVMA guidelines. If, after the imaging study or during the surgical procedure, an animal contracts a severe infection, undergoes respiratory distress, or fails to eat, it will be humanely euthanized.

Appendix C

Guidewire Simulation

COMSOL MULTIPHYSICS®

Guidewire in Rectilinear Phantom

Author

Erin Sutton

Report date

Mar 10, 2015 11:40:57 AM

APPENDIX C. GUIDEWIRE SIMULATION

Contents

1 Global Definitions

1.1 Parameters 1

Parameters

Name	Expression	Value	Description
posGND	10.0	10	
posIN	15	15	
posPROBE	15	15	

2 Component 1 (comp1)

2.1 Definitions

2.1.1 Probes

Domain Point Probe 1

Probe type	Domain point probe

2.1.2 Selections

inelec

Selection type
Explicit

Selection
Boundaries 25–28

gndelec

Selection type
Explicit

Selection
Boundaries 19–22

electrodes

Selection type
Explicit

Selection
Boundaries 19–22, 25–28

Cylinder 8

Selection type
Object_selection

Selection
Points 81–82, 91–96, 101–102

2.1.3 Coordinate Systems

Boundary System 1

Coordinate system type	Boundary system
Tag	sys1

2.2 Geometry 1

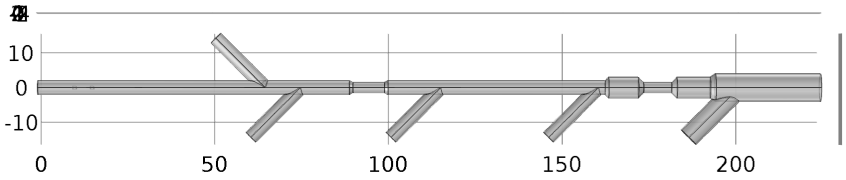

Geometry 1

Units

Length unit	mm
Angular unit	deg

2.3 Materials

2.3.1 Titanium beta-21S

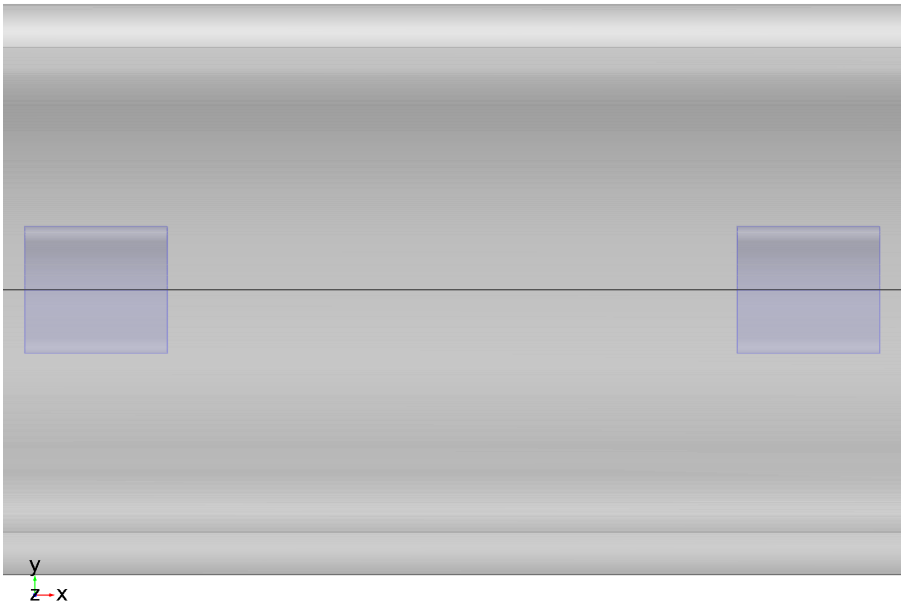

Titanium beta-21S

Selection

Geometric entity level	Domain
Selection	Domains 6–7

5

2.3.2 Blood

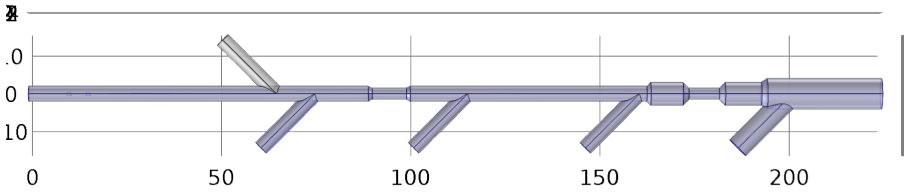

Blood

Selection

Geometric entity level	Domain
Selection	Domains 3, 15–16, 20, 25, 30, 35, 38, 45, 50, 55, 60, 65, 70, 75, 80, 85, 90

2.3.3 VesselWall

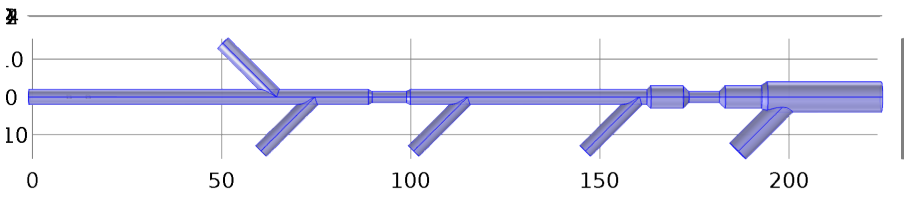

VesselWall

Selection

Geometric entity level	Domain
Selection	Domains 1–2, 4–5, 8–14, 17–19, 21–24, 26–29, 31–34, 36–37, 39–44, 46–49, 51–54, 56–59, 61–64, 66–69, 71–74, 76–79, 81–84, 86–89, 91–92

2.4 Electric Currents (ec)

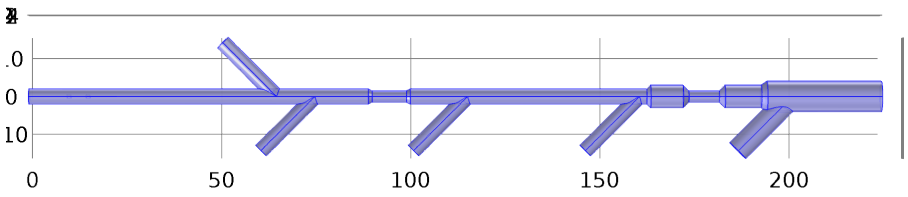

Electric Currents

Features

Current Conservation 1
Electric Insulation 1
Initial Values 1
Ground 1
Boundary Current Source 1

2.5 Mesh 1

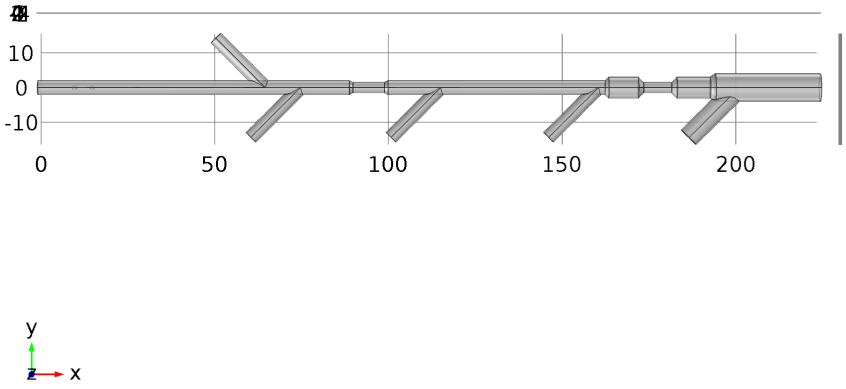

Mesh 1

3 Study 1

Computation information

Computation time	2 h 42 min 25 s
CPU	Intel(R) Core(TM) i7-3540M CPU @ 3.00GHz, 2 cores
Operating system	Windows 7

3.1 Parametric Sweep

Parameter name	Parameter value list
posGND	range(20,2,200)
posIN	range(25,2,205)
posPROBE	range(25,2,205)

3.2 Stationary

Study settings

Description	Value
Include geometric nonlinearity	Off

Physics and variables selection

Physics interface	Discretization
Electric Currents (ec)	physics

Mesh selection

Geometry	Mesh
Geometry 1 (geom1)	mesh1

4 Results

4.1 Data Sets

4.1.1 Data Set 1

4.1.2 Data Set 1

4.1.3 Data Set 1

4.1.4 Data Set 1

4.2 Derived Values

4.2.1 Derived Values 1

4.3 Tables

4.3.1 Probe Table 1

Probe Table 1

posGND	posIN	posPROBE	Electric potential (V), Point Probe Expression 1
20.000	25.000	25.000	1.6284E-5
22.000	27.000	27.000	1.6236E-5
24.000	29.000	29.000	1.6218E-5
26.000	31.000	31.000	1.6212E-5
28.000	33.000	33.000	1.6207E-5
30.000	35.000	35.000	1.6229E-5
32.000	37.000	37.000	1.6231E-5
34.000	39.000	39.000	1.6276E-5
36.000	41.000	41.000	1.6254E-5

posGND	posIN	posPROBE	Electric potential (V), Point Probe Expression 1
38.000	43.000	43.000	1.6241E-5
40.000	45.000	45.000	1.6234E-5
42.000	47.000	47.000	1.6264E-5
44.000	49.000	49.000	1.6232E-5
46.000	51.000	51.000	1.6227E-5
48.000	53.000	53.000	1.6212E-5
50.000	55.000	55.000	1.6199E-5
52.000	57.000	57.000	1.6173E-5
54.000	59.000	59.000	1.6215E-5
56.000	61.000	61.000	1.6108E-5
58.000	63.000	63.000	1.5649E-5
60.000	65.000	65.000	1.5046E-5
62.000	67.000	67.000	1.5536E-5
64.000	69.000	69.000	1.6130E-5
66.000	71.000	71.000	1.6188E-5
68.000	73.000	73.000	1.5416E-5
70.000	75.000	75.000	1.4555E-5
72.000	77.000	77.000	1.5220E-5
74.000	79.000	79.000	1.6094E-5
76.000	81.000	81.000	1.6258E-5
78.000	83.000	83.000	1.6226E-5
80.000	85.000	85.000	1.6237E-5
82.000	87.000	87.000	1.6207E-5
84.000	89.000	89.000	1.6919E-5
86.000	91.000	91.000	1.9823E-5
88.000	93.000	93.000	2.4341E-5
90.000	95.000	95.000	2.5572E-5
92.000	97.000	97.000	2.5515E-5
94.000	99.000	99.000	2.6144E-5
96.000	101.00	101.00	2.2176E-5
98.000	103.00	103.00	1.7626E-5
100.00	105.00	105.00	1.6255E-5

posGND	posIN	posPROBE	Electric potential (V), Point Probe Expression 1
102.00	107.00	107.00	1.6253E-5
104.00	109.00	109.00	1.6234E-5
106.00	111.00	111.00	1.6185E-5
108.00	113.00	113.00	1.5441E-5
110.00	115.00	115.00	1.4751E-5
112.00	117.00	117.00	1.5289E-5
114.00	119.00	119.00	1.6127E-5
116.00	121.00	121.00	1.6221E-5
118.00	123.00	123.00	1.6211E-5
120.00	125.00	125.00	1.6212E-5
122.00	127.00	127.00	1.6264E-5
124.00	129.00	129.00	1.6204E-5
126.00	131.00	131.00	1.6211E-5
128.00	133.00	133.00	1.6162E-5
130.00	135.00	135.00	1.6205E-5
132.00	137.00	137.00	1.6220E-5
134.00	139.00	139.00	1.6206E-5
136.00	141.00	141.00	1.6251E-5
138.00	143.00	143.00	1.6183E-5
140.00	145.00	145.00	1.6255E-5
142.00	147.00	147.00	1.6215E-5
144.00	149.00	149.00	1.6215E-5
146.00	151.00	151.00	1.6219E-5
148.00	153.00	153.00	1.6201E-5
150.00	155.00	155.00	1.6138E-5
152.00	157.00	157.00	1.5870E-5
154.00	159.00	159.00	1.4915E-5
156.00	161.00	161.00	1.4718E-5
158.00	163.00	163.00	1.5040E-5
160.00	165.00	165.00	1.2816E-5
162.00	167.00	167.00	1.0794E-5
164.00	169.00	169.00	1.0457E-5

posGND	posIN	posPROBE	Electric potential (V), Point Probe Expression 1
166.00	171.00	171.00	1.0797E-5
168.00	173.00	173.00	1.3674E-5
170.00	175.00	175.00	2.0676E-5
172.00	177.00	177.00	2.5219E-5
174.00	179.00	179.00	2.5254E-5
176.00	181.00	181.00	2.6031E-5
178.00	183.00	183.00	2.0673E-5
180.00	185.00	185.00	1.3371E-5
182.00	187.00	187.00	1.0601E-5
184.00	189.00	189.00	1.0337E-5
186.00	191.00	191.00	1.0324E-5
188.00	193.00	193.00	1.0378E-5
190.00	195.00	195.00	9.4936E-6
192.00	197.00	197.00	8.7831E-6
194.00	199.00	199.00	8.5753E-6
196.00	201.00	201.00	8.6278E-6
198.00	203.00	203.00	8.6715E-6
200.00	205.00	205.00	8.7528E-6

4.4 Plot Groups

4.4.1 Electric Potential (ec)

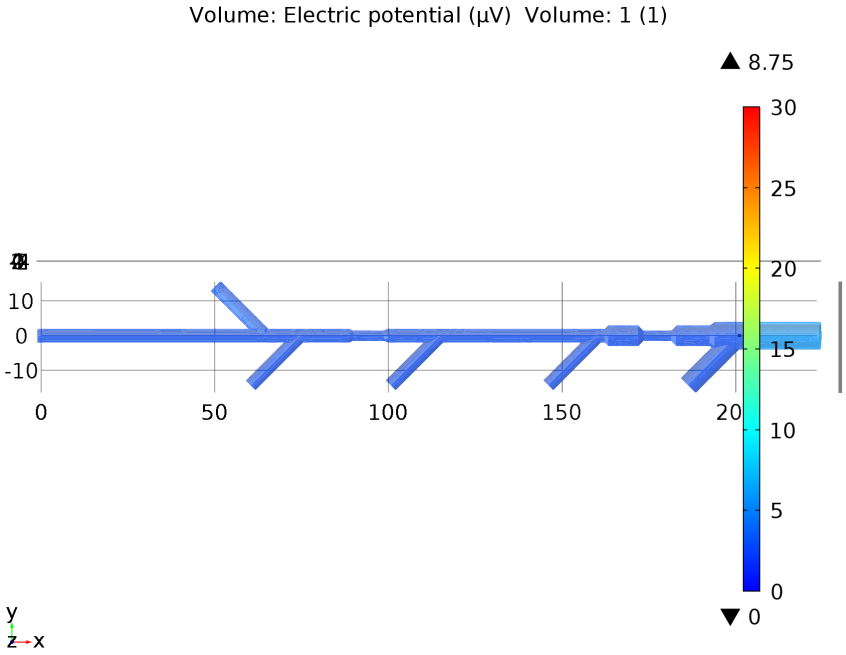

Volume: Electric potential (μV) Volume: 1 (1)

4.4.2 Probe 1D Plot Group 5

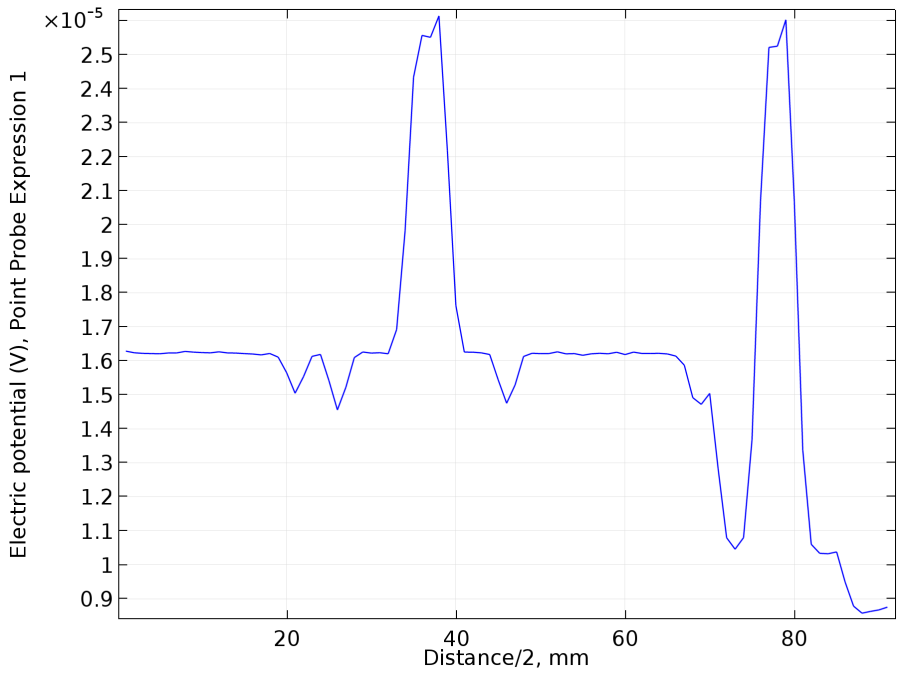

Bibliography

[1] N. J. Cowan, M. M. Ankarali, J. P. Dyhr, M. S. Madhav, E. Roth, S. Sefati, S. Sponberg, S. A. Stamper, E. S. Fortune, and T. L. Daniel, "Feedback control as a framework for understanding tradeoffs in biology," *Integr Comp Biol*, vol. 54, no. 2, pp. 223–237, 2014.

[2] E. Roth, S. Sponberg, and N. J. Cowan, "A comparative approach to closed-loop computation," *Curr Opin Neurobiol*, vol. 25, pp. 54–62, 2014.

[3] W. Heiligenberg, "Electrolocation of objects in the electric fish *eigenmannia* (rhamphichthyidae, gymnotoidei)," *J Comp Physiol*, vol. 87, no. 2, pp. 137–164, 1973.

[4] M. Gaudry, J.-M. Bartoli, L. Bal, R. Giorgi, M. D. Masi, P.-E. Magnan, and P. Piquet, "Anatomical and technical factors influence the rate of in-stent restenosis following carotid artery stenting for the treatment of post-carotid endarterectomy stenosis," *PLoS ONE*, vol. 11, no. 9, p. e0161716, 2016.

[5] E. Moscarella, A. Ielasi, B. Cortese, and A. Varricchio, "Coronary in-stent

restenosis: Where are we now?" *Ann VAsc Med Res*, vol. 3, no. 2, pp. 1033–1037, 2016.

[6] S. W. Cheng, *Rutherford's Vascular Surgery*, 8th ed. Philadelphia: Elsevier Saunders, 2014.

[7] D. Niel, H. Schone, F. Scapini, and A. Miyan, "Optokinetic responses, visual adaptation and multisensory control of eye movements in the spiny lobster, *Palinurus vulgaris*," *J Exp Biol*, vol. 107, pp. 349–366, 1983.

[8] J. M. Gardiner, J. Atema, R. E. Hueter, and P. J. Motta, "Multisensory integration and behavioral plasticity in sharks from different ecological niches," *PLoS One*, vol. 9, pp. 2875–2884, April 2014.

[9] M. A. Frye, M. Tarsitano, and M. Dickinson, "Odor localization requires visual feedback during free flight in *Drosophilia melanogaster*," *J Exp Biol*, vol. 206, pp. 843–855, 2003.

[10] D. Chow and M. Frye, "Context dependent olfactory enhanced optomotor flight control in *Drosophila*," *J Exp Biol*, vol. 211, pp. 2478–2485, 2008.

[11] M. A. Frye and M. H. Dickinson, "Motor output reflects the linear superposition of visual and olfactory inputs in *Drosophila*," *J Exp Biol*, vol. 207, no. 1, pp. 123–131, Jan. 2004.

[12] M. A. MacIver, N. M. Sharabash, and M. E. Nelson, "Prey-capture behavior

in gymnotid electric fish: Motion analysis and effects of water conductivity," *J Exp Biol*, vol. 204, no. 3, pp. 543–557, 2001.

[13] M. E. Nelson, M. A. MacIver, and S. Coombs, "Modeling electrosensory and mechanosensory images during the predatory behavior of weakly electric fish," *Brain Behav and Evol*, vol. 59, no. 4, pp. 199–210, 2002.

[14] S. A. Stamper, E. Roth, N. J. Cowan, and E. S. Fortune, "Active sensing via movement shapes spatiotemporal patterns of sensory feedback," *J Exp Biol*, vol. 215, no. 9, pp. 1567–1574, 2012.

[15] J. Bastian, "Vision and electroreception: Integration of sensory information in the optic tectum of the weakly electric fish *Apteronotus albifrons*," *J Comp Physiol A*, vol. 147, no. 3, pp. 287–297, 1982.

[16] G. J. Rose and J. G. Canfield, "Longitudinal tracking responses of the weakly electric fish, *Sternopygus*," *J Comp Physiol A*, vol. 171, no. 6, pp. 791–798, 1993.

[17] ——, "Longitudinal tracking responses of *Eigenmannia* and *Sternopygus*," *J Comp Physiol A*, vol. 173, pp. 698–700, 1993.

[18] P. Moller, "Multimodal sensory integration in weakly electric fish: a behavioral account," *J Physiol Paris*, vol. 96, no. 5-6, pp. 547–56, 2002.

[19] E. E. Sutton, A. Demir, S. A. Stamper, E. S. Fortune, and N. J. Cowan,

"Dynamic modulation of visual and electrosensory gains for locomotor control," *J R Soc Interface*, vol. 13, no. 118, p. 20160057, May 2016. [Online]. Available: https://dx.doi.org/10.1098/rsif.2016.0057

[20] E. E. Sutton, S. A. Stamper, A. Demir, T. R. Mitchell, E. S. Fortune, and N. J. Cowan, "Multisensory control of locomotion in weakly electric fish," in *Society for Integrative and Comparative Biology*, Austin, TX, USA, January 2014.

[21] E. E. Sutton, S. A. Stamper, A. Demir, E. S. Fortune, and N. J. Cowan, "Measuring multisensory integration in weakly electric fish," in *Society for Integrative and Comparative Biology Mid-Atlantic Regional Meeting*, Newark, NJ, USA, November 2015.

[22] S. Sponberg, J. P. Dyhr, R. W. Hall, and T. L. Daniel, "Luminance-dependent visual processing enables moth flight in low light," *Science*, vol. 348, no. 6240, pp. 1245–1248, June 2015.

[23] S. P. Windsor, R. J. Bomphrey, and G. K. Taylor, "Vision-based flight control in the hawkmoth *Hyles lineata*," *J R Soc Interface*, vol. 11, p. 20130921, 2014.

[24] M. J. Elzinga, W. B. Dickson, and M. H. Dickinson, "The influence of sensory delay on the yaw dynamics of a flapping insect," *J R Soc Interface*, vol. 9, pp. 1685–1696, 2012.

BIBLIOGRAPHY

[25] T. Beatus, J. M. Guckenheimer, and I. Cohen, "Controlling roll perturbations in fruit flies," *J R Soc Interface*, vol. 12, p. 20150075, 2015.

[26] N. Rohrseitz and S. N. Fry, "Behavioral system identification of visual flight speed control in *Drosophila melanogaster*," *J R Soc Interface*, vol. 8, pp. 171–185, 2011.

[27] E. Roth, R. W. Hall, T. L. Daniel, and S. Sponberg, "The integration of parallel mechanosensory and visual pathways resolved through sensory conflict," *Proc Nat Acad Sci*, vol. 113, no. 45, pp. 12 832–12 837, Oct 2016.

[28] K. S. Oie, T. Kiemel, and J. J. Jeka, "Multisensory fusion: simultaneous reweighting of vision and touch for the control of human posture," *Cog Brain Res*, vol. 14, no. 1, pp. 164–176, Jun. 2002.

[29] T. Kiemel, Y. Zhang, and J. J. Jeka, "Identification of neural feedback for upright stance in humans: stabilization rather than sway minimization," *J Neurosci*, vol. 31, no. 42, pp. 15 144–15 153, 2011.

[30] E. Roth, K. Zhuang, S. A. Stamper, E. S. Fortune, and N. J. Cowan, "Stimulus predictability mediates a switch in locomotor smooth pursuit performance for *Eigenmannia virescens*." *J Exp Biol*, vol. 214, no. 7, pp. 1170–1180, 2011.

[31] M. S. Madhav, S. A. Stamper, E. S. Fortune, and N. J. Cowan, "Closed-loop

stabilization of the jamming avoidance response reveals its locally unstable and globally nonlinear dynamics," *J Exp Biol*, vol. 216, no. 22, pp. 4272–4284, 2013.

[32] N. J. Cowan and E. S. Fortune, "The critical role of locomotion mechanics in decoding sensory systems," *J Neurosci*, vol. 27, no. 5, pp. 1123–1128, 2007.

[33] S. Sefati, I. D. Neveln, E. Roth, T. Mitchell, J. B. Snyder, M. A. MacIver, E. S. Fortune, and N. J. Cowan, "Mutually opposing forces during locomotion can eliminate the tradeoff between maneuverability and stability," *Proc Nat Acad Sci*, vol. 110, no. 47, pp. 18 798–18 803, 2013.

[34] R. Ruiz-Torres, O. M. Curet, G. V. Lauder, and M. M. MacIver, "Kinematics of the ribbon fin in hovering and swimming of the electric ghost knifefish," *J Exp Biol*, vol. 216, pp. 823–834, 2013.

[35] A. Hitschfeld, S. Stamper, K. Vonderschen, E. Fortune, and M. Chacron, "Effects of restraint and immobilization on electrosensory behaviors of weakly electric fish," *ILAR J.*, vol. 50, no. 4, pp. 361–372, 2009.

[36] B. E. Stein and T. R. Stanford, "Multisensory integration: current issues from the perspective of the single neuron," *Nature Reviews Neuroscience*, vol. 9, pp. 255–266, 2008.

[37] R. Pintelon and J. Schoukens, *System Identification: A Frequency Domain Approach*, 2nd ed. Hoboken, New Jersey: Wiley, 2012.

[38] C. Cuppini, M. Ursino, E. Magosso, B. A. Rowland, and B. E. Stein, "An emergent model of multisensory integration in superior colliculus neurons," *Front Integr Neurosci*, vol. 6, p. 6, 2010.

[39] D. Raposo, J. P. Sheppard, P. R. Schrater, and A. K. Churchland, "Multisensory decision-making in rats and humans," *J Neurosci*, vol. 32, no. 11, pp. 3726–3735, March 2012.

[40] P. W. Battaglia, R. A. Jacobs, and R. N. Aslin, "Bayesian integration of visual and auditory signals for spatial localization," *J Opt Soc Am A*, vol. 20, no. 7, pp. 1391–1397, July 2003.

[41] R. B. Welch and D. H. Warren, "Immediate perceptual response to intersensory discrepancy," *Psychol Bull*, vol. 88, no. 3, pp. 638–667, 1980.

[42] J. Heron, D. Whitaker, and P. McGraw, "Sensory uncertainty governs the extent of audio-visual interaction," *Vis Res*, vol. 44, pp. 2875–2884, 2004.

[43] M. Simoneau, N. Teasdale, C. Bourdin, C. Bard, M. Fleury, and V. Nougier, "Aging and postural control: postural perturbations caused by changing the visual anchor," *J Am Geriatr Soc*, vol. 17, no. 2, pp. 235–240, Feb 1999.

[44] S. M. O'Connor and J. M. Donelan, "Fast visual prediction and slow optimization of preferred walking speed," *J Neurophysiol*, vol. 107, no. 9, pp. 2549–2559, 2012.

[45] R. E. Kalman, "A new approach to linear filtering and prediction problems," *J Basic Eng–T ASME*, vol. 82, no. Series D, pp. 35–45, 1960.

[46] S. Ahmad, H. Huang, and A. J. Yu, "Cost-sensitive Bayesian control policy in human active sensing," *Front Hum Neurosci*, vol. 8, no. 955, 2014.

[47] J. F. Ferreira, J. Lobo, P. Bessière, M. Castel-Braco, and J. Diaz, "A Bayesian framework for active artificial perception," *IEEE T Syst Man Cyb*, vol. 43, no. 2, pp. 699–711, April 2013.

[48] D. Schauer and O. Linton, "NCRP Report No. 160, Ionizing radiation exposure of the population of the United States, medical exposure–are we doing less with more, and is there a role for health physicists?" *Health Phys*, vol. 97, no. 1, pp. 1–5, 2009.

[49] E. Ketteler and K. Brown, "Radiation exposure in endovascular procedures," *J Vasc Surg*, vol. 53, pp. 35S–38S, 2011.

[50] R. Fazel, H. Krumholz, Y. Wang, J. Ross, J. Chen, H. Ting, N. Shah, K. Nasir, A. Einstein, and B. Nallamothu, "Exposure to low-dose ionizing radiation from medical imaging procedures," *N Engl J Med*, vol. 361, no. 9, pp. 849–857, 2009, pMC3707303.

[51] F. Mettler, T. Y. W. Huda, and M. Mahesh, "Effective doses in radiology and

diagnostic nuclear medicine: A catalog," *Radiology*, vol. 248, no. 1, pp. 254–263, 2008.

[52] C. Jones, S. Badger, and C. Boyd, C. S.and Soong, "The impact of radiation dose exposure during endovascular aneurysm repair on patient safety," *J Vasc Surg*, vol. 52, no. 2, pp. 298–302, 2010.

[53] M. Andreassi, E. Piccaluga, G. Guagliumi, M. D. Greco, F. Gaita, and E. Picano, "Occupational health risks in cardiac catheterization laboratory workers," *Circ Cardiovasc Interv*, vol. 9, p. e003273, 2009.

[54] Center for Devices and Radiological Health, "Initiative to reduce unnecessary radiation exposure from medical imaging," *US Food and Drug Administration*, Feb 2010.

[55] B. Maurel, J. Sobocinski, P. Perini, M. Guillou, M. Midulla, R. Azzaoui, and S. Haulon, "Evaluation of radiation during evar performed on a mobile c-arm," *Eur J Vasc Endovasc Surg*, vol. 43, pp. 16–21, 2012.

[56] A. S. Thakor, A. Winterbottom, M. Mercuri, C. Cousins, and M. Gaunt, "The radiation burden from increasingly complex endovascular aortic aneurysm repair," *Insights Imaging*, vol. 2, no. 6, pp. 699–704, 2011.

[57] P. Howells, R. Eaton, A. Patel, P. Taylor, and B. Modarai, "Risk of radiation

exposure during endovascular aortic repair," *Eur J Endovasc Surg*, vol. 43, no. 4, pp. 393–397, 2012.

[58] S. Walsh, T. Tang, M. Gaunt, and J. Boyle, "Contrast-induced nephropathy," *J Endovasc Ther*, vol. 14, no. 1, pp. 92–100, 2007.

[59] National Cancer Institute, "Interventional fluoroscopy: Reducing radiation risks for patients and staff," *National Institutes of Health*, March 2005.

[60] S. Matl, R. Brosig, M. Baust, N. Navab, and S. Demirci, "Vascular image registration techniques: A living review," *Med Imag Anal*, vol. 35, pp. 1–17, 2017.

[61] G. Dibildox, N. Baka, M. Punt, J. Aben, C. Schultz, W. Niessen, and T. van Walsum, "3D/3D registration of coronary CTA and biplane XA reconstructions for improved image guidance," *Med Phys*, vol. 41, no. 9, p. 091909, 2014.

[62] U. Mitrovic, Z. Spiclin, B. Likar, and F. Pernus, "3D-2D registration of cerebral angiograms: A method and evaluation on clinical images," *IEEE Trans Med Imag*, vol. 32, no. 8, pp. 1550–1563, Aug 2013.

[63] H. Heibel, B. Glocker, M. Groher, M. Pfister, and N. Navab, "Interventional tool tracking using discrete optimization," *IEEE Trans Med Imag*, vol. 32, no. 3, pp. 544–555, 2013.

[64] P. Markelj, D. Tomaževič, B. Likar, and F. Pernuš, "A review of 3D/2D registration methods for image-guided interventions," *Med Imag Anal*, vol. 16, pp. 642–661, 2012.

[65] P. Ambrosini, D. Ruijters, W. J. Niessen, A. Moelker, and T. van Walsum, "Continuous roadmapping in liver TACE procedures using 2D-3D catheter-based registration," *Int J CARS*, vol. 10, pp. 1357–1370, 2015.

[66] M. Nejati, S. Sadri, and R. Amirfattahi, "Nonrigid image registration in digital subtraction angiography using multilevel b-spline," *Biomed Res Int*, vol. 2013, p. 236315, July 2013, pMC3736499.

[67] B. Wood, H. Zhang, A. Durrani, N. Glossop, S. Ranjan, D. Lindisch, E. Levy, F. Banovac, J. Borgert, S. Krueger, J. Kruecker, A. Viswanathan, and K. Cleary, "Navigation with electromagnetic tracking for interventional radiology procedures: A feasibility study," *J Vasc Interv Radiol*, vol. 16, no. 4, pp. 493–505, 2005, pMC2375916.

[68] Z. Yaniv, E. Wilson, D. Lindisch, and K. Cleary, "Electromagnetic tracking in the clinical environment," *Med Phys*, vol. 36, no. 3, pp. 876–893, 2009, pMC2673677.

[69] F. Manstad-Hulaas, G. Tangen, L. Gruionu, A. Aadahl, and T. Hernes, "Three-dimensional endovascular navigation with electromagnetic tracking: Ex vivo and in vivo accuracy," *J Endovasc Ther*, vol. 18, no. 2, pp. 230–240, 2011.

[70] S. Condino, V. Ferrari, C. Freschi, A. Alberti, R. Berchiolli, F. Mosca, and M. Ferrari, "Electromagnetic navigation platform for endovascular surgery: how to develop sensorized catheters and guidewires," *J Med Robotics Comput Assist Surg*, vol. 49, no. 2, pp. 344–356, 2012.

[71] M. Rotter, Y. Takahashi, P. Sanders, P. J. Michel Haïssaguerre, L.-F. Hsu, F. Sacher, J.-L. Pasquié, J. Clementy, and M. Hocini, "Reduction of fluoroscopy exposure and procedure duration during ablation of atrial fibrillation using a novel anatomical navigation system," *Euro Heart J*, vol. 26, pp. 1415–1421, 2005.

[72] R. De Ponti, "Reduction of radiation exposure in catheter ablation of atrial fibrillation: Lesson learned," *World J Cardiol*, vol. 7, no. 8, pp. 442–448, 2015, pMC4549777.

[73] S. Nedios, P. Sommer, A. Bollmann, and G. Hindricks, "Advanced mapping systems to guide atrial fibrillation ablation: Electrical information that matters," *J Atrial Fibrillation*, vol. 8, no. 16, pp. 96–102, 2016.

[74] J. Hsing, J. Wang, and A. Al-Ahmad, *Electroanatomical mapping technologies*. Wiley-Blackwell, 2008, ch. 1.

[75] L. Richmond, K. Rajappan, E. Voth, V. Rangavajhala, M. Earley, G. Thomas, S. Harris, S. Sporton, and R. Schilling, "Validation of computed tomography image integration into the EnSite NavX mapping system to perform catheter

ablation of atrial fibrillation," *J Cardiovasc Electrophysiol*, vol. 19, no. 8, pp. 821–827, 2008.

[76] S. Nazarian, A. Kolandaivelu, M. M. Zviman, G. R. Meininger, R. Kato, R. C. Susil, A. Roguin, T. L. Dickfeld, H. Ashikaga, H. Calkins, R. D. Berger, D. A. Bluemke, A. C. Lardo, and H. R. Halperin, "Feasibility of real-time magnetic resonance imaging for catheter guidance in electrophysiology studies," *Circulation*, vol. 118, pp. 223–229, 2008.

[77] S. R. Dukkipati, R. Mallozzi, E. J. Schmidt, G. Holmvang, A. d'Avila, R. Guhde, R. D. Darrow, G. Slavin, M. Fung, Z. Malchano, G. Kampa, J. D. Dando, C. McPherson, T. K. Foo, J. N. Ruskin, C. L. Dumoulin, and V. Y. Reddy, "Electroanatomic mapping of the left ventricle in a porcine model of chronic myocardial infarction with magnetic resonance-based catheter tracking," *Circulation*, vol. 118, no. 8, pp. 853–862, 2008.

[78] N. Whiting, J. Hu, J. V. Shah, M. C. Cassidy, E. Cressman, N. Z. Millward, D. G. Menter, C. M. Marcus, and P. K. Bhattacharya, "Real-time MRI-guided catheter tracking using hyperpolarized silicon particles," *Sci Rep*, vol. 5, p. 12843, 2015.

[79] R. A. Omary, O. Unal, D. S. Koscielski, R. Frayne, F. R. Korosec, C. A. Mistretta, C. M. Strother, and T. M. Grist, "Real-time MR imaging-guided passive

catheter tracking with use of gadolinium-filled catheters," *J Vasc Interv Radiol*, vol. 11, no. 8, pp. 1079–1085, 2000.

[80] P. Magnusson, E. Johansson, S. Mansson, J. Petersson, C. Chai, G. Hansson, O. Axelsson, and K. Golman, "Passive catheter tracking during interventional MRI using hyperpolarized 13C," *Magn Reson Med*, vol. 57, no. 6, pp. 1140–1147, 2007.

[81] B. Fuerst, E. Sutton, R. Ghotbi, N. Cowan, and N. Navab, "Bioelectric navigation: A new paradigm for intravascular device guidance," in *Medical Image Computing and Computer-Assisted Intervention*, ser. LNCS, S. Ourselin, W. Wells, M. R. Sabuncu, G. Unal, and L. Joskowicz, Eds., vol. 9902. Springer, 2016.

[82] M. Dweck, M. Doris, M. Motwani, P. Adamson, P. Slomka, D. Dey, Z. Fayad, D. Newby, and D. Berman, "Imaging of coronary atherosclerosis evolution towards new treatment strategies," *Nat Rev Cardiol*, vol. 13, pp. 533–548, 2016.

[83] D. Huang, E. A. Swanson, C. P. Lin, J. S. Schuman, W. G. Stinson, W. Chang, M. R. Hee, T. Flotte, K. Gregory, C. A. Puliafito, and J. G. Fujimoto, "Optical coherence tomography," *Science*, vol. 254, no. 5035, pp. 1178–1181, 1991.

[84] M. Brezinski, G. Tearney, B. Bouma, J. Izatt, M. Hee, E. Swanson, J. Southern, and J. Fujimoto, "Optical coherence tomography for optical biopsy: Properties

and demonstration of vascular pathology," *Circulation*, vol. 93, no. 6, pp. 1206–1213, 1996.

[85] X. D. Li, S. A. Boppart, J. V. D. , H. Mashimo, M. Mutinga, W. Drexler, M. Klein, C. Pitris, M. L. Krinsky, M. E. Brezinski, and J. G. Fujimoto, "Optical coherence tomography: Advanced technology for the endoscopic imaging of barrett's esophagus," *Endoscopy*, vol. 32, no. 12, pp. 921–930, 2000.

[86] J. Welzel, E. Lankenau, R. Birngruber, and R. Engelhardt, "Optical coherence tomography of the human skin," *J Am Acad Dermatol*, vol. 37, p. 958963, 1997.

[87] U. Baran and R. Wang, "Review of optical coherence tomography based angiography in neuroscience," *Neurophoton*, vol. 3, no. 1, p. 010902, 2001.

[88] M. Farooq, A. Khasnis, A. Majid, and M. Kassab, "The role of optical coherence tomography in vascular medicine," *Vasc Med*, vol. 17, no. 12, pp. 63–71, 2009.

[89] J. Kim, K. Park, J. Ryu, J. Lee, M. Lee, H. Cho, H. Nam, O. Park, J. Song, T. Kim, D. Oh, D. Gweon, W.-Y. Oh, H. Yoo, and J. Kim, "Intravascular optical imaging of high-risk plaques *in vivo* by targeting macrophage mannose receptors," *Sci Rep*, vol. 6, p. 22608, 2016, pMC4780083.

[90] J. Li, T. Ma, D. Mohar, E. Steward, M. Yu, Z. Piao, Y. He, K. Shung, Q. Zhou, P. Patel, and Z. Chen, "Ultrafast optical-ultrasonic system and miniaturized

catheter for imaging and characterizing atherosclerotic plaques in vivo," *Sci Rep*, vol. 5, p. 18406, Dec 2015.

[91] M. Prasad, A. Cassar, K. Fetterly, M. Bell, H. Theessen, O. Ecabert, J. Bresnahan, and A. Lerman, "Image-based co-registration of angiography and intravascular ultrasound images," *Catheter Cardiovasc Interv*, pp. 2238–2249, Nov 2015.

[92] Z. Li, J. Li, J. Jing, T. Ma, S. Liang, J. Zhang, D. Mohar, A. Raney, S. Mahon, M. Brenner, P. Patel, K. K. Shung, Q. Zhou, and Z. Chen, "Integrated IVUS-OCT imaging for atherosclerotic plaque characterization," *IEEE J Sel Top Quantum Electron*, vol. 20, no. 2, p. 7100108, 2014, pMC3996710.

[93] G. von der Emde, H. Bousack, C. Huck, K. Mayekar, M. Pabst, and Y. Zhang, "Electric fishes as natural models for technical sensor systems," in *Bioengineered and Bioinspired Systems IV*, ser. SPIE Proceedings, Ángel B. Rodríguez-Vázquez, Ed., vol. 7365. SPIE, 2009, pp. 73 650B–1.

[94] G. Von der Emde, "Non-visual environmental imaging and object detection through active electrolocation in weakly electric fish," *J Comp Physiol A*, vol. 192, no. 6, pp. 601–612, 2006.

[95] J. B. Snyder, M. Nelson, J. Burdick, and M. MacIver, "Omnidirectional sensory and motor volumes in electric fish," *PLoS Biol*, vol. 5, no. 11, pp. 2671–2683, 2007, pMC2071945.

[96] G. Von der Emde, S. Schwarz, L. Gomez, R. Budelli, and K. Grant, "Electric fish measure distance in the dark," *Nature*, vol. 395, no. 6705, pp. 890–894, 1998.

[97] S. Stamper, E. Roth, N. Cowan, and E. Fortune, "Active sensing via movement shapes spatiotemporal patterns of sensory feedback," *J Exp Biol*, vol. 215, no. 9, pp. 1567–1574, 2012.

[98] S. Gabriel, R. Lau, and C. Gabriel, "The dielectric properties of biological tissues: II. Measurements in the frequency range 10 Hz to 20 GHz," *Phys Med Biol*, vol. 41, no. 11, pp. 2251–2269, 1996.

[99] G. Pop, W. Hop, L. Moraru, M. van der Jagt, J. Quak, D. Dekkers, Z. Chang, F. Gijsen, D. Duncker, and C. Slager, "Blood electrical impedance closely matches whole blood viscosity as parameter of hemorheology and inflammation," *Appl Rheol*, vol. 13, no. 6, pp. 305–312, 2003.

[100] U. Kyle, I. Bosaeus, A. De Lorenzo, P. Deurenberg, M. Elia, J. Manuel Gómez, B. Lilienthal Heitmann, L. Kent-Smith, J. Melchior, M. Pirlich, H. Scharfetter, A. M.W.J. Schols, and C. Pichard, "Bioelectrical impedance analysis—Part II: utilization in clinical practice," *Clin Nutr*, vol. 23, no. 6, pp. 1430–1453, 2004.

[101] L. Ward and M. Müller, "Bioelectrical impedance analysis," *Eur J Clin Nutr*, vol. 67, p. S1, 2013.

[102] G. von der Emde, K. Mayekar, H. Bousack, and M. Pabst, "Simulation of bionic electrolocation sensor based on weakly electric fish," in *IEEE World Congress on Nature & Biologically Inspired Computing*, A. Abraham, A. Carvalho, F. Herrera, and V. Pai, Eds. IEEE, 2009, pp. 830–834.

[103] M. Metzen, S. Biswas, H. Bousack, M. Gottwald, K. Mayekar, and G. von der Emde, "A biomimetic active electrolocation sensor for detection of atherosclerotic lesions in blood vessels," *IEEE Sens J*, vol. 12, no. 2, pp. 325–331, 2012.

[104] K. Mayekar, M. Gottwald, G. von der Emde, D. Damalla, and H. Bousack, "Characterization of a bionic electrolocation sensor using finite element modeling," in *2011 IEEE SENSORS Proceedings*, 2011, pp. 978–981.

[105] G. S. Kassab, E. R. Lontis, and H. Gregersen, "Measurement of coronary lumen area using an impedance catheter: finite element model and in vitro validation," *Ann Biomed Eng*, vol. 32, no. 12, pp. 1642–1653, 2004.

[106] O. Pauly, H. Heibel, and N. Navab, "A machine learning approach for deformable guide-wire tracking in fluoroscopic sequences," in *MICCAI 2010, Part III*, T. Jiang, N. Navab, J. P. W. Pluim, and M. A. Viergever, Eds. Berlin, Heidelberg: Springer-Verlag, 2010, pp. 343–350.

[107] M. Groher, D. Zikic, and N. Navab, "Deformable 2D-3D registration of vascular structures in a one view scenario," *IEEE Trans Med Imag*, vol. 28, no. 6, pp. 847–860, 2009.

[108] S. Chávez, "Catheter tracking for medical interventions," Master's thesis, Technische Universität München, 2013.

[109] H. Choi, B. Jansen, D. Birrer, and G. Kassab, "Effect of saline injection mixing on accuracy of conductance lumen sizing of peripheral vessels," *PLoS ONE*, vol. 8, no. 9, p. e74622, 2013, pMC3772889.

[110] P. Tormene, T. Giorgino, S. Quaglini, and M. Stefanelli, "Matching incomplete time series with dynamic time warping: an algorithm and an application to post-stroke rehabilitation," *Artif Intell Med*, vol. 45, pp. 11–34, 2009.

[111] J. Martin and D. Hirschberg, "Small sample statistics for classification error rates ii: confidence intervals and significance tests," University of California Irvine, Technical Report ICS-TR-96-22, 1996.

[112] M. Schwerter, F. Lietzmann, and L. R. Schad, "A novel approach for a 2D/3D image registration routine for medical tool navigation in minimally invasive vascular interventions," *Z Med Phys*, vol. 26, no. 3, pp. 259–269, 2016.

[113] University of Michigan, "Metro health: Coronary angioplasty," https://metrohealth.net/healthwise/coronary-angioplasty/, accessed: 2017-06-20.

[114] S. Sharma, "Experience with a new guidewire: The Terumo Runthrough NS," *Cath Lab Digest*, vol. 16, no. 3, Mar 2008.

[115] M. Svendsen, D. Birrer, B. Jansen, S. Teague, B. Combs, G. Schears, and

G. Kassab, "Accurate nonfluoroscopic guidance and tip location of peripherally inserted central catheters using a conductance guidewire system," *J Vasc Surg*, vol. 1, no. 2, pp. 202–208.e1, 2014.

[116] M. Earley, R. Showkathali, M. Alzetani, P. Kistler, D. Gupta, D. Abrams, J. Horrocks, S. Harris, S. Sporton, and R. Schilling, "Radiofrequency ablation of arrhythmias guided by non-fluoroscopic catheter location: a prospective randomized trial," *Eur Heart J*, vol. 27, pp. 1223–1229, 2006.

[117] J. Papagiannis, A. Tsoutsinos, G. Kirvassilis, I. Sofianidou, t. Koussi, C. Laskari, M. Kiaffas, S. Apostolopoulou, and S. Rammos, "Nonfluoroscopic catheter navigation for radiofrequency catheter ablation of supraventricular tachycardia in children," *PACE*, vol. 29, pp. 971–978, 2006.

[118] M. Schneider, G. Ndrepepa, I. Dobran, J. Schreieck, S. Weber, A. Plewan, I. Deisenhofer, M. Karch, A. Schomig, and C. Schmitt, "LocaLisa catheter navigation reduces fluroscopy time and dosage in ablation of atrial flutter: a prospective randomized study," *J Cardiovasc Electrophysiol*, vol. 14, pp. 587–590, 2003.

[119] P. Ho, S. Cheng, P. Wu, J. Poon, C. Cheng, J. Mok, and M. Tsang, "Ionizing radiation absorption of vascular surgeons during endovascular procedures," *J Vasc Surg*, vol. 46, no. 3, pp. 455–459, 2007.

[120] R. Rhee, "Taking advantage of opportunities to maximize infrarenal seal: ad-

vantages and applicability of the GORE C3 Delivery System," *Endovascular Today*, pp. 23–26, Mar 2015.

[121] G. Maleux, M. Koolen, and S. Heye, "Complications after endovascular aneurysm repair," *Semin Intervent Radiol*, vol. 26, no. 1, pp. 3–9, Mar 2009.

[122] R. Wald, S. Waikar, O. Liangos, B. Pereira, G. Chertow, and B. Jaber, "Acute renal failure after endovascular vs open repair of abdominal aortic aneurysm," *J Vasc Surg*, vol. 43, no. 3, pp. 460–466, Mar 2006.

[123] J. Anderson, D. Leonard, D. Braner, S. Lai, and K. Tegtmeyer, "Videos in clinical medicine: Umbilical vascular catherization," *N Engl J Med*, vol. 359, p. e18, 2008.

[124] T. Sawyer, "Umbilical artery catheterization technique," http://emedicine.medscape.com/article/1348931-technique, updated: 2017-02-24. Accessed: 2017-06-13.

[125] A. Gupta, M. Peesay, and J. Ramasethu, "Simple measurements to place umbilical catheters using surface anatomy," *J Perinatol*, vol. 35, pp. 476–480, 2015.

[126] J. Magnan, "Umbilical vein catheterization technique," http://emedicine.medscape.com/article/80469-technique, updated: 2017-05-15. Accessed: 2017-06-13.

Vita

Erin E. Sutton received a B. M. E. degree in Mechanical and Aerospace Engineering from the University of Dayton in 2012 and enrolled in the Mechanical Engineering Ph.D. program at Johns Hopkins University in 2012 with a focus in Robotics. She received her M.S. in Mechanical Engineering from Johns Hopkins University in 2016. She was inducted into the Pi Tau Sigma honor society in 2011 and received a National Science Foundation Graduate Research Fellowship in 2012 and an Achievement Rewards for College Scientists scholarship in 2015.